



Swiss Society for  
Biomedical Engineering



University  
of Basel

Wednesday, September 13<sup>th</sup>, 2023

## SSBE Annual Meeting

Department of Biomedical Engineering,  
University of Basel in Allschwil

Abstract submission deadline: July 15<sup>th</sup>, 2023  
<https://www.bmc.unibas.ch/agenda/agenda.phtml>

Scientific Committee:

Daniel Baumgartner, George Kouvas, Bert Müller, Erik Schkommodau,  
Christine Tanner

beer & pretzels  
after the meeting  
[www.kitchenbrew.ch](http://www.kitchenbrew.ch)

### Biomedical Imaging and Image Analysis

Nanoscale Approaches  
to Biology

Biomaterials Science  
and Engineering

Biomechanical  
Engineering

Computational  
Bioengineering

Swiss Medtech

Motion Analysis

Orthopedic  
Technology

Signal  
Processing

Medical Informatics

Neurotechnology

Digital  
Neurotherapeutics



Thickness distribution of an optically transparent aligner, see [doi.org/10.1117/1.JMI.9.3.031509](https://doi.org/10.1117/1.JMI.9.3.031509)


Dear colleagues

We are pleased to organize the 2023 Annual Meeting of the Swiss Society of Biomedical Engineering in Allschwil, BL. This one-day symposium aims to share recent experience and to discuss current challenges in biomedical engineering as well as to evaluate future developments for benefitting patients. For this purpose, two outstanding scientists, i. e. Judith Müller and Philipp Schneider, have been invited. Their presentations entitled “Boosting real-world data for clinical development employing artificial intelligence and machine learning” and “Quantitative three-dimensional X-ray imaging” will be complemented by six oral contributions, we have selected from the more than 50 submitted abstracts for poster presentations. The program will be completed by talks of the four short-listed finalists of our awards.

The meeting will cover a broad range of topics in biomedical engineering ranging from basic research to clinical applications. The morning sessions, however, will bring into focus the medical imaging and image analysis. To supplement the oral and poster contributions on this subject, the participants are invited to use our electron microscope with energy dispersive X-ray microanalysis, thanks to the sponsor Gloor Instruments AG.

We anticipate an exciting discussion of oral and poster presentations, which will also take place during lunch time and coffee breaks and, finally, will informally be continued in Allschwil's brewery with fresh lemonade and beer together with pretzels and pizza.

It is our pleasure to invite you broaden your acquaintance with biomedical engineering for the improvement of human health and initiating promising initiatives in the triangle: clinics – MedTech industry – university.



Bert Müller, Thomas Straumann-Chair for Materials Science in Medicine

- in the name of the organization team

We thank our sponsors for supporting the 2023 Annual Meeting of the Swiss Society of Biomedical Engineering.



**BIOTRONIK**

excellence for life



**EXCISCOPE**

**GLOOR**   
INSTRUMENTS

**RMS**



Testing • Research • Consulting

[www.rms-foundation.ch](http://www.rms-foundation.ch)

**satw**

it's all about  
technology



# SSBE 2023 Annual Meeting

Department of Biomedical Engineering, University of Basel, Hegenheimermattweg 167 B, Allschwil, BL

September 13, 2023

- 9:15 Welcome coffee, registration, placing posters
- 9:45 Welcome address by SSBE president **Philippe Büchler**
- 9:50 Keynote, chaired by **Bert Müller**  
**Philipp Schneider**, Bioengineering Science Research Group, University of Southampton, Southampton, UK; High-Performance Vision Systems, AIT Austrian Institute of Technology, Vienna, Austria:  
**Quantitative three-dimensional X-ray imaging**
- 10:35 Oral presentations - Imaging and image analysis, chaired by **Daniel Baumgartner**  
**Pezhman Eghbali**, Ecole Polytechnique Fédérale de Lausanne: **Preoperative glenoid bone mineral density effect on postoperative glenoid component loosening**  
**Mattia Humbel**, University of Basel: **A virtual slice through the entire human brain with micrometer resolution**  
**Paulo Sampaio**, University of Bern: **Müller matrix polarimetry for pancreatic tissue characterization**
- 11:20 Refreshments and light lunch at posters
- 13:00 Generally assembly
- 13:30 Oral presentations – General topics in biomedical engineering, chaired by **Erik Schkommodau**  
**Silje E. Jahren**, University of Bern: **In vivo validation of a novel soft aortic counter pulsation device based on dielectric elastomer actuators**  
**Tobias Ruff**, ETH Zurich: **A living biohybrid neural interface for synaptic deep brain stimulation of the visual thalamus**  
**Barbara Postolka**, KU Leuven: **A combined in vivo and in silico approach to estimate articular hindfoot mechanics**
- 14:15 Short-listed finalist presentations for Student Award, chaired by **Philippe Büchler**  
**Michael Chan**, Ecole Polytechnique Fédérale de Lausanne: **Reorganization of brain functional gradients during film watching**  
**Jonathan Muheim**, Ecole Polytechnique Fédérale de Lausanne: **The MiniTouch: a system to restore real-time thermal sensation for arm amputee individuals**
- 14:45 Refreshments at posters
- 15:30 Keynote, chaired by **Christine Tanner**  
**Judith Müller**, Executive Director, Head of AI and Genomics at Merck & Co, USA:  
**Boosting real-world data for clinical development employing artificial intelligence and machine learning**
- 16:15 Short-listed finalist presentations for Research Award, chaired by **George Kouvas**  
**Julia Wolleb**, University of Basel: **Automatic detection of pathological regions in medical images**  
**Philipp Aebischer**, University of Bern: **SMART insertions for cochlear implant electrode arrays**
- 16:45 Closing remarks by host **Bert Müller**
- 17:00 Coming together with local fresh lemonade & beer, pretzels & pizza at <https://www.kitchenbrew.ch/>



# Contents

<b>Keynotes</b>	<b>7</b>
Philipp Schneider, Quantitative three-dimensional X-ray imaging . . . . .	7
Judith Müller, Boosting real-world data for clinical development employing artificial intelligence and machine learning . . . . .	8
<b>Oral presentations - Imaging and image analysis</b>	<b>9</b>
Pezhman Eghbali et al., Preoperative glenoid bone mineral density effect on postoperative glenoid component loosening . . . . .	9
Mattia Humbel et al., A virtual slice through the entire human brain with micrometer resolution . . . . .	10
Paulo Sampaio et al., Müller matrix polarimetry for pancreatic tissue characterization . . . . .	11
<b>Oral presentations - General topics in biomedical engineering</b>	<b>12</b>
Silje E. Jahren et al., <i>In vivo</i> validation of a novel soft aortic counterpulsation device based on dielectric elastomer actuators . . . . .	12
Léo Sifringer et al., A living biohybrid neural interface for synaptic deep brain stimulation of the visual thalamus	13
Barbara Postolka et al., A combined <i>in vivo</i> and <i>in silico</i> approach to estimate articular hindfoot mechanics . .	14
<b>Short-listed finalist presentations</b>	<b>15</b>
C. H. Michael Chan et al., Reorganization of brain functional gradients during film watching . . . . .	15
Jonathan Muheim et al., The MiniTouch: a system to restore real-time thermal sensations for arm amputee individuals . . . . .	16
Julia Wolleb et al., Automatic detection of pathological regions in medical images . . . . .	17
Philipp Aebischer et al., SMART insertions for cochlear implant electrode arrays . . . . .	18
<b>Posters - Imaging and image analysis</b>	<b>19</b>
P01 Paola Bermudez-Lekerika et al., The role of IL-4 and IL-10 in degenerating intervertebral disc . . . . .	19
P02 Andrea Nüesch et al., Gram positive bacteria within the intervertebral disc and their potential influence on nucleus pulposus cells . . . . .	20
P03 Benjamin Gantenbein et al., An <i>in-vivo</i> rat spinal fusion model of the elderly . . . . .	21
P04 Dimitrios Tripkis et al., X-ray nanotomography of dental composites for wide color matching . . . . .	22
P05 Chris Celania et al., Exciscope Polaris: lab-based phase-contrast CT for low contrast samples . . . . .	23
P06 Griffin Rodgers et al., 3DX-ray histology for the investigation of temporal lobe epilepsy in a mouse model	24
P07 Matteo Frigelli et al., Optical coherence elastography assessment of the optomechanical effects of corneal cross-linking . . . . .	25
P08 Vahoura Tahsini et al., Quantification of internal crystalline lens biomechanics stored in different preservation conditions using OCE . . . . .	26
P09 Sébastien Muheim et al., Smart alignment system for optical coherence tomography . . . . .	27
P10 Dorian Vogel et al., Building probabilistic stimulation maps for DBS from high resolution intraoperative data	28
P11 Osman Berk Satir et al., Predicting the premorbid anatomy of the scapula with cycle generative adversarial networks . . . . .	29
P12 Marc Stawiski et al., Using an SQLite database with REDCap to enhance the capture of BIDS metadata . .	30
<b>Posters - Signal processing</b>	<b>31</b>
P13 Frédéric Bourgeois et al., Tremor detector: online BMFLC based method compared to offline PSD based method . . . . .	31
P14 Mélina Richard et al., The scent of pain: metabolic fingerprints of cold pressor test via real-time breath analysis in a multisite clinical trial . . . . .	32
P15 Kapil Dev Singh et al., Personalised therapeutic management of epileptic patients guided by pathway-driven breath metabolomics . . . . .	33
P16 Marlies Geys et al., Electrophysiological measurements during and after cochlear implantation . . . . .	34
P17 Christof Baeriswyl et al., Neural spike detection and sorting with autonomous linear state space models . .	35
P18 Camilo Mendez Schneider et al., Detection of nocturnal hypoglycaemia using non-invasive sensors in people with diabetes . . . . .	36
P19 Manavi Samaneh et al., Navigating flexible medical instruments using fiber sensors and deep learning . . .	37
<b>Posters - Biomechanical engineering</b>	<b>38</b>
P20 Diego Stutzer et al., Forces applied during ultrasonic scaling . . . . .	38
P21 Eleonora Croci et al., Load-induced scapula rotation during a 30° loaded arm abduction test in rotator cuff tears and controls . . . . .	39

P22 Jeremy Genter et al., Critical shoulder angle and glenohumeral biomechanics in shoulders with rotator cuff tears - an in situ study . . . . .	40
P23 Linda Bühl et al., Knee biomechanics and muscle activity after anterior cruciate ligament repair and reconstruction . . . . .	41
P24 Jonas Abeken et al., Including turbulent stresses in blood damage models: Reynolds-stress-based vs. dissipation-based approaches . . . . .	42
P25 Malavika H. Nambiar et al., Comparative analysis of PRK, SMILE, and LASIK for personalized refractive interventions . . . . .	43
P26 Michaela Maintz et al., Designing 3D-printed implants using topology optimization . . . . .	44
P27 Slavko Corluka et al., Development of a novel bioreactor for the mechanobiological study of the tendon-bone interface . . . . .	45
<b>Posters - Biomaterials science and engineering</b>	<b>46</b>
P28 Shuimu Chen et al., Conditioned medium from intervertebral disc inhibits autologous mesenchymal stromal cells and osteoblasts . . . . .	46
P29 Katherine B. Crump et al., In-vitro investigation of compression and catabolic cytokines on human cartilage endplate cells in agarose . . . . .	47
P30 Silvan Rüttimann et al., Exploring a novel spheroid 3D cell culture system for TIE2+ nucleus pulposus cells of the intervertebral disc . . . . .	48
P31 Esma B. Tankus et al., From nasal chondrocytes to a 3D bioprinted osteochondral tissue . . . . .	49
P32 Fabian Züger et al., 3D-bioprinting of cardiac tissue models with a novel cost-effective and versatile bioink . . . . .	50
P33 Elisa M. Kaufmann et al., Temporal interference stimulation of the phrenic nerves . . . . .	51
P34 Beate Lyko et al., Adaptive artificial muscles for treating incontinence . . . . .	52
P35 Lukas Graf et al., Dynamic compression tests with simultaneous electrochemical analysis of porous graded titanium . . . . .	53
P36 Nadia Milanesi et al., Optimization of hydrothermal treatments on orthopedic AZ31B alloy to improve corrosion resistance . . . . .	54
<b>Posters - Swiss medtech</b>	<b>55</b>
P37 Christian Grossmann Aybar et al., Thermal analysis of new transdermal devices for power transfer to ventricular assist devices . . . . .	55
P38 Thanh Tu Ha et al., Feasibility and accuracy of robot guided cold ablation osteotomy for extradural anterior clinoidectomy . . . . .	56
P39 Martina Schicker et al., Feasibility and accuracy of robot guided cold ablation osteotomy for extradural optic canal unroofing . . . . .	57
P40 Thanh Tu Ha et al., Model to simulate brain biopsies using a navigated robotic guiding system and a bone cutting laser . . . . .	58
P41 Céline Vergne et al., A robust electromagnetic tracking system for deep brain stimulation surgery . . . . .	59
P42 Ehsan Hassanpour Yesaghi et al., Polarimetric glucose measurement via digital polarization modulation . . . . .	60
P43 Nishant Gupta et al., A novel approach towards smart multi-functional catheters . . . . .	61

# Quantitative three-dimensional X-ray imaging

**Philipp Schneider**

*Bioengineering Science Research Group, Faculty of Engineering and Physical Sciences, University of Southampton,  
Southampton, UK*

*High-Performance Vision Systems, Center for Vision, Automation and Control, AIT Austrian Institute of  
Technology, Vienna, Austria*

**Abstract.** Living structures are an intricate three-dimensional arrangement of cells and tissue matrices. The structural analysis of tissues, however, generally remains constrained by microscopy of sparse two-dimensional sections, providing only a snapshot from which spatial relationships can be inferred. Image data is the prerequisite for quantifying the spatial organization and interrelation between anatomical structures in their native environment in order to understand their function. This talk will show the power of three-dimensional imaging to interrogate biological tissues with a special focus on micro computed tomography ( $\mu$ CT) in conjunction with advanced image processing & quantification. In the musculoskeletal field, research is geared towards a holistic understanding of bony tissue, considering the coupling between angiogenesis and osteogenesis. Therefore, we have implemented  $\mu$ CT and image processing for the simultaneous visualization and quantification of calcified bone and its intracortical vasculature, suggesting a sexually dimorphic regulation of the bone vascular network. We translated this framework to the field of paleontology to study cementum increments as a record of an animal's life history to overcome caveats of conventional cementochronology approaches [1] and further developed it for colonic crypts during the early stages of colorectal cancer [2]. We developed soft-tissue-optimized  $\mu$ CT for formalin-fixed, paraffin-embedded biopsy specimens beyond histology workflows to bridge the gap between biological and preclinical imaging [3], for which we have established a dedicated facility, see [www.xrayhistology.org](http://www.xrayhistology.org).

1. Newham et al.: *Journal of the Royal Society Interface*; 2020, 17:20200538. [10.1098/rsif.2020.0538](https://doi.org/10.1098/rsif.2020.0538), *Nature Communications*; 2020, 11:5121. [10.1038/s41467-020-18898-4](https://doi.org/10.1038/s41467-020-18898-4), *PLoS One*; 2021, 16:e0249743. [10.1371/journal.pone.0249743](https://doi.org/10.1371/journal.pone.0249743)
2. Rossides et al.: *Scientific Reports*; 2021, 11:14672. [10.1038/s41598-021-93184-x](https://doi.org/10.1038/s41598-021-93184-x)
3. Katsamenis et al.: *American Journal of Pathology*; 2019, 189:1608-20. [10.1016/j.ajpath.2019.05.004](https://doi.org/10.1016/j.ajpath.2019.05.004)

**Curriculum.** Philipp Schneider studied physics at ETH Zurich. After his PhD in bioengineering, Philipp advanced high-resolution three-dimensional bone imaging and experimental mechanics at the Institute for Biomechanics of ETH Zürich. Currently, he is Full Professor of Biomedical Imaging at the University of Southampton, where he has been the Academic Director of the  $\mu$ -VIS X-ray Imaging Centre (<http://www.muvis.org>) till 2021. His research team has developed and applied multi-scale and correlative biomedical imaging, undertaking translational efforts to integrate engineering knowledge into pre-clinical applications by high-resolution *in vivo* and *ex vivo* imaging. Prof. Schneider is the principal investigator of a Wellcome Trust-funded research program [www.xrayhistology.org](http://www.xrayhistology.org) and co-investigator for the National Research Facility for Lab X-ray CT in the UK, see [www.nxct.ac.uk](http://www.nxct.ac.uk). Since 2021, he has strategically led research in high-performance vision systems with a focus on high-speed sensing, AI-driven surface inspection, and three-dimensional measurement at the Austrian Institute of Technology.

# Boosting real-world data for clinical development employing artificial intelligence and machine learning

*Judith Müller*

*Executive Director, Head of AI and Genomics at Merck & Co, USA*

**Abstract.** Artificial intelligence (AI) - machine learning (ML) techniques together with the increase in vast and diverse data sets and the rise in compute power are transforming the way we investigate and understand complex systems, boost data, and perform biomedical research including biomedical engineering. First, an overview of machine learning will be given, including types of algorithms, addressable problems and a comparison with traditional methods. Second, the challenges associated with real-world data, including CT scans, will be discussed. AI/ML methodologies to tackle the challenges will be presented: How do they enable us to gain insight and to uncover pattern that were difficult to discern previously? Third, the presentation will illustrate the challenges and power of combining data sets of a variety of modalities and demonstrate the pros and cons of AI/ML approaches including state-of-the-art pre-trained transformer models for data enrichment and outcome prediction. Such approaches were used for ranking patients by their eligibility for clinical trials. Finally, challenges related to data quality, privacy, and interpretability, which must be effectively addressed to fully realize the potential of AI and ML in leveraging real-world data for knowledge discovery and advancements in biomedical research, will be highlighted.

**Curriculum.** Judith Müller earned a Master's of Science degree in physics at the RWTH in Aachen, Germany, before she has obtained her PhD in theoretical physics at McGill University in Montreal, Canada. First, she worked in the semiconductor industry for 14 years, where she modeled advanced electronic devices, specialized circuits, and developed methodologies for technology assessment and parametric yield improvements. Second, at Rosetta Design Group in the US, she provided contract R&D in computational macromolecular modeling. Third, as her interest and expertise in mathematical modeling of complex systems, data science, and machine learning continuously broadened, Dr. Müller joined GNS Healthcare, a biosimulation company based in Somerville, MA, USA, where she led a team to develop causal machine learning algorithms to extend capabilities of their proprietary REFS™ platform. Finally, as Vice President of Data Science at ConcertAI, she built and led an interdisciplinary team of data scientists and machine learning engineers to develop and deploy AI/ML solutions for clinical development using real-world oncology data. She recently joined Merck as executive director and head of AI and genomics.

# PREOPERATIVE GLENOID BONE MINERAL DENSITY EFFECT ON POSTOPERATIVE GLENOID COMPONENT LOOSENING

Pezhman Eghbali (1), Osman Berk Satir (2), Fabio Becce (3), Patrick Goetti (3),  
Philippe Büchler (2), Dominique Pioletti (1), Alexandre Terrier (1,3)

1) Ecole Polytechnique Fédérale de Lausanne (EPFL), Switzerland, 2) ARTORG Center for Biomedical Engineering Research, Switzerland, 3) Lausanne University Hospital (CHUV), Switzerland

\*Corresponding author: pezhman.eghbalishamsabadi@epfl.ch

## Introduction

Glenoid component loosening is one of the most common complications after anatomical total shoulder arthroplasty (aTSA), with up to 66% rate of fixation failure after 15 years [1]. Different factors have been hypothesized as causes of loosening, including preoperative glenoid bone quality and the extent of subchondral bone reaming [2]. In this study our objective was to evaluate the effect of preoperative glenoid bone mineral density (BMD) on glenoid component loosening.

## Materials and Methods

We considered CT scan and radiological loosening outcome of 135 aTSA patients (96 F, 36-88 years). BMD was evaluated in 6 volumes of interest (VOIs), divided into eight sectors (Fig. 1).

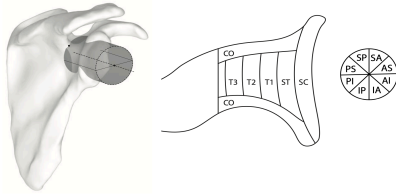


Fig. 1: BMD measured as HU within 6 VOIs: cortical bone (CO), subchondral cortical plate (SC), subchondral trabecular bone (ST), and 3 successive layers of trabecular bone (T1, T2, and T3), and octants.

The VOIs were defined within a 40 mm cylinder centered on the glenoid vault and aligned with the medio-lateral scapular axis. The method was fully automated [3]. We used a Bayesian network model to evaluate the (linear) effect of glenoid BMD, sex, age, and body mass index (BMI) on (log) years after surgery (Y) of glenoid component loosening (L).

$$Y_i | L_i = 1 \sim \text{Exponential}(\lambda_i)$$

$$Y_i | L_i = 0 \sim \text{Exponential-CCDF}(\lambda_i)$$

$$\lambda_i = 1.0 / \mu_i$$

$$\log(\mu_i) = \alpha_{\text{sex}}[i] + \beta_{\text{sex}}[i] * (\text{age} - 70) + \gamma_{\text{sex}}[i] * (\text{BMI} - 25) + \eta_i[\text{sex}] * \text{BMD}$$

$\lambda$  is the loosening rate,  $\mu$  is the time to loosening, and  $\alpha$ ,  $\beta$ ,  $\gamma$  and  $\eta$  are the average sex, age, BMI and BMD effects on the log of time to loosening.

We only considered the effect of BMD in the subchondral trabecular (ST) VOI, in all

sectors, as ST has paramount clinical importance since it guarantees the mechanical support of aTSA implants.

## Results

Females had a lower loosening rate, 52%, 10 years after surgery, while it was 59% for male. The age had an opposite effect on loosening for female and male. Increasing age from 60 to 70, increased the loosening rate by 6% for female and decreased it by 13% for male 10 years after surgery. Increasing BMI from 20 to 30 (kg/m<sup>2</sup>) for 70 years old subjects decreased the loosening rate by 18% for female and 32% for male 10 years after surgery. Increasing preoperative subchondral trabecular (ST) bone BMD by 2 z-score (from -1 to 1) in all sectors did not affect loosening rate for female, while decreased it by 8% for male 10 years after surgery (Fig. 2).

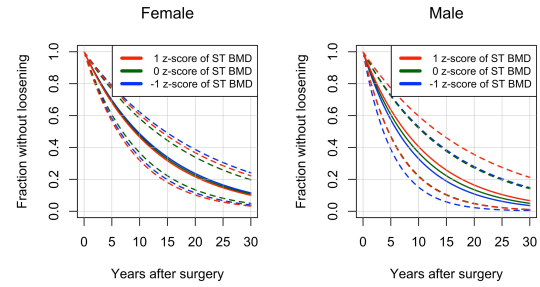


Fig. 2: Survival curves (1-loosening rate) (solid lines) and 89% compatibility interval (dashed lines) for female, male, and 3 values of BMD in ST: -1, 0 (mean) and +1 z-score, for each octant.

## Discussion

Although other studies have reported association between preoperative glenoid BMD and loosening [1], here, we could not find strong evidence for that for females (8% of loosening rate difference with 2 z-score change in BMD for males and less than 3% for females). However, this could be due to low number of cases in this study. We recommend an extension of this study with a higher number of subjects.

## References

1. M. Chamseddine et al, JSES, 28:18-28, 2019.
2. A. Terrier et al, JSES, 26:1644-1652, 2017.
3. P. Eghbali et al, JOR, 41:263-270, 2022.

## Acknowledgements

This work is supported by the Swiss National Science Foundation (Grant no: 189972).



# A VIRTUAL SLICE THROUGH THE ENTIRE HUMAN BRAIN WITH MICROMETER RESOLUTION

Mattia Humbel\* (1), Griffin Rodgers (1), Hans Deyhle (1), Georg Schulz (1), Christine Tanner (1), Felix Beckmann (2), Julian Moosmann (2), and Bert Müller (1)

1. University of Basel, Department of Biomedical Engineering, Biomaterials Science Center, Allschwil, Switzerland; 2. Helmholtz-Zentrum Hereon, Institute of Materials Physics, Geesthacht, Germany

\*Corresponding author: mattia.humbel@unibas.ch

## Introduction

Imaging anatomical features of human brain at a spatial resolution of about one micrometer requires physical sectioning. References such as the Allen brain atlas [1] or the BigBrain model [2] consist of a series of sections with related artefacts from slicing. Microtomography has been employed to image an entire human brain at a pixel size of 25  $\mu\text{m}$  and selected regions using 6  $\mu\text{m}$  [3]. This study aims to demonstrate the feasibility of imaging the entire human brain with one micrometer resolution without the need for physical sectioning using hard X-ray computed tomography.

## Materials and Methods

A human brain was formalin-fixated and then immersed in ethanol. Coronal sections 1 cm thick were prepared for X-ray imaging in a cylindrical polymer container.

Micro-computed tomography was performed at the P07 beamline, Deutsches Elektronen-Synchrotron (DESY), Hamburg, Germany using a mean photon energy of 67 keV. The detector unit, consisting of a 100  $\mu\text{m}$ -thin  $\text{CdWO}_4$  scintillator, a  $5\times$  objective lens, and a KIT CMOS detector, was placed 80 cm behind the brain disk with its axis perpendicular to the beam. The exposure time per projection was set to 150 ms.

With an effective pixel size of  $(1.27 \mu\text{m})^2$ , 16 projections were required to cover the brain disk with 10 cm diameter. The extended field of view was realized acquiring eight rings, each with 48'000 projections along 360 degrees. The rings were recorded in fly-scan mode. For one tomogram, step-scan mode with random sample movement after every 25<sup>th</sup> projection was employed. The projections were stitched and superimposed using the motor position before standard tomographic reconstruction.

## Results

A single reconstructed slice with  $2\times$  binning measures  $39'000\times 39'000$  pixels, occupying 6 GB of storage at 32-bit precision. The acquisition of one height step in fly-scan mode, see virtual coronal slice in Fig. 1, took fourteen hours. Step-scan acquisition needed tripled time, but helped reducing the ring artefacts present in the fly-scan acquisition.

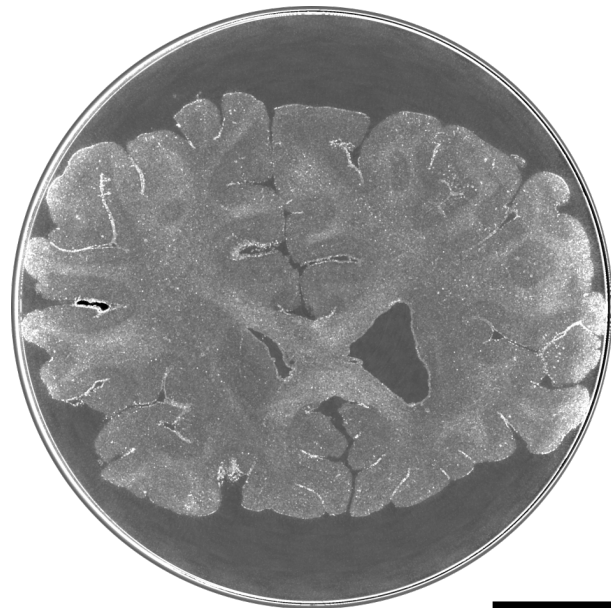


Figure 1: Virtual slice through an X-ray tomographic image of a brain disk 10 cm in diameter with an isotropic pixel length of 2.54  $\mu\text{m}$ . The scale bar is 2 cm.

## Discussion

This synchrotron radiation-based study shows the feasibility of employing X-ray tomography to image the entire human brain using isotropic voxels 2.54  $\mu\text{m}$  wide. In a next step, several 10'000 slices, each several GB in size, must be tiled vertically, posing the challenge of handling the big data of an entire human brain with PB size and providing access to the research community.

## References

1. Ding et al, J Comp Neurol, 524:3127-3481.
2. Amunts et al, Science, 340:1472-1475, 2013.
3. Walsh et al, Nat Methods 18:1532-1541, 2021.

## Acknowledgements

We thank Magdalena Müller-Gerbl, University of Basel, for providing the specimen used in this experiment. The work was financially supported by grant 185058 from the Swiss National Science Foundation. The research was authorized by the Ethikkommission Nordwest- und Zentralschweiz (EKNZ), project 2020-00047.





# MÜLLER MATRIX POLARIMETRY FOR PANCREATIC TISSUE CHARACTERIZATION

Paulo Sampaio\* (1), Maria Lopez Antuña (1), Federico Storni (2), Jonatan Wicht (1, 4), Greta Sökeland (3), Martin Wartenberg (3), Pablo Márquez Neila (1), Daniel Candinas (2), Brice-Olivier Demory (4), Aurel Perren (3), Raphael Sznitman (1)

1. ARTORG Center, University of Bern, Switzerland, 2. Department of Visceral Surgery and Medicine, Bern University Hospital, Switzerland, 3. Institute of Tissue Medicine and Pathology, University of Bern, Switzerland, 4. Center for Space and Habitability, University of Bern, Switzerland

\*Corresponding author: paulo.sampaio@unibe.ch

## Introduction

Müller Matrix Polarimetry (MMP) is a powerful technique for analyzing the optical properties of tissues. Its use for the characterization of different tissue types has been the subject of studies in recent years [1], nevertheless rarely in fresh pancreatic tissue, partially due to its heterogeneity, leading to a challenging differentiation [2]. However, accurate and reliable methods for diagnosing pancreatic diseases are critical for improving patient outcomes. To this end, we designed a machine-learning approach to process MMP data and accurately identify normal (endocrine/exocrine pancreas, fat and healthy stroma) and abnormal pancreatic tissue (fibrosis, chronic pancreatitis, malignant tumors, desmoplasia).

## Material and Methods

Using a custom-built spectro-polarimeter (fig. 1) [3], we imaged biopsy samples from 18 patients. After imaging,

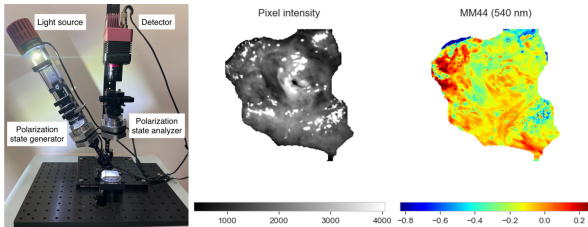


Figure 1: Custom-built polarimeter (left) and example of pixel intensity image (center) and one element from the Müller Matrix (right) acquired for one of the samples.

samples followed the histopathology pipeline to produce digital hematoxylin & eosin slides, which an expert pathologist annotated. From these, uniform regions were matched with the imaged sample and used as ground truth. A multi-layer perceptron (MLP) was used to classify each pixel as normal or abnormal. Two models were trained: MLP-pol (using polarimetric information) and MLP-no-pol (using pixel intensities). From 4 patient-basis splits, the area under the ROC curve and prediction scores for both models were evaluated.

## Results

MLP-pol yielded a classifier with an AUC of 0.91, far superior to the 0.68 obtained from MLP-no-pol. Moreover, the confidence of these predictions shows a clearer separation (fig. 2). Qualitatively, the MLP-pol

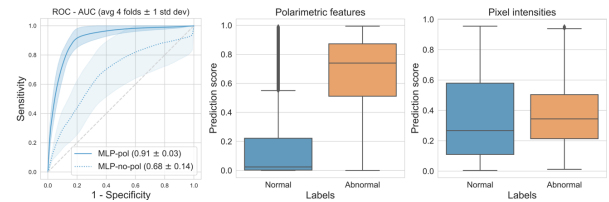


Figure 2: ROC-AUC for both MLP-pol and MLP-no-pol (left) and boxplots of prediction scores by class (center and right).

correctly identified the different tissue characterizations, while MLP-no-pol predicted in a narrow band (fig. 3).

## Discussion

The results demonstrated that MMP is superior to pixel intensities for pancreatic tissue characterization, highlighting surgeons' challenges in visually distinguishing different tissue types. The results obtained on samples containing both tissue types indicate that polarimetry is strong enough to overcome some intra-patient correlation (fig. 3C). Although coming from a small dataset, results are encouraging.

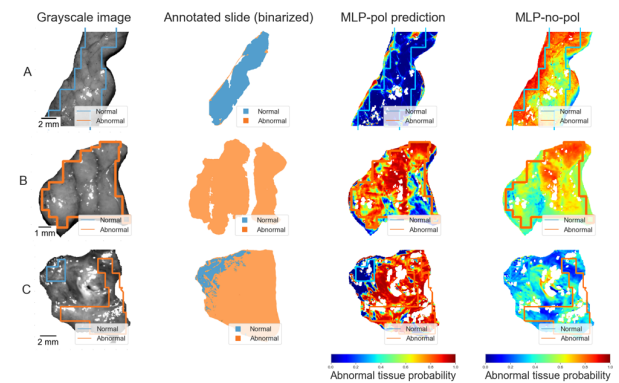


Figure 3: MLP-pol correctly identified tissue types in uniform samples (A and B) and mixed samples (C), while MLP-no-pol yielded similar scores for both labels.

## References

1. He, C. et al., Light. Sci. & Appl, 10:194, 2021.
2. Lanka, P. et al., Sci. Reports 12:14300, 2022.
3. Goldstein, D. H., Appl. Opt. 31:6676–6683, 1992.





# IN VIVO VALIDATION OF A NOVEL SOFT AORTIC COUNTERPULSATION DEVICE BASED ON DIELECTRIC ELASTOMER ACTUATORS

Silje E. Jahren\* (1), Thomas Martinez (2), Paul Philipp Heinisch (3), Francesco Clavica (1), Armando Walter (2), Eric Bufflé (1), Thierry Carrel (4), Yoan Civet (2), Jürgen Hörer (3), Dominik Obrist (1), Yves Perriard (2)

1. ARTORG Center, University of Bern, Switzerland; 2. Integrated Actuators Laboratory (LAI), École polytechnique fédérale de Lausanne (EPFL), Neuchâtel, Switzerland; 3. German Heart Center Munich, Technical University of Munich, University Hospital of Munich, Munich, Germany; 4. Department of Cardiac Surgery, University of Zurich, Zurich, Switzerland

\*Corresponding author: silje.jahren@unibe.ch

## Introduction

Aortic augmentation using dielectric elastomer actuators (DEAs) has been suggested as a new technological approach to cardiac assistance [1,2]. The purely electrically driven and soft tubular DEA-based device increases its diameter when activated and decreases it when deactivated. The device replaces a section of the aorta and is acting as a counterpulsation device.

## Material and Methods

The DEA-device is a soft tube consisting of a stack of four Elastosil films (Wacker Chemie) with compliant electrodes between each film (Figure 1A). The stack is glued together and rolled twice to create the tubular device (dimensions: 60mm length, 25mm in diameter). Figure 1B shows the DEA-tube. In this *in vivo* study, the DEA-based device is implanted in 5 pigs in proximity of the ascending aorta (Figure 1C and D). The device was tested in counterpulsation for different actuation synchronizations with the cardiac cycle.

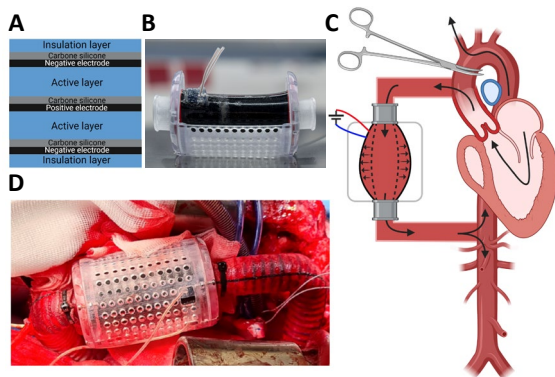


Figure 1: (A) The elastomer stack with compliant electrodes in between. (B) DEA-tube within protective housing (Félix Wey, Werner Siemens-Stiftung). (C) In vivo model: DEA-device was implanted in a graft between the ascending and descending aorta. The ascending aorta was clamped, and all blood went through the DEA. (D) Image of the implanted device. (A and B created with BioRender.com).

## Results

The pigs had an aortic pressure 80-100mmHg (systolic) and 30-60mmHg (diastolic). We demonstrate (best results) that the DEA can reduce end-diastolic pressure (13%), reduce peak left ventricular pressure (4%) and peak ascending aortic pressure (15%), and augment early diastolic pressure in the ascending aorta (10%). The best support was achieved with an activation around aortic valve opening (when pressure is low) and a deactivation around aortic valve closure (when pressure is high) (Figure 2).

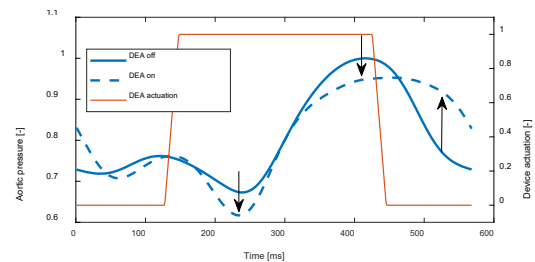


Figure 2: Representative results of the DEA in counterpulsation. It reduces the end-diastolic pressure and peak systolic pressure and augment the diastolic aortic pressure. The arrows indicate these three main effects of the device.

## Discussion

This *in vivo* study shows the feasibility and validation of the DEA-based counterpulsation device. The DEA actuator requires no bulky pneumatics and conforms closely to the aorta. A fully implantable device with trans-cutaneous wireless power transfer [3] could be achieved in the future as only electrical activation is required. Efforts are made to make the device less invasive by e.g., wrapping the DEA actuator around the aorta, to avoid direct contact of blood.

## References

1. Martinez et al., Bioeng Transl Med, 8(2):e10396, 2023.
2. Almanza et al., Adv. Sci., 8:2001974, 2021.
3. Knecht et al, IEEE Trans Power Electron, 30(11):6221-36, 2015.

## Acknowledgements

The authors would like to thank the experimental surgery facility team of the University of Bern.



# A LIVING BIOHYBRID NEURAL INTERFACE FOR SYNAPTIC DEEP BRAIN STIMULATION OF THE VISUAL THALAMUS

Léo Siffringer (1), Alex Fratzl (2), Stephan J. Ihle (1), Parth Chansoria (4), Jens Duru (1), Blandine Clément (1), Sinead Conolly (1), Benedikt Maurer (1), Christina M. Tringides (1), Leah Mönkemöller (1), Giulia Amos (1), Sean Weaver (1), Sophie Girardin (1), Katarina Vulić (1), Simon Steffens (1), Anna Beltraminelli (1), Eylul Ceylan (1), Srinivas Madduri (3), Marcy Zenobi-Wong (4), Botond Roska (2), János Vörös (1) and Tobias Ruff\* (1)

<sup>1</sup>Laboratory of Biosensors and Bioelectronics, ETH Zurich, Institute for Biomedical Engineering, Switzerland

<sup>2</sup>Institute of Molecular and Clinical Ophthalmology Basel, Switzerland

<sup>3</sup>Center for Bioengineering and Regenerative Medicine, University of Basel, Switzerland

<sup>4</sup>Laboratory of Tissue Engineering and Biofabrication, ETH Zurich, Institute of Molecular Health Sciences

\*Corresponding author: toruff@ethz.ch

## Introduction

Restoring functional vision in blind patients lacking a healthy optic nerve requires bypassing retinal circuits. This can be achieved by high-resolution stimulation of the visual thalamus, which is located deep inside the brain and serves as the main input to cortical circuits underlying vision. However, available deep brain stimulation electrodes suffer from low stimulation resolution, limited biocompatibility and limited coverage of the targeted tissue. To overcome those limitations, we propose a novel living biohybrid neural interface with the goal of restoring functional vision in the blind without a healthy optic nerve. The biohybrid concept exploits on-chip grown retinal neurons as relays to convert electrical signals from a stretchable 2D microelectrode array into synaptic stimulation of a neural target tissue (Figure 1 A).

## Material and Methods

The stretchable Polydimethylsiloxane (PDMS) based micropatterned microelectrode array is fabricated by a transfer stripping method [1,2]. A PDMS microfluidic axon guidance structure is aligned and bond onto the microelectrode array. To increase biocompatibility of the device we fabricate a nerve forming gelatin methacryloyl (GelMA)[3] tube of only 300  $\mu\text{m}$  diameter directly onto the PDMS device. Finally, living retinal neurons labelled with a viral vector (AAV-DJ/2 hSyn1 mRuby3, 3\*10<sup>4</sup> vg/cell) are seeded into the 16 seeding wells and cultured under standard cell culture conditions prior to implantation.

## Results and Discussion

We explain the fabrication of the biohybrid neural interface and show how the retinal ganglion cells seeded into the implant form an artificial optic nerve of up to 3 mm length (Figure 1B). We demonstrate how axons transit from the biohybrid implant into a nerve forming bioresorbable collagen tube that will guide axons from the implant towards a neural target structure for sensory reinnervation and synaptic stimulation of the visual thalamus in vivo.

We demonstrate the seeding of retinal spheroids into our biohybrid devices using a modified fluid force microscope. We show that retinal spheroids can be stimulated using the stretchable microelectrode array. To assess signal transmission in the biohybrid implant we present in vitro data on how spikes propagate within the axon guidance channels to modulate thalamic target activity using glass and CMOS<sup>[4]</sup> multielectrode arrays.

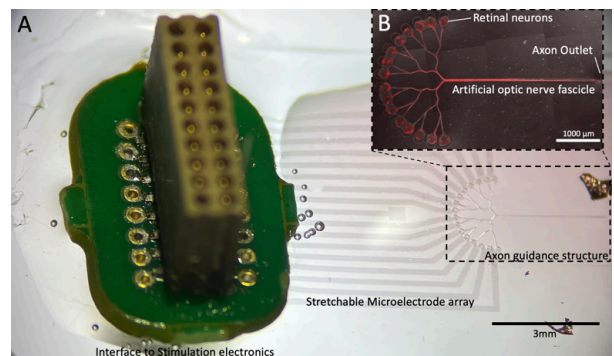


**Figure 1:** A) PDMS based 16 channel biohybrid neural interface. An axon guidance structure containing living neurons is aligned onto a stretchable multielectrode array to enable stimulation of retinal neurons. The stretchable electrode array is bond to a PCB to interface with the stimulation electronics. B) Retinal neurons form a more than 3mm long on-chip grown artificial optic nerve fascicle. The biohybrid interface will be implanted onto the cortical surface of a mouse brain to support on-chip grown neurons with oxygen and nutrients.

Finally, we present first progress towards in vivo implantation.

## References

1. R.F. Tiefenauer et al., ACS Nano 12:2514-2520, 2018
2. N. Vachicouras et al., EML, 15:63-69, 2017
3. H. Liu et al., Adv. Healthc. Mater., 34:2204301, 2022
4. J. Duru et al., Front. Neurosci., 16:829884, 2022

## Acknowledgements

This work was supported by the Human Frontiers Science Project (HFSP) postdoc fellowship, the OPO foundation, Swiss National Science Foundation and ETH Zürich.



# A COMBINED *IN VIVO* AND *IN SILICO* APPROACH TO ESTIMATE ARTICULAR HINDFOOT MECHANICS

Barbara Postolka\* (1), Bryce A Killen (1), Hannelore Boey (1,2), Jos Vander Sloten (2), Ilse Jonkers (1)

1. Human Movement Biomechanics Research Group, KU Leuven, Belgium

2. Biomechanics Section, KU Leuven, Belgium

\*Corresponding author: barbara.postolka@kuleuven.be

## Introduction

Increased joint contact stress can lead to cartilage degeneration and thus the development of osteoarthritis. Musculoskeletal simulations can present valuable information pertaining to articular joint loading which cannot directly be measured *in vivo*. As such, they may provide insights into the role of mechanical loading in disease development. While articular joint loading has been well studied in the knee [1], less is known about loading of the hindfoot. Therefore, the aim of this study was to combine high fidelity *in vivo* kinematics with state-of-the-art musculoskeletal simulations to estimate ankle and subtalar joint loading in healthy and chronic ankle instable subjects.

## Material and Methods

9 healthy subjects ( $24 \pm 3$  years) with no history of foot-ankle injuries and 7 subjects ( $30 \pm 10$  years) with clinically diagnosed chronic ankle instability (CAI) participated in this study. *In vivo* hindfoot kinematics were acquired during a simulated stance phase using 4D CT imaging [2]. For *in silico* assessment of the hindfoot articular joint mechanics, cartilage contact meshes for the ankle (tibia/talus) and subtalar (talus/calcaneus) joints were added to an existing foot-ankle model [3]. Articular joint contact was modelled using an elastic foundation formulation [1]. Models were then used in a forward simulation whereby ankle and subtalar rotations were prescribed based on the 4D CT measurements and translations were solved. Articular joint mechanics were then estimated using the OpenSim joint articular mechanics (JAM) tool [1].

## Results

Contact area and mean cartilage contact pressure were comparable between the healthy and CAI subjects throughout the simulated stance phase for both, the ankle and subtalar joint (Figure 1). At the beginning of the stance phase, contact pressure was evenly distributed between the ankle and subtalar joint. During the first half of the stance phase, where the foot moves into plantarflexion, higher contact pressure occurred at the ankle joint. After mid-stance and with increasing dorsiflexion, contact pressure was redistributed from the ankle to the subtalar joint (Figure 1). Peak ankle contact pressure occurred at  $31 \pm 10\%$  of the simulated stance phase (healthy  $4.23 \pm 0.29$  MPa; CAI  $4.21 \pm 0.20$  MPa) while peak subtalar contact pressure occurred at  $69 \pm 5\%$  (healthy  $4.35 \pm 0.43$  MPa; CAI  $4.08 \pm 0.34$  MPa; Figure 2).

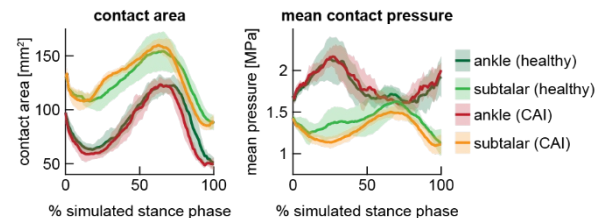


Figure 1: Contact area and mean contact pressure of the ankle and subtalar joint throughout the simulated stance phase for healthy and CAI subjects. Mean and standard deviations are shown for each subject group.

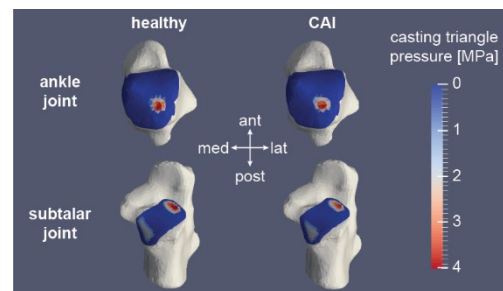


Figure 2: Cartilage contact pressure distribution of the ankle joint projected on the talus (top) and subtalar joint projected on the calcaneus (bottom) for a healthy (left) and CAI (right) subject at peak contact pressure.

## Discussion

This study presents proof of concept data of articular hindfoot mechanics during a simulated stance phase in healthy and chronic ankle instable subjects. In line with previous findings assessing *in vivo* hindfoot kinematics [2], similar articular joint loading was found for both groups. Combining high fidelity *in vivo* kinematics and recently developed *in silico* methods [1] to estimate articular joint mechanics, this study provided novel insights into the location and magnitude of joint contact at the ankle and subtalar joints.

## References

1. Smith et al, Comput Methods Biomech Biomed Eng Imaging Vis, 6:491-498, 2018.
2. Postolka et al, 8<sup>th</sup> iFAB Congress, 2023.
3. Malaquias et al, Comput Methods Biomech Biomed Engin, 20(2):153-159, 2017.

## Acknowledgements

This work has been funded by an SNF Postdoc.Mobility fellowship (500PM 214210), the Berghmans-Dereymacker research chair on foot & ankle biomechanics, and the Research Foundation Flanders (1S36519N).





# REORGANIZATION OF BRAIN FUNCTIONAL GRADIENTS DURING FILM WATCHING

Chun Hei Michael Chan (1,2), Laura Vilaclara (1,2), Patrik Vuilleumier (3,4), Dimitri Van De Ville\*(1,2), Elenor Morgenroth\* (1,2)

1. Neuro-X Institute, Ecole Polytechnique Fédérale de Lausanne (EPFL), Switzerland; 2. Department of Radiology and Medical Informatics, University of Geneva, Switzerland; 3. Geneva Neuroscience Center, Department of Neuroscience, University of Geneva, Switzerland; 4. NCCR Affective Sciences, University of Geneva, Switzerland

\*Corresponding authors: chunheimichael.chan@epfl.ch, dimitri.vandeville@epfl.ch

## Introduction

The use of film in functional magnetic resonance imaging (fMRI) [1] has recently gained great interest to study brain function, but also as a replacement for the resting-state condition with better participant compliance [2]. However, analysis of naturalistic stimuli is complex and has benefited from advanced methods such as decoding of individual differences based on functional connectivity (FC) [3,4]. In this work we build upon the functional gradients methodology [5], which provide an elegant way to represent the macrostructure of brain organization. We specifically investigate the relationship between gradients and emotion processes during film watching. Our results show the impact of social and affective events on brain reorganization by considering subject variability and prediction of individual differences.

## Methods

We collected rest and film fMRI recordings from 30 healthy participants. We further used continuous annotations of emotion experience from an independent sample of 43 participants (outside the MR scanner). From these we derived “ground truth” of emotion experience, and we then tailored the functional gradients pipeline and considered Schaeffer 400 parcellation of brain activation. We extracted the first three functional gradients from which we compute the average distance to centroid which is a subject level metric. In addition, the method of emotion-informed gradients is introduced, that is to select timeframes according to levels of valence/arousal/dominance when generating gradients. We investigate the intersubject variability and also predict individual differences with lasso regression using our emotion-informed gradients’ metrics.

## Results

First, we find that functional gradients are more variable in rest than in films (Fig 1A). Then, gradients from film can predict reliably individual differences in anxiety, while gradients from rest predict openness (Fig 1B). Through emotion-informed gradients we find that frames with high arousal and low valence show the highest level of predictability for Anxiety scores while prediction by rest still outperforms emotion-informed gradients in Openness scores (Fig 2).

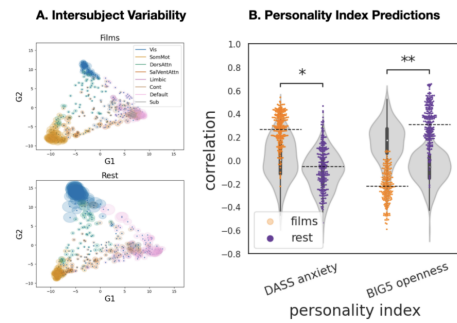


Figure 1: (Fig A) Intersubject variability across all parcels for Films Gradients and Rest Gradients. (Fig B) Prediction results on test folds for Anxiety and Openness

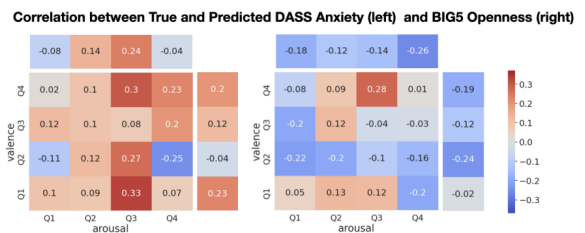


Figure 2: Prediction results (correlation with ground truth) on test folds for Anxiety and Openness

## Discussion

Our findings show that the gradient space derived from film fMRI is more stable across subjects, consistent with FC in film [4]. While the literature showed film to be superior to rest in personality prediction [3][6], our results do not support this for gradients. Our work is also the first to show emotion-informed gradients to predict individual differences. We demonstrate that processes such as emotion experience reflect idiosyncrasy.

## References

1. Hasson et al., Projections 2.1: 1-26, 2008
2. Vanderwal et al., Neuroimage, 122, 222-232, 2015
3. Finn et al., NeuroImage, 235, 117963, 2021
4. Vanderwal et al., Neuroimage, 157, 521-530, 2017
5. Margulies et al., Proceedings of the National Academy of Sciences, 113(44), 12574-12579, 2016
6. Samara et al., NeuroImage, 271, 120023, 2023



# THE MINITOUCH: A SYSTEM TO RESTORE REAL-TIME THERMAL SENSATIONS FOR ARM AMPUTEE INDIVIDUALS

Jonathan Muheim (1), Francesco Iberite (2), Outman Akouissi (1,3), Silvestro Micera\* (1,2), Solaiman Shokur\* (1)

1. Bertarelli Foundation Chair in Translational Neural Engineering, Neuro-X Institute, École Polytechnique Fédérale de Lausanne, 1015 Lausanne, Switzerland

2. The BioRobotics Institute, Health Interdisciplinary Center, and Department of Excellence in Robotics and AI, Scuola Superiore Sant'Anna, 56127 Pisa, Italy

3. Bertarelli Foundation Chair in Neuroprosthetic Technology, Neuro-X Institute, École Polytechnique Fédérale de Lausanne, 1015 Lausanne, Switzerland

\*Corresponding authors: [silvestro.micera@epfl.ch](mailto:silvestro.micera@epfl.ch) and [solaiman.shokur@epfl.ch](mailto:solaiman.shokur@epfl.ch)

## Introduction

One of the reasons commonly invoked for the high rejection rate of robotic prosthetic hands is the users' failure to perceive the prosthesis as part of their own body due to the lack of sensory feedback [1]. Therefore, researchers have sought to develop novel approaches to restore the rich catalog of sensations mediated by the human hand [2,3,4]. Here, we target a largely neglected modality: the ability to have thermal sensations.

## Material and Methods

We developed the MiniTouch, a portable prosthetic system that delivers continuous and realistic thermal sensations (Figure 1). The MiniTouch is composed of an Active Thermal Skin (ATS) sensor. The ATS sensor is a thin-film temperature sensor designed to mount commercial prosthetic hands easily. It integrates a heating track that increases the sensor surface temperature to the human skin level (32°C) allowing the measurement of realistic thermal changes. A closed-loop controller mediates the ATS sensor temperature via Peltier elements placed on the residual arm. We assessed the validity of the MiniTouch system to restore natural thermal sensations with 9 transradial amputee individuals. The thermode was placed on thermal phantom spots, specific locations on the residual arm that elicit a temperature sensation on the phantom hand when stimulated with warm or cold objects.

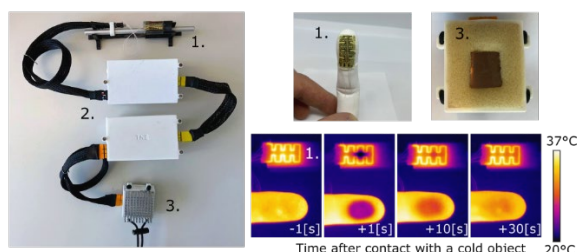


Figure 1: The MiniTouch system is composed of the ATS sensor (1.) a control unit (2.) and a wearable thermal display (3.).

## Results

In the first task, the participants reported temperature levels (cold, cool, neutral, or warm) while the

experimenter placed the ATS sensor in contact with cups at 15°, 24°, and 40°C. On average, participants could detect 97.2% of the contacts with hot cups, 66.7% with cool cups (55.6% reported as cool, 11.1% as cold), and 97.2% with cold cups (36.1% reported as cool, 61.1% as cold) (Figure 2, left). In the second task, the participant was asked to identify three materials at room temperature with different thermal conductivities (Copper, Glass, and Plastic). When the thermal sensation was mediated with the MiniTouch (accuracy: 65.93%) the participants performed similarly well with their intact hand (67.41%) (Figure 2, right).

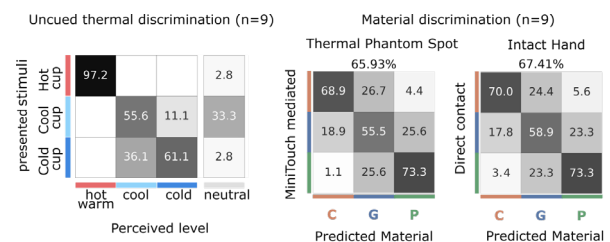


Figure 2: Group performance of nine transradial amputee individuals using the MiniTouch.

## Discussion

We developed a system that allows the restoration of continuous and natural thermal sensations in upper-limb amputees. This device could help increase the embodiment of robotic prosthetic hands.

## References

1. D. M. Page et al., Front. Hum. Neurosci., 12:352, 2018.
2. C. M. Oddo et al., eLife, 5:e09148, 2016.
3. S. Raspopovic et al., Sci. Transl. Med., 6:222ra19, 2014.
4. D. W. Tan et al., Sci. Transl. Med., 6:257ra138, 2014.

## Acknowledgements

This work was supported by the Bertarelli Foundation (including the Catalyst program); the Swiss National Science Foundation through the National Centre of Competence in Research (NCCR) Robotics and the CHRONOS project; and the European Union's Horizon 2020 research and innovation program under Marie Skłodowska-Curie grant 754354.



# AUTOMATIC DETECTION OF PATHOLOGICAL REGIONS IN MEDICAL IMAGES

Julia Wolleb\* (1), Robin Sandkühler (1), Cristina Granziera (1,2), Philippe C. Cattin (1)

1. Department of Biomedical Engineering, University of Basel, Switzerland

2. University Hospital Basel, Switzerland

\*Corresponding author: julia.wolleb@unibas.ch

## Introduction

Medical images are critical for detecting, diagnosing, and monitoring disease. Advances in deep learning enable automated analysis of these images. The goal of this PhD thesis was to develop algorithms for automatic detection of pathological regions in patient images, as presented in Figure 1.

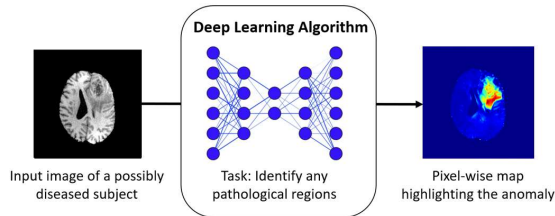


Figure 1: The goal of this PhD thesis was to develop deep learning algorithms that automatically identify anomalous changes in medical images, to lead the attention to the relevant parts of the anatomy.

## Material and Methods

By analysing diverse medical image datasets including X-ray, CT, and MR images, we develop novel deep learning methods for the varying data and label availability in medical applications. First, we propose a fully supervised segmentation approach using denoising diffusion models [1] that provides interpretable uncertainty maps. Since manual annotations are biased and difficult to obtain, we introduce weakly supervised methods [2,3] based on generative models that generate pixel-wise anomaly maps using only image-level annotations, as shown in Figure 2. By extending our diffusion-based anomaly detection approach [3], we create a flexible framework for various image-to-image translation tasks [4].

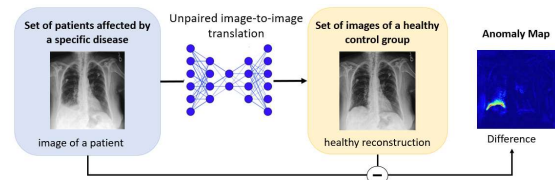


Figure 2: Workflow for weakly supervised anomaly detection using unpaired image-to-image translation between a set of patients and a healthy control group.

To address bias in MR images from different hospitals, we present a regularization strategy [5] to improve model robustness and generalization.

## Results

Limited availability of data and corresponding labels imposes various challenges to state-of-the-art deep learning approaches and has a direct impact on the degree of automatization that can be achieved. We explored various scenarios depending on the amount of data and labels accessible and proposed methods to cope with the given limitations. Figure 3 shows exemplary results for one of our weakly supervised approaches [3]. All presented methods perform well for their given task, each representing a building block toward generalizable and applicable deep learning methods.

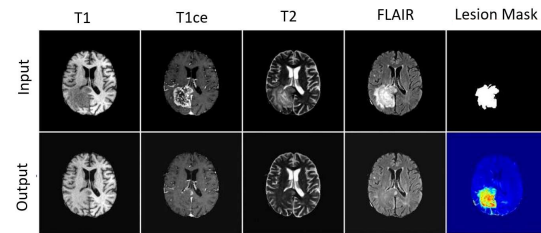


Figure 3: Results for our weakly supervised brain tumor detection algorithm [3] on the BraTS2020 dataset. The difference map between input and output accurately highlights pathological changes.

## Discussion

While our approaches [1-5] show promising results, the combination of these building blocks is essential to improve model robustness and interpretability and to establish reliable deep learning methods for clinical applications.

## References

1. J. Wolleb et al, PMLR, 172:1336-1348, 2022.
2. J. Wolleb et al, MICCAI Proceedings, IV:14-24, 2020.
3. J. Wolleb et al, MICCAI Proceedings, VIII :35-45, 2022.
4. J. Wolleb et al, arXiv preprint (arXiv:2204.02641), 2022.
5. J. Wolleb et al, MICCAI Proceedings, VII :725-735, 2022.

## Acknowledgements

This work was supported by Novartis Freenovation and the Uniscientia Foundation.



Annual Meeting of the Swiss Society of Biomedical Engineering  
Department of Biomedical Engineering, University of Basel, Allschwil (Switzerland)  
September 13, 2023

# SMART INSERTIONS FOR COCHLEAR IMPLANT ELECTRODE ARRAYS

Philipp Aebischer\* (1, 2), Stefan Weder (2), Mattheus Vischer (2), Lukas Anschütz (2), Georgios Mantokoudis (2), Marco Caversaccio (1, 2), Wilhelm Wimmer (3)

1. ARTORG Center for Biomedical Engineering Research, Switzerland; 2. Department for Otolaryngology, Head and Neck Surgery, Inselspital University Hospital Bern, Switzerland; 3. Technical University of Munich, Germany; TUM School of Medicine, Klinikum rechts der Isar, Department of Otorhinolaryngology

\*Corresponding author: philipp.aebischer@unibe.ch

## Introduction

The cochlear implant is a neural prosthesis that restores hearing by stimulating the auditory nerve through an array of electrodes surgically placed into the cochlea. But the inner ear is essentially a black box—with no visual access to the cochlea, surgeons must rely on their mental representation of the occluded anatomical structures. Worse, the forces needed to advance the electrode array are near the surgeon's force perception threshold [1], and comparable to forces needed to puncture vital intracochlear membranes [2]. Consequently, it is no surprise that injuries to the hearing organ are frequently reported. These injuries increase inflammatory reactions and fibrotic tissue growth, negatively affecting hearing outcomes [3]. Therefore, this thesis aims to develop tools to enhance the safety and minimize trauma associated with cochlear implantation procedures.

## Material and Methods

**In-Vitro Model Development:** Realistic in-vitro models of cochlear anatomy were created based on micro-computed tomography data. A hydrophilic coating mimics in-vivo frictional properties and the setup allows to simultaneously measure parameters related to physical loads and operator kinematics.

**Insertion Process Assessment:** With these models we comprehensively studied the impact of insertion speed, alignment of the implant and surgical technique during the implantation procedure. Furthermore, we developed a mathematical model for estimating load distribution along the electrode array onto cochlear structures.

**Insertion Tool Design:** An insertion tool concept that integrates into the conventional surgical workflow was developed, allowing safe redirection of the electrode array while protecting inner ear structures. A novel sleeve-based design allows the instrument to be compliant and potentially protective to intracochlear structures, while a tear-open mechanism allows it to be removed after insertion by simply retracting the tool (see Fig. 1).

**Intraoperative Position Estimation:** To judge the implant position, we developed a method for estimating electrode positions based on transimpedance measurements that are already acquired clinically for implant verification purposes.

## Results

Our developed models accurately match the relevant properties of in-vivo systems for assessing insertion me-

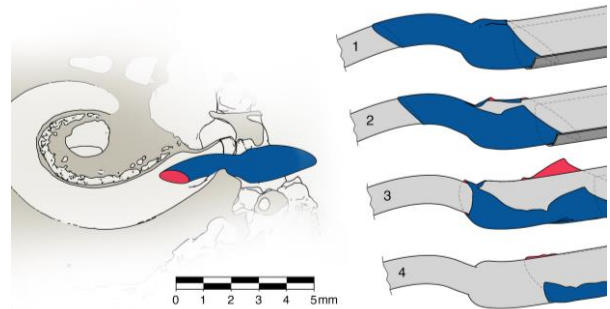


Figure 1: Left: Cut through the basal plane of a cochlea with the redirecting sleeve (blue) placed. Right: After electrode array insertion, the sleeve is removed by retraction, which causes a tear to propagate along its length until it is fully opened (step 1–4).

chanics. A comprehensive analysis of the surgical procedure performed in these models revealed that insertions parallel to the cochlear base minimize forces and improve array micro-motion. A mathematical model estimating electrode load distribution helped to improve our understanding of how the implantation affects intracochlear structures. These results governed the development of an insertion tool, which demonstrated a substantial reduction of forces exerted on the cochlea and intracochlear pressure transients. Lastly, the method for intraoperative estimation of the electrode positions from implant telemetry recordings performed with an accuracy close to measuring the position in postoperative computed tomography scans.

## Discussion

This thesis addresses cochlear implantation challenges by designing an atraumatic electrode array insertion tool and proposing an accurate method for intraoperative estimation of electrode positions within the cochlea. We hope that the concepts and ideas presented in this thesis will help reduce intracochlear trauma and ultimately improve hearing outcomes in patients receiving a cochlear implant.

## References

1. Kratchman et al, *Audiology and Neurotology*, 21.4:244–249, 2016
2. Ishii et al, *Acta Oto-Laryngologica*, 115:78–82, 1995
3. Foggia et al, *Inv. Otolaryngology*, 4.6:678–683, 2019





# THE ROLE OF IL-4 AND IL-10 IN DEGENERATING INTERVERTEBRAL DISC

Paola Bermudez-Lekerika\* (1,2), Sofia Tseranidou (3), Exarchos Kanelis (4,5), Katherine B. Crump (1,2), Christine Le Maitre (6), Karin Wuertz-Kozak (7), Leonidas G. Alexopoulos (4,5) Jérôme Noailly (3) and Benjamin Gantenbein (1,2)

1. Tissue Engineering for Orthopaedics and Mechanobiology, Bone & Joint Program, Department for BioMedical Research (DBMR), Medical Faculty, University of Bern, Bern, Switzerland; 2. Department of Orthopaedic Surgery & Traumatology, Inselspital, University of Bern, Switzerland; 3. BCN MedTech (Universitat Pompeu Fabra), Spain; 4. Protavio Ltd, Agia Paraskevi, Greece; 5. School of Mechanical Engineering, National Technical University of Athens, Zografou, Greece; 6. Medical School, University of Sheffield, Sheffield, United Kingdom; 7. Department of Biomedical Engineering, Rochester Institute of Technology, Rochester, United States

\*Corresponding author: [paola.bermudez@unibe.ch](mailto:paola.bermudez@unibe.ch)

## Introduction

Intervertebral disc (IVD) degeneration is a pathological process often associated with chronic back pain and considered a leading cause of disability worldwide [1]. During degeneration, progressive structural changes occur leading to blood vessel and nerve ingrowth that promote discogenic pain [2]. In the last decades, several cytokines have been applied to IVD cells *in vitro* to investigate the degenerative cascade. Particularly, IL-10 and IL-4 have been predicted as important anabolic factors in the IVD according to a regulatory network model based *in-silico* approach [3]. Thus, we aim to investigate the potential presence and anabolic effect of IL-10 and IL-4 in human NP cells (*in-vitro*) and explants (*ex-vivo*) under hypoxia (5% O<sub>2</sub>).

## Material and Methods

Primary human NP cells were expanded, encapsulated in 1.2% alginate beads (4 x 10<sup>6</sup> cells/ml) and cultured for two weeks with 1g/ml glucose DMEM under hypoxia (5% O<sub>2</sub>) for phenotype recovery. Similarly, human NP tissue explants were collected and placed into a ring culture system for five days with 1g/ml glucose DMEM under hypoxia (5% O<sub>2</sub>). Following pre culture, alginate and explant cultures were stimulated i) without 1ng/ml IL-1 $\beta$  for 2 days prior to two-day-stimulation with 10ng/ml IL-4, IL-10 (single treatments) or ii) with 1ng/ml IL-1 $\beta$  for 2 days prior to two-day-stimulation with 10ng/ml IL-4, IL-10 (combined treatments). Immunohistochemistry was used to determine expression of IL-4, IL-10 and IL-4 receptor in native human NP tissue.

## Results

The presence of IL-4 receptor, IL-4 and IL-10 was confirmed in human intact NP tissue (Figure 1). Additionally, IL-4 single and combined treatments induced a significant increase of proinflammatory protein secretion *in vitro* (Figure 2A-C) and *ex vivo* (Figure 2D and E). In contrast, no significant differences were observed in the secretome between IL-10 single and combined treatments compared to control.

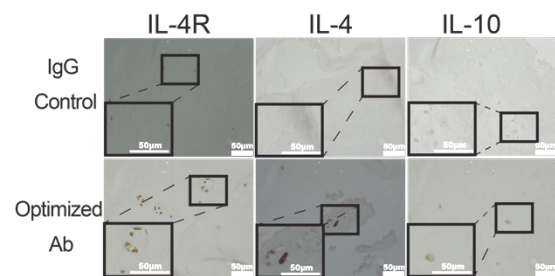


Figure 1: Immunohistochemical analysis for IL-4R, IL-4 and IL-10 in human NP tissue.

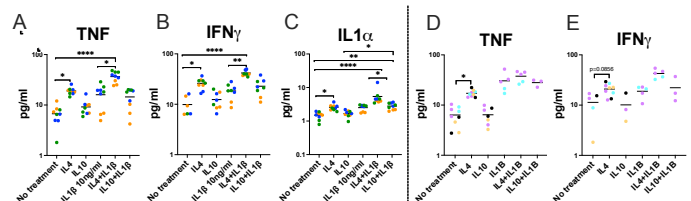


Figure 2: *In vitro* (A-C) and *ex vivo* (D and E) secretome analysis of proinflammatory and catabolic proteins. Shown are medians, N = 3, p-value: \* < 0.05, \*\* < 0.01, \*\*\* < 0.005 and \*\*\*\* < 0.001.

## Discussion

Overall, IL-4 containing treatments promote human NP cell and explant catabolism in contrast to previously reported IL-4 anti-inflammatory performance [4]. Thus, a possible pleiotropic effect of IL-4 could occur depending on the IVD culture and environmental condition.

## References

1. J. Hartvigsen et al, The Lancet 391:2356-67, 2018.
2. PPA. Vergroesen et al, Osteoarthritis and Cartilage 23:1165-77, 2015.
3. S. Tseranidou et al, EBS 28th Congress, Maastricht, The Netherlands, 2023.
4. H. Kedong et al, The Spine Journal 20:60-68, 2020.

## Acknowledgements

This project was supported by the Marie Skłodowska Curie International Training Network “disc4all” under the grant agreement #955735.



# GRAM POSITIVE BACTERIA WITHIN THE INTERVERTEBRAL DISC AND THEIR POTENTIAL INFLUENCE ON NUCLUES PULPOSUS CELLS

**Andrea Nüesch<sup>1</sup>, Exarchos Kanelis<sup>2</sup>, Leonidas Alexopoulos<sup>2</sup>, Frances Williams<sup>3</sup>, Benjamin Gantenbein<sup>4,5</sup>, Melissa Lacey<sup>6</sup>, Lee Breakwell<sup>1</sup>, Christine Le Maitre<sup>1</sup>**

<sup>1</sup>The University of Sheffield, Department of Oncology and Metabolism, S10 2TN, <sup>2</sup> Department of Mechanical Engineering, National Technical University of Athens, Athens, Greece <sup>3</sup> Department of Twin Research, King's College London, St Thomas' Hospital Campus, 4th Floor South Wing Block D, Westminster Bridge Road, London, SE1 7EH, UK. <sup>4</sup> Tissue Engineering for Orthopaedics & Mechanobiology (TOM), Department for BioMedical Research (DBMR) of the Faculty of Medicine of the University of Bern, University of Bern, Bern, CH <sup>5</sup> Department of Orthopaedic Surgery and Traumatology, Inselspital, Bern University Hospital, CH. <sup>6</sup> Biomolecular Sciences Research Centre, Sheffield Hallam University, S1 1WB, UK

\*Corresponding author: a.nuesch@sheffield.ac.uk

## Introduction

Modic changes (MC) that are vertebral bone marrow lesions visualised on magnetic resonance imaging have been associated with disc degeneration. For MC type I one of the identified aetiologies is infection of the intervertebral disc (IVD) [1]. However, there is controversy whether infection of the IVD is linked to disc degeneration. Even though there is increasing evidence for bacterial presence within the herniated disc, there are limited studies, which determine whether bacteria are present in the intact IVD *in vivo* or whether they represent contamination. This study aimed to investigate bacterial presence in non-herniated human IVDs and the potential influence of bacterial components on disc cells.

## Material and Methods

Immunohistochemical staining for Gram-positive bacterial membrane component, and specific antibodies for *Staphylococcus aureus*, *Cutibacterium acnes* Cellular recognition receptors Toll-like receptor (TLR) 2, TLR4 and NLR family pyrin domain containing 3 (NLRP3) and the pyroptosis marker Gasdermin D were performed on 90 human IVD samples. Furthermore, human nucleus pulposus cells in monolayer were treated with Lipopolysaccharide (LPS) (5-50µg/ml) and Peptidoglycan (PGN) (5-50µg/ml) for 48 hours. Cells in alginate were treated with PGN up to 72 hours. Secretome analysis was performed using Luminex for cytokines, chemokines, matrix degrading enzymes and other secreted factors. Statistical analysis was performed using Kruskal-Wallis and Dunn's multiple comparison test.

## Results

Gram-positive bacteria were internalized by at least one disc cell in 90 % of the samples. The percentage of cells containing bacteria across the NP was ~3%. Analysis for the abundance for the other factors is ongoing. Furthermore, the correlation between the abundance of bacteria, the TLR2, TLR4, NLRP3, Gasdermin D and the histological grade of disc degeneration will be investigated. Treatment of NP cells with LPS and PGN resulted in an increase of several catabolic cytokines

such as IL-1, TNF, IL-6 and IFN-γ alongside increased production of chemokines, neurotrophic and angiogenic factors associated with IVD degeneration.

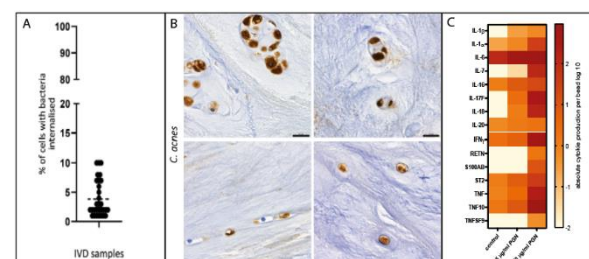


**Figure 1/ Presence of bacteria in intervertebral discs and their potential effects** **A** Average cells containing internalized bacteria after immunohistochemical (IHC) staining for Gram-positive bacteria was 4% (ranging 1-10%). Current work is determining correlations with histological grade of degeneration. **B** IHC staining for *C. acnes* lysate with enzyme antigen retrieval at a 1:100 dilution. Nuclei are stained in blue with Hematoxylin, the presence of *C. acnes* is shown in brown. **C** Cyto- and Chemokine expression of Nucleus Pulposus (NP) cells in Alginate stimulated with Peptidoglycans (PGN) from Gram-positive bacteria. PGN treatment induced catabolism in the NP cells in a dose dependent manner.

## Conclusion

This study demonstrated that Gram-positive bacteria are present in non-herniated and cadaveric human disc samples. Furthermore, bacterial cell membrane components triggered a catabolic response in human disc cells. Ongoing interaction studies between bacteria and NP cells will give insights into the internalisation mechanisms and potential role in disc degeneration.

## References

1. Dudli et al. European Spine Journal vol. 25. 3723–3734, 2016.

## Acknowledgements

This Project is part of the Disc4All Training network advance integrated computational simulations in translational medicine, applies to intervertebral disc degeneration and funded by Horizon 2020 (H2020-MCA-ITN-ETN-2020GA:955735)



# AN *IN-VIVO* RAT SPINAL FUSION MODEL OF THE ELDERLY

Benjamin Gantenbein<sup>\*,(1,2)</sup>, Katharina A. C. Oswald (1), Georg F. Erbach (1), Andreas S. Croft (2), Paola Bermudez-Lekerika (2), Franziska Strunz (2), Sebastian F. Bigdon (1), Christoph E. Albers (1)

1. Department of Orthopaedic Surgery and Traumatology, Inselspital, Bern University Hospital, University of Bern, Switzerland

2. Tissue Engineering for Orthopaedics and Mechanobiology, Bone & Joint Program, Department for BioMedical Research (DBMR), Medical Faculty, University of Bern, Bern, Switzerland

\*Corresponding author: [Benjamin.gantenbein@unibe.ch](mailto:Benjamin.gantenbein@unibe.ch)

## Introduction

Non-union and pseudoarthrosis remain major complications after spinal fusion surgery, resulting in unsatisfactory outcomes and high socio-economic costs. Several biomaterials and osteo-biologics have been used to improve spinal fusion, including bone morphogenetic protein (BMP)2 [1-3]. However, its necessary high dose application often leads to adverse effects. L51P, a BMP2 analogue and inhibitor of BMP antagonists, has been shown to augment BMP-induced bone formation and lower the required doses [4]. The current study therefore aimed to demonstrate the effects of L51P and BMP2 on spinal fusion *in vivo*.

## Material and Methods

46 elderly Wistar rats (~12 months, 52% female, 423±78g) underwent a two-step spinal fusion surgery [5, 6]. Firstly, a custom external fixator was applied in the proximal tail. Secondly, discectomy and disc replacement with a  $\beta$  tri-calcium-phosphate ( $\beta$ -TCP) carrier were conducted. Carriers were loaded with the study compounds based on random and blinded allocation into seven groups. Digital X-rays were performed on day zero, at six weeks, and twelve weeks postoperatively. After twelve weeks, spinal fusion was evaluated by 6  $\mu$ m-resolution micro-computer tomography ( $\mu$ CT) scans and on histology that was semi-quantitatively scored on sagittal-oriented toluidine/fuchsin red stained ~200- $\mu$ m-thick polymethyl methacrylate (PMMA) embedded sections (Figure 1).

## Results

At twelve weeks, 10 $\mu$ g BMP2, 1 $\mu$ g BMP-2 + 5 $\mu$ g L51P and 1 $\mu$ g BMP2 + 10 $\mu$ g L51P showed significantly higher fusion rates compared to the PBS control in X-ray analysis.  $\mu$ CT analysis showed significantly higher fusion rates for all groups compared to the control group. 1 $\mu$ g BMP2 + 1 $\mu$ g L51P demonstrated significantly higher fusion rates than 1 $\mu$ g BMP2 alone and equivalent ossification compared to 10 $\mu$ g BMP2; higher doses of L51P did not lead to a better fusion outcome. Histological analysis confirmed the radiographical and the  $\mu$ CT results using adapted Emery *et al.* (1994) scores [7] (Figures 1, 2).

Examples of Semiquantitative Ranking using 5 class scoring system based on Emery *et al.* (1994)

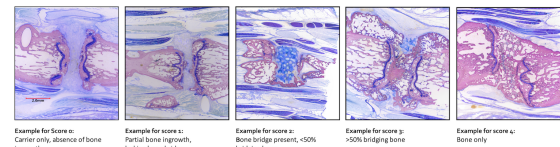


**Figure 1.** Representative images of PMMA-embedded thick sections and applied semi-quantitative histology scoring system based on Emery *et al.* (1994) [7] staining: toluidine blue/fuchsin red.

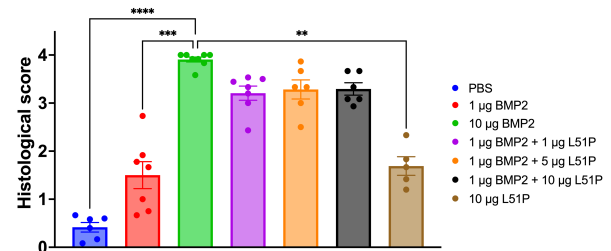


**Figure 2.** Histology scoring of PMMA-thick sections of the coccygeal spinal fusion model of elderly Wistar rat according to Emery *et al.* (1994) [7]. Mean histological scores of three independent scorers. N = 4-7. Kruskal-Wallis Dunn's corrected \*\*\*\*  $P < 0.0001$  \*\*\*  $P < 0.001$  \*\*  $P < 0.025$  \*  $P < 0.05$ .

## Conclusions

Combining low doses of L51P with BMP2 enhances spinal fusion equivalent to high-dose BMP2 and may reduce BMP2 doses and side effects at similar to higher efficacy in clinical application.

## References

1. Rajaei *et al.*, 2008. Spine 37(1):67-76, 2008.
2. Zera *et al.*, Tissue Eng Part A 17(9-10):1389-1399, 2011.
3. Martin *et al.*, Spine 32(3):382-387, 2007.
4. Khattab *et al.*, J Bone Miner Metab, 2008.
5. Sengupta *et al.*, Int J Prev Med 4(6):624-630, 2013.
6. Oswald *et al.*, Meth & Prot 4(4), 2021.
7. Emery *et al.*, J Bone Joint Surg Am 76(4):540-548, 1994.

## Acknowledgements

Funding was received from the Swiss Orthopaedics Foundation (SGOT) and the clinical trials unit (CTU) of the Insel University Hospital Bern. Further support was received by the Robert Mathys Foundation, grant number E19\_0003.





# X-RAY NANOTOMOGRAPHY OF DENTAL COMPOSITES FOR WIDE COLOR MATCHING

Dimitrios Tripkis\* (1), Mattia Humbel (1), Hans Deyhle (1), Georg Schulz (1), Mario Scheel (2), Bert Müller (1)

1. Biomaterials Science Center, University of Basel, Allschwil, Switzerland; 2. Beamline Anatomix, Synchrotron SOLEIL, Saint-Aubin, France

\*Corresponding author: d.tripkis@stud.unibas.ch

## Introduction

Caries, a global dental disease, affects billions of individuals, thus pointing out the importance of advancements in restorative dentistry. Dental resin composites, replacing metal alloys, consist of ceramic filler particles in a polymer matrix [1]. Applied as a viscous material and solidified with ultraviolet light (UV), these composites yield restorations with mechanical properties comparable to traditional fillings. Challenges in matching tooth color arise due to limited options, application changes, and color variations over time [2]. Single-shade composites with the 'chameleon effect' closely match the tooth's optical spectrum, enhancing color blending. Structural color, based on light interference, contributes to this effect. Resin composites exploit the chameleon effect for color consistency [3]. Some products, such as Filtek Universal, offer a reduced shade set while still leveraging the effect for broad tooth color coverage. The study investigates submicron filler particles' impact on optical properties and the chameleon effect.

## Material and Methods

Needle-like samples, as well as broken sample pieces glued onto a syringe needle were prepared. Several single-shade dental resin composite materials were used and a diameter of 100  $\mu\text{m}$  and a length of 10 mm with a sharp tip were targeted. The preparation included rolling out to the desired shape and curing with UV light. The samples' tips were imaged from the side in a scanning electron microscope and the diameter was measured. Finally, 3D nanotomography data were obtained through transmission X-ray microscopy (TXM) at the ANATOMIX beamline (Synchrotron SOLEIL, France) and Zernike phase contrast was used for the tips of the needles. The pixels are square and have a size of 23 nm.

## Results

Nanotomography experiments revealed the differences in the microscopic structure of four materials. In the case of Omnichroma, the filler consists of almost identical spheres with a diameter of 230 nm while in the case of Filtek Universal the size is polydisperse. Additionally, Venus Pearl One's fillers have a polyhedral shape and also a wide size distribution. Finally, the setup used did not reveal any microstructure of the Chroma Fill composite.

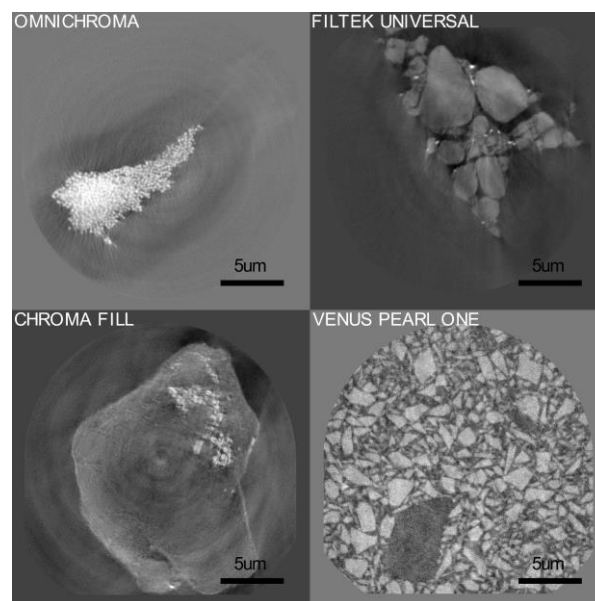


Figure 1: X-ray nanotomography slices of several single-shade materials acquired using synchrotron-radiation X-ray nanotomography.

## Discussion

The microstructure of several single-shade composite materials was revealed via transmission X-ray microscopy using Zernike phase contrast. Remarkably, the chameleon effect appears for all the materials despite their vast differences in microstructure. More research is needed to further understand the principles of the chameleon effect. For this reason, it would be useful to do spectrophotometry measurements and further structural analysis with additional microscopy methods that provide a better resolution.

## References

1. Humbel M., et al, Bioinspiration, Biomimetics, and Bioreplication XII, 12041: 2, 2022.
2. Karadas M., European Journal of Dentistry, 8: 1-2, 2014.
3. Humbel M., et al, Developments in X-ray Tomography XIV, 12242: 2, 2022.

## Acknowledgements

I thank Dr. Timm Weitkamp for the help in data reconstruction.



Annual Meeting of the Swiss Society of Biomedical Engineering  
Department of Biomedical Engineering, University of Basel, Allschwil (Switzerland)  
September 13, 2023

# EXCISCOPE POLARIS: LAB-BASED PHASE-CONTRAST CT FOR LOW CONTRAST SAMPLES

Chris Celania\* (1), Jenny Romell (1,2), and William Twengström (1)

1. Exciscope AB, Torshamnsgatan 28A, 164 40 Kista, Sweden

2. Dept. of Applied Physics, KTH Royal Institute of Technology, Stockholm, Sweden

\*Corresponding author: [chris.celania@exciscope.com](mailto:chris.celania@exciscope.com)

## Introduction

Micro computed tomography ( $\mu$ CT) is a key tool in providing 3D information of samples with  $\mu$ m resolution across a range of fields in science and technology. The two greatest challenges in  $\mu$ CT are achieving sufficient contrast and to shorten the exposure time. Contrast is challenging in soft, low atomic number materials as well as contrast between materials of similar composition. Whereas faster imaging is needed for dynamic or degrading samples, or simply to improve throughput. Phase contrast tomography overcomes the challenge of contrast [1], and has become a mainstay of synchrotron facilities, but has only begun to become commercially available for laboratory instruments.

## Material and Methods

Exciscope Polaris is a laboratory solution for faster imaging of low-contrast materials like biological tissue or polymers. Utilizing the high brightness and small spot size of a MetalJet x-ray source (Excillum AB, Stockholm, Sweden) [2] and accurate acquisition and reconstruction algorithms it enables propagation-based phase-contrast CT. With this technology, Exciscope Polaris allows a great combination of contrast, resolution, and speed, making 4D measurements of ongoing processes possible. Application examples within the fields of biomedical imaging, food and packaging, and materials science will be discussed as well as comparison scans from the TOMCAT synchrotron beamline [3].

## Results

Within the field of biomedical imaging, a lab system that can produce phase contrast CT quickly and with good contrast can revolutionize soft tissue analysis. For example, classical histology methods for analyzing tumor tissues is a relatively long process requiring several preparation steps (that are destructive processes) in order to provide high quality 2D imaging. The Exciscope Polaris has demonstrated comparable image quality to classical histology, but nondestructively while providing full 3D information on the sample [4]. As classical histology methods can still be performed after phase contrast CT analysis, the Exciscope Polaris creates the opportunity to complement histology methods, granting pathologists a powerful new tool.

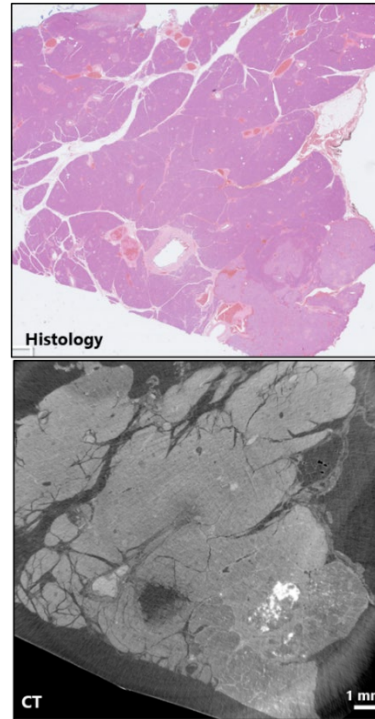


Figure 1: (top) 2D slice of pancreas tissue sample with neuroendocrine tumor: formalin-fixed, paraffin-embedded, sliced (4  $\mu$ m thick) and stained using classical histology methods and (bottom) corresponding virtual slice of the same sample (top-most layer of paraffin-embedded sample exposed after removal of layer for staining/histological analysis) scanned using propagation-based phase-contrast CT [4]

## Discussion

Exciscope Polaris provides both high performance and a great deal of flexibility. Multiple detectors allow imaging across multiple length scales and resolutions, with possibility to integrate in-situ sample environments. Image processing and reconstruction are performed with the Exciscope cloud software, allowing fast, flexible, and scalable data processing.

## References

1. A. Bravin, P. Coan, P. Suortti, Phys. Med. Biol. 58:R1–R35 2013.
2. O. Hemmberg, M. Otendal, H. M. Hertz, Appl. Phys. Lett. 83:1483, 2003.
3. A. Migga et al., J. Med. Imag. SPIE Vol. 9, No. 3:031507 2022.
4. Twengström et al, J. Med. Imag. SPIE Vol. 9 No. 3:031503 2022.



# 3D X-RAY HISTOLOGY FOR THE INVESTIGATION OF TEMPORAL LOBE EPILEPSY IN A MOUSE MODEL

Griffin Rodgers\* (1,2), Christos Bikis (1,3), Philipp Janz (4,5,6), Christine Tanner (1,2), Georg Schulz (1,2,7), Peter Thalmann (1), Carola A. Haas (4,6,8), and Bert Müller (1,2)

1. Biomaterials Science Center, Department of Biomedical Engineering, University of Basel, Switzerland; 2. Biomaterials Science Center, Department of Clinical Research, University Hospital Basel, Switzerland; 3. Integrierte Psychiatrie Winterthur—Zürcher Unterland, Switzerland; 4. Faculty of Medicine, Experimental Epilepsy Research, Department of Neurosurgery, Medical Center—University of Freiburg, Germany; 5. Faculty of Biology, University of Freiburg, Germany; 6. BrainLinks-BrainTools Center, University of Freiburg, Germany; 7. Core Facility Micro- and Nanotomography, Department of Biomedical Engineering, University of Basel, Switzerland; 8. Center of Basics in NeuroModulation, Faculty of Medicine, University of Freiburg, Germany;

\*Corresponding author: griffin.rodgers@unibas.ch

## Introduction

The most common form of epilepsy among adults is mesial temporal lobe epilepsy (mTLE), with seizures often originating in the hippocampus due to abnormal electrical activity. The gold standard for the histopathological analysis of mTLE is histology, which is a two-dimensional technique. To fill this gap, we propose complementary 3D X-ray histology. Herein, we evaluate synchrotron radiation-based phase-contrast microtomography with 1.6  $\mu\text{m}$ -wide voxels for the post mortem visualization of tissue microstructure in an intrahippocampal-kainate mouse model for mTLE [1].

## Material and Methods

We used the kainate (KA) mTLE model, whereby a stereotactic KA injection into the hippocampus induces a pathological phenotype resembling that of humans. Fifteen 9- to 12-week-old male C57BL/6N wildtype mice were used for this experiment. Label-free 3D X-ray histology with 1.6  $\mu\text{m}$ -wide voxels was used to image paraffin-embedded brain hemispheres from mice sacrificed 1, 7, 14, and 21 days after KA injection, i.e., time points representing distinct phases during epileptogenesis [2].

## Results

3D X-ray histology of unstained, unsectioned, paraffin-embedded brain hemispheres identified hippocampal sclerosis through the loss of pyramidal neurons in the first and third regions of the Cornu ammonis as well as granule cell dispersion in the dentate gyrus. Morphology and density changes during epileptogenesis were quantified by segmentations from a deep convolutional neural network. Compared to control mice, the total dentate gyrus volume doubled and the granular layer volume quadrupled 21 days after injecting KA. Subsequent sectioning of the same mouse brains allowed for benchmarking 3D X-ray histology against well-established histochemical and immunofluorescence stainings, see Figure 1.

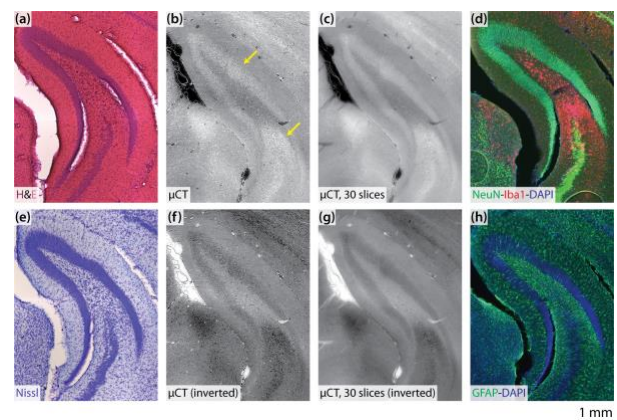


Figure 1: Benchmarking label-free 3D X-ray histology against histological and immunofluorescent stainings. Arrows indicate the granular cell layer (upper) and microglial-rich regions (lower).

## Discussion

Analysis of the volumetric data from 3D X-ray histology is distinct from conventional histology, though tools such as convolutional neural networks enable microstructural analysis without exhaustive manual labeling. Thus, 3D X-ray histology is a complementary neuroimaging tool to unlock the third dimension for the cellular-resolution histopathological analysis of mTLE. This X-ray microscopy technique will find increasing application in epilepsy research and beyond.

## References

1. Rodgers et al, *Microsc Microanal*, 00:1-16, 2023.
2. Janz et al, *Front Cell Neurosci*, 12:244, 2018.

## Acknowledgements

Beamtime for this experiment was provided by the European Synchrotron Radiation Facility (ESRF) through application MD 896. The authors thank A. Rack and the staff at beamline ID19 of ESRF for their support during the beamtime. Financial support was provided by the Swiss National Science Foundation through projects 147172, 150164, and 185058, as well as R'Equip project 133802. C.A.H. received funding from the German Research Foundation (HA 1443/11-1).





# OPTICAL COHERENCE ELASTOGRAPHY ASSESSMENT OF THE OPTOMECHANICAL EFFECTS OF CORNEAL CROSS-LINKING

Matteo Frigelli\* (1), Philippe Büchler (1), Sabine Kling (1,2)

1. ARTORG Center for Biomedical Engineering Research, University of Bern, Switzerland; 2. Institute for Biomedical Engineering, ITET department, ETH Zürich, Switzerland

\*Corresponding author: matteo.frigelli@unibe.ch

## Introduction

In the treatment of hyperopia and mild myopia, localized corneal cross-linking (CXL) has recently emerged as a promising approach, showing favorable outcomes in modifying corneal refractive power [1]. In this context the main challenge is the assessment of the relationship between the induced degree of tissue stiffening and the resulting curvature change, in order to control and predict the location and magnitude of the resulting refractive correction. Optical coherence elastography (OCE) has been proposed as a novel imaging technique to assess ocular tissues biomechanics [2]. Here, we used OCE to quantify the refractive and mechanical effects of patterned CXL, varying the irradiation energy delivered to the tissue.

## Material and Methods

9 pig eyes were subjected to a bow-tie patterned CXL treatment within 2 to 12 hours after collection. Three different protocols were tested: group A (n=3) received 3mW/cm<sup>2</sup> for 30 min (fluence of 5.4 J/cm<sup>2</sup>); group B (n=3) received 9mW/cm<sup>2</sup> for 10 min (fluence=5.4 J/cm<sup>2</sup>); group C (n=3) received 9mW/cm<sup>2</sup> for 30 min (fluence= 16.2 J/cm<sup>2</sup>). For all samples, one OCE acquisition was performed before and one 30 minutes after the patterned CXL treatment, using the experimental OCE setup schematically represented in Figure 1. OCE measurements were performed before and after stressing the cornea via the application of a mild vacuum ( $\Delta p=30$  mmHg). Axial strains in the stroma induced by the ocular inflation were computed using a previously described algorithm [3]. The anterior corneal surface was then segmented from the images and its refractive power [D] was calculated as:

$$\text{Sagittal curvature} = \frac{n-1}{R_a} \quad (1)$$

where  $n=1.3375$  is the refractive index and  $R_a$  the local sagittal radius.

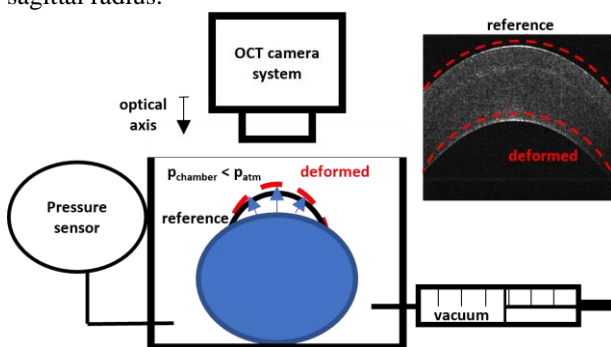


Figure 1: schematic representation of the OCE setup

## Results

A reduction in sagittal curvature and an increase in axial strain amplitude were observed in the regions treated with CXL compared to the pre-CXL condition (Figure 2). Groups A and B showed comparable increases in axial strain ( $2.1 \pm 1.1\%$  vs  $1.3 \pm 0.7\%$ ) and decreases in sagittal curvature ( $2.1 \pm 0.8D$  vs  $2.3 \pm 0.6D$ ). Group C showed a trend towards both, a greater decrease in curvature ( $3.4 \pm 0.9D$ ), and a larger increase in axial strain ( $6.7 \pm 4.1\%$ ) compared to the other groups.

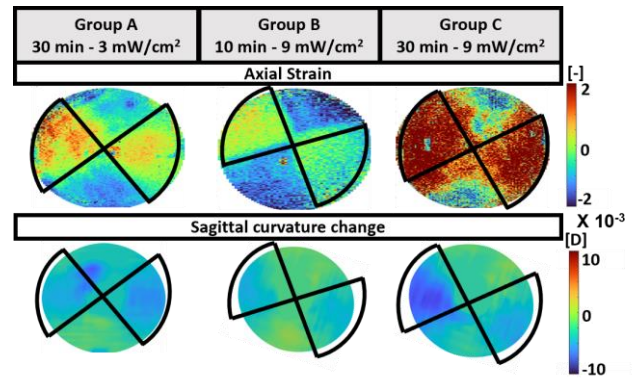


Figure 2: distinct CXL protocols optomechanical effects

## Discussion

OCE was used to quantify the relationship between refractive and mechanical changes in porcine corneas. We observed a correlation between the amount of UV energy applied to the corneal tissue during CXL and the resulting refractive correction: a threefold increase in applied energy lead to a 1.5-fold increase in refractive correction. Finally, we found that the two protocols with an energy 5.4 J/cm<sup>2</sup> but different irradiation times induced comparable mechanical response and refractive correction, which is consistent with clinical data [4].

## References

1. Sachdev et al, J Cataract Refract Surg, 46:428–433, 2020.
2. K.V. Larin et al, Biomed. Opt. Express, 8:1172-1202, 2017.
3. Kling et al, Front Bioeng Biotechnol., 7:1–13, 2020.
4. Mazzotta et al, Eye Vis., 8(1):1–12, 2021.

## Acknowledgements

This work received funding from the European Union's HORIZON 2020 research and innovation programme under grant agreement No 956720 and from the AMBIZIONE grant PZ00P2\_174113 from the Swiss National Science Foundation.





# QUANTIFICATION OF INTERNAL CRYSTALLINE LENS BIOMECHANICS STORED IN DIFFERENT PRESERVATION CONDITIONS USING OCE

Vahoura Tahsini\* (1), Philippe Büchler (1), Sabine Kling (2)

1. ARTORG Center for Biomedical Engineering Research, University of Bern, Switzerland.

2. Institute of Biomedical Engineering, ETH Zurich, Switzerland.

\* Corresponding author: vahoura.tahsini@unibe.ch

## Introduction

The crystalline lens is an important component of the visual system and responsible for accommodation and, thus, for keeping a wide range of focus. The biomechanical properties of the lens have a direct impact on the eye's refractive power. With age, the lens loses its elasticity and gets stiffer decreasing the ability to accommodate (presbyopia) [1]. Still, measuring the biomechanical properties of the lens is a challenge due to its high transparency and non-homogenous internal distribution of the materials for both ex-vivo and in-vivo.

Recently, optical coherence elastography (OCE) has been introduced as a promising tool to non-invasively assess the mechanical properties of tissues with high spatial resolution. In this study, we apply OCE ex-vivo to characterize the biomechanical properties of the lens preserved in different conditions for 24 hours.

## Material and Methods

A total of 48 lenses were obtained from the local slaughterhouse and treated as follows: 12 lenses were immediately tested as fresh lenses. Another set of eyes was tested after storage for 24 hours under different conditions: 12 eyes were preserved in the freezer, 12 eyes were stored in the refrigerator, and 12 lenses were separated from the eye globe and kept in MEM solution. For biomechanical characterization, the lenses were compressed between two glass lamellae. One lamella was attached to a piezoelectric actuator to apply a sinusoidal axial deformation stimulus. A series of 256 optical coherence tomography (OCT) B-scans were recorded to capture the corresponding lens deformation during time. The max sinusoidal oscillation applied by the piezoelectric actuator was  $36\text{ }\mu\text{m}$  with the frequency of 0.2 Hz. Internal deformations of the crystalline lens were assessed by computing the phase difference between two B scans using a complex-valued vector approach reported previously [2].

The output of the experiment was the (i) strain amplitude and (ii) phase delay between the crystalline lens cortex and nucleus to assess their stiffness and viscoelastic behavior.

## Results

Figure 1 shows a representative temporal OCE strain map. Table 1 shows the derived ratios of the strain amplitudes and the phase delay observed in the different conditions. Overall, frozen lenses presented the largest difference between the nucleus and cortex with a strain

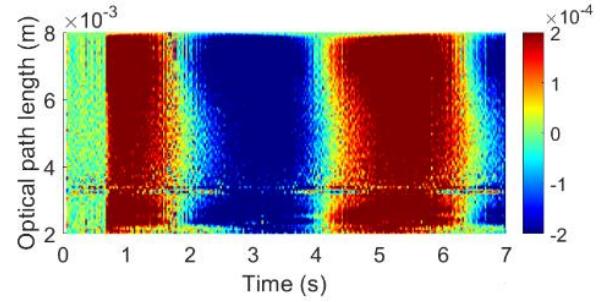


Figure 1. Representative axial strain map during lens compression as a function of time.

amplitude of 0.0213 in the cortex and 0.0084 in the nucleus. While in the fridge, MEM, and fresh lenses, the strain amplitude of the cortex measured 0.0156, 0.0165, and 0.0154, respectively, and the strain amplitude of the nucleus measured 0.0120, 0.0118, and 0.0126 respectively.

Table 1: Comparison of strain and cortex-nucleus time delay of lenses preserved in different conditions.

Sample	Nucleus:Cortex strain amp	Cortex:Nucleus time delay (s)
Frozen	$0.39 \pm 0.06$	$0.175 \pm 0.027$
Fridge	$0.79 \pm 0.09$	$0.129 \pm 0.054$
MEM	$0.74 \pm 0.10$	$0.127 \pm 0.036$
Fresh	$0.84 \pm 0.09$	$0.125 \pm 0.044$

## Discussion and Conclusions

Optical coherence elastography was able to quantify differences in the mechanical properties of the crystalline lens induced by preservation. Freezing induced substantial changes and other preservation options should be preferred.

## References

- Gerometta R, Zamudio AC, et al, *American Journal of Physiology-Cell Physiology*. 293(2):C797-C804, 2007
- Kling S, *Front Bioeng Biotechnol*. 7:453, 2020.

## Acknowledgment

This work received funding from the European Union's HORIZON 2020 research and innovation program under grant agreement No 956720.



# SMART ALIGNMENT SYSTEM FOR OPTICAL COHERENCE TOMOGRAPHY

Sébastien Muheim\* (1), Sandra Drusova (1), Arsham Hamidi (1), Ferda Canbaz\* (1)

1. Biomedical Laser and Optics Group, Department of Biomedical Engineering, University of Basel, Switzerland

\*Corresponding authors: [s.muheim@unibas.ch](mailto:s.muheim@unibas.ch), [ferda.canbaz@unibas.ch](mailto:ferda.canbaz@unibas.ch)

## Introduction

The pursuit of minimally invasive techniques in medicine has led to an increased usage of laser to diagnose and treat many diseases in various medical fields such as osteotomy, lithotripsy, ophthalmology, as well as dermatology.

Laser osteotomy has been proven to have higher accuracy and allows faster bone healing compared to conventional mechanical bone cutting [1]. During laser osteotomy, due to lack of tactile feedback, it is challenging to control the temperature, depth and shape of the cut. Optical coherence tomography (OCT) has been demonstrated to provide real-time visual feedback suitable for monitoring the procedure of laser osteotomy [2]. However, to ensure the accuracy of the depth measurement, OCT and ablative lasers must be coaxial. In this study, an algorithm is presented allowing automatic alignment of the OCT beam with the cutting laser beam and control thereof, thus improving the imaging quality of the ablation area.

## Material and Methods

A custom-made OCT system equipped with an Axsun swept laser source ( $\lambda_0 = 1060$  nm,  $\Delta\lambda = 100$  nm, and sweep rate = 100 kHz) was used to obtain top-view images through maximum intensity projection of the B-scans [2].

To detect circles the image matrixes  $f(x, y)$  are convolved with a Laplacian of Gaussian (LoG):

$$\nabla^2[G(x, y)] = \left( \frac{x^2 + y^2 - 2\sigma^2}{\sigma^4} \right) e^{-\frac{x^2 + y^2}{2\sigma^2}} \quad (1)$$

By approximating the LoG with a difference of Gaussian (DoG), the performance was increased substantially, hereafter referred to as halo detection.

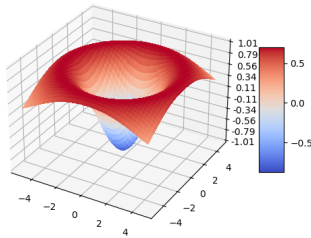


Fig. 1. Laplacian of a Gaussian.

The performance of this method was compared to the commonly used circle Hough Transform (CHT).

## Results

The halo detection shows overall better circle detection capabilities than the Hough circle method, especially in OCT enface images with high noise and low contrast. We tested 25 craters using both algorithms. All centers were detected with halo detection, whereas with CHT, 3 craters were not able to be identified.

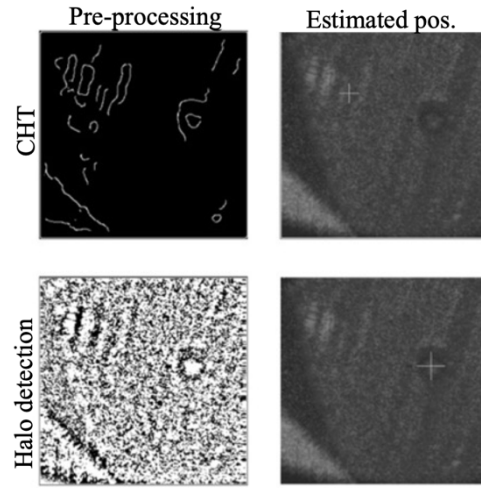


Fig. 1. Example comparison of CHT and halo detection pre-processing steps and results. A. Canny edge detection with  $\sigma=4$ , B. CHT does not detect the crater center C. Convolution with a LoG, D. Halo detection locates the crater center correctly.

## Discussion

Hough circle detection reaches its limit when the crater edges are blurry and sharper artifacts are present. Applied on OCT enface images, the halo detection method is more robust. The presented algorithm was integrated in a software program allowing to automatically find the values needed by the galvanometric motor controller to align the OCT beam to the ablative laser beam by identifying the offset of the crater centre to the image centre. Based on these preliminary results, this addition can already improve the safety and accuracy of depth measurement using OCT.

## References

1. Baek et al, J Lasers Surg Med, 47:426-432, 2015.
2. Hamidi et al, J Biomed Opt Express, 12:2118-2133, 2021.



# BUILDING PROBABILISTIC STIMULATION MAPS FOR DBS FROM HIGH RESOLUTION INTRAOPERATIVE DATA

Dorian Vogel \* (1), Karin Wårdell (2), Jérôme Coste (3),  
Jean-Jacques Lemaire (3), Simone Hemm (1,2)

1. Institute for Medical Engineering and Medical Informatics, FHNW, Switzerland; 2. Department of Biomedical Engineering, Linköping University, Sweden; 3. University Hospital Clermont-Ferrand, France

\*Corresponding author: dorian.vogel@fhnw.ch

## Introduction

Deep brain stimulation (DBS) consists in delivering electric stimulation to the brain structures responsible for movement regulation using multi-contact electrodes to control symptoms of movement disorders. To ensure proper placement of the electrode during surgery, awake intra-operative testing of symptoms is common. Normative analysis methods have been applied by other groups [1], [2] to study the mechanisms of action of DBS but focus on stimulation settings and long-term symptoms and rarely study essential tremor (ET). In comparison, intra-operative tests during awake surgery produce a large amount of exploration data. We previously presented the objectivation and automation of the intraoperative symptom scoring [3]

The study describes a method to set up disease specific DBS atlases based on intra-operative stimulation test data exemplified with data from 6 ET patients implanted in the ventro-intermediate nucleus of the thalamus (Vim).

## Material and Methods

A group specific anatomical template was created based on WAIR (white matter attenuated inversion recovery) and T1 MR (magnetic resonance) images from 19 bilaterally implanted DBS patients [4]. Deep brain structures manually delineated by the neurosurgeon [5] were projected to and summarized in the template. The distribution of the electric field (EF) was resolved for the ET patients for each position and amplitude evaluated during surgery. In each voxel, tremor improvement and EF norm were used to discriminate voxels with scores significantly above or below average using linear mixed models with patient as random effect.

## Results

The stimulation atlas describes the efficacy of DBS by combining the probabilistic anatomical template, outlines of deep brain structures and improvement scores. Voxels associated for improvement above average concentrate in the Posterior subthalamic area (infero-posterior to Vim) extending in the direction of Zona incerta and along the posterior limit of Vim (Figure 1). Voxels significant for improvement below average concentrate in the anterior and posterior limits of the region of interest.

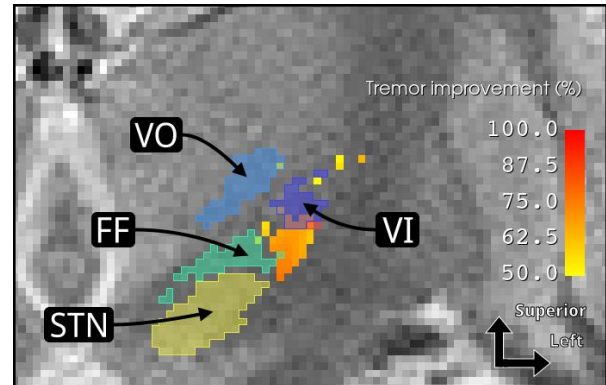


Figure 1: Coronal slice of the stimulation atlas with voxels significant for positive response to stimulation at the level of Vim. Vim: ventro-intermediate nucleus, VO: ventro-oral nucleus, FF: fields of Forel, STN: sub-thalamic nucleus

## Discussion

This study underlines the potential of the high-quality data collected during surgery for the analysis of the mechanisms of action of DBS in tremor using state-of-the-art group-analysis approaches. The low number of patients is compensated for by the high number of tests in each patient, allowing to identify significant improvement regions. The next steps are the integration of more patients and investigation in different statistical approaches to capture and quantify reliability of the results.

## References

- [1] de Roquemaurel et al., Stereotact. Funct. Neurosurg., 1–18, Jun. 2021
- [2] G. J. B. Elias et al., Ann. Neurol., 89-3:426–443, 2021
- [3] A. Shah et al., Med. Biol. Eng. Comput., 55-5:845–858, 2017
- [4] Vogel et al., NeuroImage Clin., 102271, 2020
- [5] Lemaire et al., Oper. Neurosurg., 66:161–172, 2010

## Acknowledgements

This work was financially supported by the School of Life Sciences, FHNW; the Swedish Foundation for Strategic research (BD15-0032), the Swedish research council (2016-03564) and the Swiss National Science Foundation (205320\_20749L).



# PREDICTING THE PREMORBID ANATOMY OF THE SCAPULA WITH CYCLE GENERATIVE ADVERSARIAL NETWORKS

Osman Berk Satir\* (1), Pezhman Eghbali (2), Alexandre Terrier (2, 3), Fabio Becce (3), Patrick Goetti (3), Arnaud Meylan (3), Kilian Rothenbühler (3), Philippe Büchler (1)

1. ARTORG Center for Biomedical Engineering Research, Switzerland; 2. Ecole Polytechnique Fédérale de Lausanne (EPFL), Switzerland; 3. Lausanne University Hospital (CHUV), Switzerland

\*Corresponding author: osman.satir@unibe.ch

## Introduction

Total shoulder arthroplasty is a surgical procedure to relieve pain and disability associated with glenohumeral osteoarthritis (OA). The goal is to restore the anatomy and function by replacing the deformed humeral head and glenoid cavity by placing implants. The positioning of the implants is crucial for the long-term success of the surgery [1]. Due to the bone wear caused by OA, determining the proper implant position is challenging. In addition, since OA is often bilateral, preoperative planning based on contralateral healthy morphology is not possible. Therefore, we proposed a cycle generative adversarial network (CycleGAN) based approach for objective prediction of the premorbid scapular anatomy.

## Material and Methods

Our training dataset consisted of 50 healthy and 50 pathologic segmented scapulae from CT scans. Additional 30 pathologic scapulae were used for validation. U-Net and PatchGAN were selected as generators and discriminators of CycleGAN, respectively. The goal was to create two mappings with generators that translate from pathologic to normal scapula, and vice-versa. After training, the generator that maps the pathological scapulae to normal ones was used to predict the premorbid glenoid version (GVA) of a given pathologic scapula. This method provides an objective prediction of the premorbid scapular anatomy based on the healthy cases in the dataset.

## Results

Visual comparison of the pathologic cases with their premorbid predictions showed that the shapes of the glenoid cavities were successfully restored in cases with low deformity (Fig. 1a). In the cases with extensive osteophytes, they were reduced only to a certain degree, resulting in a premorbid prediction that did not restore healthy anatomy (Fig. 1b). In addition, we investigated the difference between GVA, an important parameter for surgical planning, in pathologic cases and their premorbid predictions. In our population, glenoid was more posterior in pathologic cases than in healthy subjects, with an average difference of  $5.4^\circ$ . The same comparison between pathological cases and their premorbid predictions revealed an average correction of  $4.2^\circ$  (Fig. 2). Statistical analysis showed a significant difference between the GVA of pathologic cases and their premorbid prediction in our validation group ( $p < 0.001$ ). There was also no significant difference found

between the GVA of the healthy cases in our population and the premorbid prediction of the validation group ( $p = 0.781$ ). The findings of this study align with the existing research. In a study by Abler et al., which aims to reconstruct the premorbid anatomy of the glenoid, an average of  $6.1^\circ$  of correction was observed in 13 cases with posterior rim erosion (Walch class of B2).



Figure 1: Two examples of pathologic glenoid and their premorbid reconstruction, where the pathological osteophyte formation has been successfully (a) and only partially (b) corrected after reconstruction.

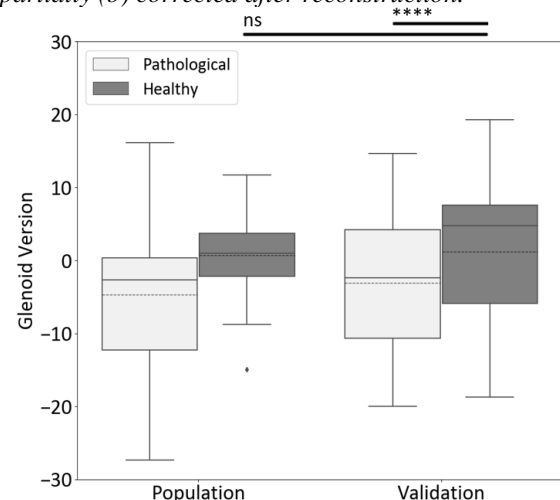


Figure 2: GVA of healthy and pathologic cases, with corresponding premorbid reconstructions

## Discussion

In this study, we proposed an approach based on CycleGAN to predict the premorbid anatomy of the scapula. Visual inspection showed that osteophytes and overall glenoid shape were successfully corrected in the less deformed glenoids. In addition, the GVA of the premorbid scapulae was restored to a similar level to the original anatomy, indicating good overall restoration of the normal glenoid shape. We will extend this work by increasing our dataset and applying the method to rotator cuff muscles to quantify muscle deformation.

## References

1. Matsen et al., J Bone Joint Surg Am., 2008
2. Abler et al., J Shoulder Elbow Surg., 2018





# USING AN SQLITE DATABASE WITH REDCAP TO ENHANCE THE CAPTURE OF BIDS METADATA

Marc Stawiski\*(1), Dorian Vogel (1), Simone Hemm (1)

1. Institute for Medical Engineering and Medical Informatics, FHNW, Switzerland

\*Corresponding author: marc.jermann@fhnw.ch

## Introduction

The usability of metadata structures, specifically the Brain Imaging Data Structure (BIDS) [1], presents challenges for analysis pipelines in brain imaging research. The limitations of BIDS in capturing detailed patient-centered information, essential for comprehensive analysis, hinder its effectiveness for clinicians using the data in their research endeavors. To overcome this limitation, our research proposes integrating an SQLite database together with the Research Electronic Data Capture (REDCap) system. This integration replaces key-value files in a JSON format, as specified by the BIDS standard, which has trouble capturing the complexity of metadata. Databases offer a reliable and efficient solution for structured data storage, and REDCap supplies a systematic approach to capturing and managing patient information [2]. This combination allows researchers to overcome the limitations of BIDS and create a more adaptable system for capturing metadata.

Our research team investigated the use of SQLite and REDCap to enhance BIDS metadata capture, yielding more impactful research by facilitating understanding of brain imaging data and patient characteristics.

## Material and Methods

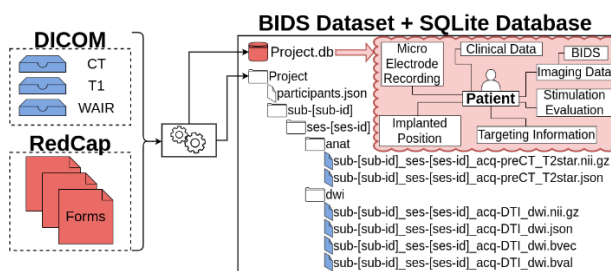


Figure 1 Data Flow Diagram

To test this configuration of REDCap in conjunction with SQLite, data was collected from two different medical centers. Patient-related metadata, including demographic information, medication and neurological assessments were transmitted using structured forms in REDCap, while medical image data was stored in DICOM format.

To prepare the data for analysis and store it in its BIDS format, a Python script was developed to convert the DICOM data to the Neuroimaging Informatics Technology Initiative (NIFTI) format and store the files following the standard. This ensured that the DICOM

files were organized and formatted according to BIDS specifications. Simultaneously, the patient metadata stored in the REDCap database was extracted and populated into an SQLite database using the same Python script. The SQLite database was designed with a patient-centric model, allowing for comprehensive storage and retrieval of the metadata (Figure 1).

## Results

Our study shows that using an SQLite database in conjunction with REDCap effectively enhances the capture of BIDS metadata, providing benefits such as improved data integrity and consistency, efficient querying and indexing, compact storage, and efficient memory usage, as well as easy backup and restore options, all within a mature ecosystem using an open standard with robust tooling support. Using this configuration, users can now execute precise patient queries with ease, as exemplified by the ability to select all images featuring patients with a specific hardware device. These findings highlight the potential of leveraging SQLite in combination with REDCap for optimizing the management and analysis of brain imaging data.

## Discussion

Overall, our approach enhances the capture and organization of BIDS metadata by using a Python script for data transfer, SQLite for metadata storage, and BIDS for standardization. This automated workflow improves efficiency and enables seamless integration for subsequent analysis pipelines.

## References

1. Gorgolewski, K. et al., Sci Data, 3, 2016.
2. Harris, P. et al., J Biomedical Informatics, 42:377-381, 2009.

## Acknowledgements

Clinical partners: We are grateful to Jean-Jacques Lemaire, Jérôme Coste, University Hospital Clermont-Ferrand, France and Peter Fuhr, Ute Gschwandtner, Ethan Taub, University Hospital Basel, Switzerland for sharing the clinical data. This work was supported by the Swiss National Science Foundation.



# TREMOR DETECTOR: ONLINE BMFLC BASED METHOD COMPARED TO OFFLINE PSD BASED METHOD

Frédéric Bourgeois\* (1), Simone Hemm (1)

1. Institute for Medical Engineering and Medical Informatics, School of Life Sciences, University of Applied Sciences and Arts Northwestern Switzerland

\*Corresponding author: frederic.bourgeois@fhnw.ch

## Introduction

Tremor is a neurological disorder characterized by an involuntary quasiperiodic movement with a dominant frequency between 3 and 12 Hz. Beside medical treatment more sophisticated methods like deep brain stimulation (DBS) can be used to alleviate the symptoms. As medical follow-up is essential for the adjustment of the treatment the detection of tremor phases can be beneficial to quantify the treatment impact. Luft et al. [1] propose the relative tremor power (RTP) based on the power spectral density (PSD) as a metric to detect tremor phases from sensor devices.

The Bandlimited Multiple Fourier Linear Combiner (BMFLC) [2] is a recursive algorithm to estimate a quasiperiodic signal modeled as a series of sine and cosine components with pre-selected frequencies. A least mean square algorithm constantly updates the estimated amplitudes and phases for each frequency providing an analog metric to the RTP based on the PSD. We previously proposed a similar online algorithm consisting of a single sine-cosine-pair [3] to identify and characterize tremor within a motion signal.

## Material and Methods

Tri-axial wrist-worn accelerometer recordings were gathered from eight patients during DBS surgery (University Hospital Clermont-Ferrand, 2011-A00774-37 / AU905). The dominant tremor axis was first identified using a principal component analysis.

The calculation of the PSD based RTP was done according to [1]. The data is first band-pass filtered (2nd-order Butterworth, 0.5-20Hz) and split into 3-second windows with 50% overlap. Using the power spectral density estimation via the periodogram method the RTP is calculated according to (1) where  $P(f_{band})$  is the power density within a certain frequency band and  $f_{peak}$  is the estimated tremor frequency.

$$RTP = \frac{P(f_{peak}-0.5Hz \text{ to } f_{peak}+0.5Hz)}{P(3.5 \text{ to } 12 \text{ Hz})} \quad (1)$$

The BMFLC model consisted of sines and cosines with fixed frequencies ranging from 3.5 to 12 Hz with 0.5 Hz spacing and an additional bias term. The adaptive gains were set to  $\mu = 0.01$  and  $\mu_{bias} = 0.01$ . The BMFLC based RTP is computed analog to (1) using the estimated amplitudes instead of the power densities.

To compare both methods the BMFLC based RTP was averaged over the same 3-second windows and the mean absolute error (MAE) was calculated.

## Results

A total of 4808 3-second windows were analyzed with both methods resulting in an overall MAE of 7.4% (std. 6.4%). A Wilcoxon signed-rank test ( $z=1.80$ ,  $p>0.05$ ) did not reject the null hypothesis (MAE=0%) suggesting similar results for both RTPs (Figure 1). A calculated mean error of -0.2% denotes a slightly underestimation of the BMFLC based RTP.

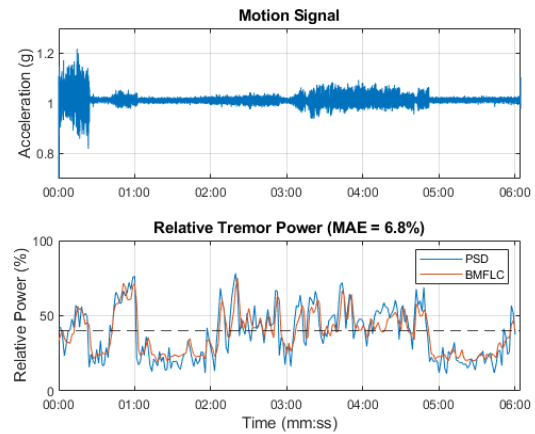


Figure 1: PSD (blue) and BMFLC (orange) based RTP from an exemplary motion signal.

In [1] the phases are classified by comparing the RTP to a threshold value of 40%. Using this hard threshold, the same classification is obtained for 89% of the windows.

## Discussion

The BMFLC method can be used as an online alternative to the PSD method for tremor phase detection, although the threshold criteria may need some adaptation. Besides being an online recursive algorithm the BMFLC method requires no other filters to estimate the RTP and is easily tunable via the adaptive gains.

## References

1. Luft F et al, Sensors (Basel), 19(19):4301, 2019.
2. Veluvolu K et al, Annu Int Conf IEEE Eng Med Biol Soc. 2007, 2847-50, 2007.
3. Bourgeois F et al, Current Directions in Biomedical Engineering, 8(2):105-108, 2022.

## Acknowledgements

We thank Jérôme Coste from the Université Clermont Auvergne for collecting the data during the DBS surgeries.



# THE SCENT OF PAIN: METABOLIC FINGERPRINTS OF COLD PRESSOR TEST VIA REAL-TIME BREATH ANALYSIS IN A MULTISITE CLINICAL TRIAL

Mélina Richard (1), Dilan Sezer (2), Sarah Bürgler (2), Luana Palermo (2), Yannick Schulz (2), Zhifeng Tang (3), Xin Luo (3), Xue Li (3), Jens Gaab (2), Pablo Sinues (1)

1 University Children's Hospital Basel (UKBB), Department of Biomedical Engineering; University of Basel, Switzerland

2. Faculty of Psychology; University of Basel, Switzerland

3. Institute of Mass Spectrometry and Atmospheric Environment, Jinan University, P.R.China

\*Corresponding author: melinadenise.richard@unibas.ch

## Introduction

Olfactory cues may convey pain to others [1]. Up until recently blood and urine were the only easily accessible tissues for understanding the biochemical mechanisms of pain in experimental studies of humans [2, 3]. Here we propose for the first time a real-time non-invasive assessment of biochemical changes of experimentally induced pain via cold pressor test (CPT) by harnessing the metabolome via exhaled breath.

Metabolites have been demonstrated to have exceptional predictive abilities and to closely mirror the actual phenotype [4,5] and are therefore an important step towards improved diagnostics and treatment, furthermore, providing an important path towards personalized medicine [6,7] including the treatment of pain.

A diagnostic difficulty for healthcare providers is the frequent disparity between peripheral sources of pain and the severity of pain and impairment. It is frequently impossible to detect tissue injury, inflammation, or peripheral sensitization, or if detected, it is insufficient to explain the reported pain intensity, disability, and accompanying symptoms. [8] Hence it is important to investigate further into underlying molecular mechanisms associated with pain responses. In this multisite clinical trial, we applied the CPT which is arguably the most popular pain-provocation test in history [2, 9] and measured the exhaled metabolome before and after CPT.

## Material and Methods

We conducted the study at two sites: Switzerland (CH, n=19) and China (CN, n=21). Exhaled breath metabolome was analyzed using Secondary Electrospray Ionization-High Resolution Mass Spectrometry (SESI-HRMS). Each participant performed two sets of exhalations before and after the CPT, with six exhalations in positive and negative modes respectively. A total of 1920 exhalations were examined using standard univariate and multivariate data analysis strategies.

## Results

Both for the participants in CH and CN, significant changes in peaks before and after the CPT were observed. We found an overlap of 137 significant features [False Discovery Rate (FDR) < 0.01, log<sub>2</sub>(fold

change) (FC) > 2] between the two study sites with a consistent up-/down-regulation behavior.

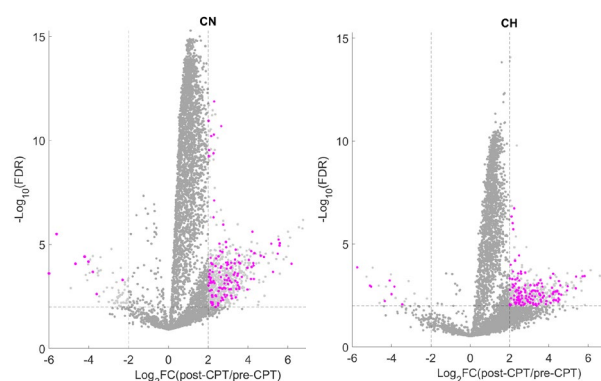


Figure 1. Volcano Plot of all 5058 Metabolic Features in CH and CH. Pink features are the overlap of 137 significant features (FDR 0.01, log<sub>2</sub>fold change > 2) between the two study sites for pre-post CPT intervention.

## Discussion

Altered metabolite abundances suggest a metabolic response to CPT induced pain. The overlapping features in both study sites indicate consistent metabolic changes associated with pain across populations. We are currently conducting enrichment analysis to investigate the correlation networks of involved metabolic pathways.

## References

1. Lötsch, J., et al., PAIN, 157(10): 2152-2157, 2016
2. Kogelman, L.J.A., et al., BMC Genomics, 23(1): 759., 2022.
3. Hsu, W.H., et al., Eur J Pain, 26(2): 445-462, 2022.
4. Rohde, P.D., et al., Heredity (Edinb), 126(5): 717-732, 2021
5. Zhou, S., et al., Genome Res, 30(3): 392-405, 2020.
6. Castelli, F.A., et al., Anal Bioanal Chem, 414(2): 759-789, 2022.
7. Jacob, M., et al., Mass Spectrom Rev, 38(3): 221-238, 2019.
8. Nijs, J., et al., The Lancet Rheumatology, 3(5): 383-e392, 2021
9. Modir, J.G. and M.S. Wallace, Humana Press: Totowa, NJ., 165-168, 2010.





# PERSONALISED THERAPEUTIC MANAGEMENT OF EPILEPTIC PATIENTS GUIDED BY PATHWAY-DRIVEN BREATH METABOLOMICS

Kapil Dev Singh (1,2), Martin Osswald (3), Victoria C. Ziesenitz (1), Mo Awchi (1,2), Jakob Usemann (1), Lukas L. Imbach (3), Malcolm Kohler (3), Diego García-Gómez (4), Johannes van den Anker (1), Urs Frey (1,2), Alexandre N. Datta (1), Pablo Sinues\* (1,2)

1. University Children's Hospital Basel, University of Basel, Basel, Switzerland; 2. Department of Biomedical Engineering, University of Basel, Basel, Switzerland; 3. University Hospital Zurich, University of Zurich, Zurich, Switzerland; 4. Department of Analytical Chemistry, University of Salamanca, Salamanca, Spain

\*Corresponding author: pablo.sinues@unibas.ch

## Introduction

Therapeutic management of epilepsy remains a challenge, since optimal systemic antiseizure medication (ASM) concentrations do not always correlate with improved clinical outcome and minimal side effects [1]. We tested the feasibility of noninvasive real-time breath metabolomics as an extension of traditional therapeutic drug monitoring for patient stratification by simultaneously monitoring drug-related and drug-modulated metabolites.

## Material and Methods

This proof-of-principle observational study involved 93 breath measurements from 54 paediatric patients monitored over a period of 2.5 years, along with an adult's cohort of 37 measurement from 37 patients measured in two different hospitals (UKBB and USZ). Exhaled breath metabolome of epileptic patients was measured in real time using secondary electrospray ionisation–high-resolution mass spectrometry (SESI–HRMS).

We trained (on 75 measurement from UKBB) a regression model based on Gaussian process regression using exponential kernel (eGPR) to predict (independent 18 measurements from UKBB and 37 measurements from USZ) the total and free serum valproic acid (VPA, an ASM) concentration, based on the signal of 11 VPA-related ions detected in exhaled breath. For further details see our published article [2].

## Results

We show that systemic ASM concentrations could be predicted by the breath test. Total and free VPA is predicted with concordance correlation coefficient (CCC) of 0.63 and 0.66, respectively (Figure 1). We also find (i) high between- and within-subject heterogeneity in VPA metabolism; (ii) several amino acid metabolic pathways are significantly enriched ( $p < 0.01$ ) in patients suffering from side effects; (iii) tyrosine metabolism is significantly enriched ( $p < 0.001$ ), with downregulated pathway compounds in non-responders.

## Discussion

In this translational study, by combining real-time, noninvasive and rapid breath analysis with

sophisticated bioinformatics tools, we showed that systemic total VPA concentrations can be predicted (Figure 1a).

However, it has been shown previously that free VPA is physiologically active and clinically relevant, which stresses the importance of measuring free VPA concentration [3]. In spite of this, current clinical practice relies most often on total VPA blood levels, perhaps due to the fact that determination of free VPA requires relatively large blood volumes, lengthy and laborious mass spectrometric analyses requiring hours-to-days of laboratory work. Here we showed the possibility of predicting free VPA concentrations in 15 min by a simple non-invasive breath test (Figure 1b).

In conclusion, these results show that real-time breath analysis of epileptic patients provides reliable estimations of systemic drug concentrations along with risk estimates for drug response and side effects.

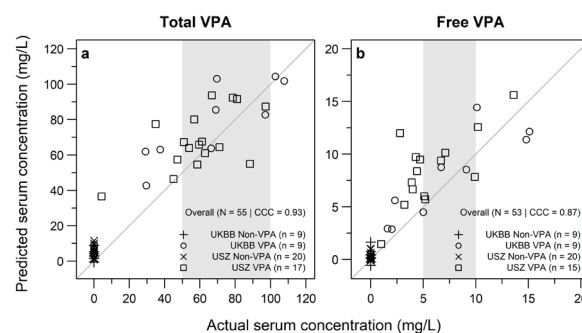


Figure 1: Prediction of systemic drug concentration based on real-time breath mass spectra for total (a) and free (b) VPA.

## References

1. Kang, J. S. & Lee, M. H., Korean J. Intern. Med, 24:1–10, 2009.
2. Singh, K.D. et al., Commun Med, 1:21, 2021.
3. Sproule, B. et al., Ther. Drug Monit, 28:714–715, 2006.



# ELECTROPHYSIOLOGICAL MEASUREMENTS DURING AND AFTER COCHLEAR IMPLANTATION

Marlies Geys\* (1), Leanne Sijgers (1), Alexander Huber (1), Ahmet Kunut (1), Adrian Dalbert (1), Flurin Pfiffner (1)

1. Department of Otorhinolaryngology, Head&Neck Surgery, University Hospital Zurich, University of Zurich, Switzerland

\*Corresponding author: marlies.geys@usz.ch

## Introduction

A cochlear implant (CI) is one of the most successful neuroprosthetic that can restore hearing of patients with severe to profound hearing loss. In the recent years, the use of electrocochleography (ECoChG) to monitor the cochlear health during surgery has been investigated [1]. ECoChG is the recording of electrical potentials generated by the cochlea in the inner ear, in response to acoustic stimulation. In CI users with residual hearing, ECoChG responses recorded using the CI's intracochlear electrodes can provide valuable information regarding the hair cell and neural health surrounding the recording electrodes at different regions in the cochlea [2]. As the cochlea is tonotopically organized, the highest ECoChG amplitudes are expected at the most apical electrodes when stimulating with a low frequency (figure 1, A). However, different patterns with maximal amplitudes in the more basal regions of the cochlea have been reported [3] (figure 1, B). The aim of this study is to investigate if different ECoChG patterns change the cochlear health in the initial year following CI surgery.

## Material and Methods

Fifteen subjects with residual acoustic hearing undergoing CI surgery at the University Hospital of Zurich were included in this study. ECoChG responses to 500 Hz tone bursts were recorded with different electrodes of the electrode array at three different time-points: intraoperatively after full CI electrode array insertion, between four and twelve weeks postoperatively, and after one year of CI activation. Pure Tone Audiometry (PTA) was performed preoperatively, approximately six weeks post-surgery, and after one year of CI activation. Hearing loss after surgery and further hearing reduction between six weeks post-surgery and one year will be analyzed between the two groups (typical and atypical ECoChG peak patterns).

## Results

Preliminary results show that intraoperative atypical ECoChG peak patterns, with a maximum in the more basal region, remain stable after six weeks and one year after implantation. Residual hearing was reduced six weeks after implantation but no further reduction was measured after one year in patients with a more basal peak pattern.

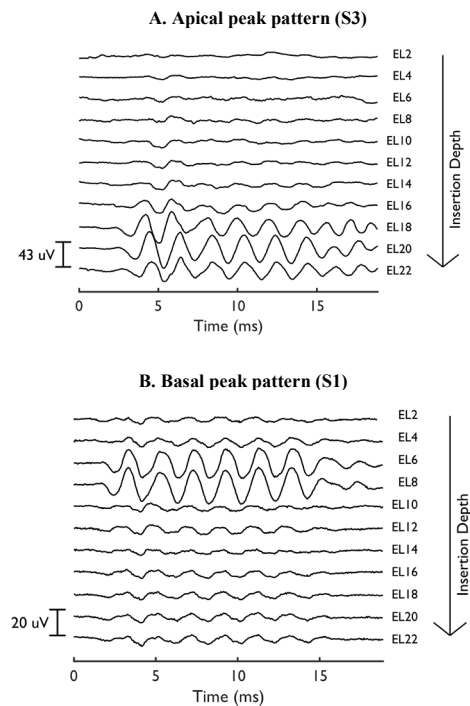


Figure 1: Intraoperative time signal of ECoChG responses measured on every second electrode during electrode array insertion. Electrode 22 is the most apical electrode of the array. **A** Apical ECoChG peak pattern in subject 3. **B** Basal ECoChG peak pattern in subject 1.

## Discussion

More basal ECoChG peak patterns can indicate a region of better cochlear health or a change in the inner ear mechanics due to cochlear implantation. Atypical peak patterns can lead to a reduction in residual hearing within first 6 weeks following cochlear implantation. However, it does not necessarily lead to changes of cochlear health or further deterioration of acoustic hearing thresholds after one year of CI use.

## References

1. Trecca et al., Otol Neurotol, 41(7): 864-878, 2020.
2. Campbell et al., Audiol Neurotol, 22:180-189, 2017.
3. Bester et al., Front. Neuroscience, 11, 2017.



# NEURAL SPIKE DETECTION AND SORTING WITH AUTONOMOUS LINEAR STATE SPACE MODELS

Christof Baeriswyl\* (1,2), Alexander Bertrand (2), Reto A. Wildhaber (3)

1. KU Leuven, Belgium; 2. Berner Fachhochschule, Switzerland (CH); 3. Fachhochschule Nordwestschweiz, CH

\*Corresponding author: christof.baeriswyl@esat.kuleuven.be

## Introduction

Neural spike sorting, a crucial step in analyzing extracellular neural activity, presents a significant challenge in neurophysiological research. In this study, we use a micro-electrode array with 384 electrodes densely packed on a mice cortex. Each firing neuron generates a unique spike pattern on the electrodes, necessitating accurate separation from other signals. We approach this problem as a source separation and (un)supervised machine learning task:

1. Learn distinct multi-channel spike patterns.
2. Detect recurring instances of spikes in recording.
3. Efficiently sort and assign spikes to their respective neurons.

**Approach:** Likelihood filtering based on linear filters.

## Method: Recursive Least Squares

### Signal Modelling with Polynomials

Autonomous linear state space models (ALSSM) are used for an efficient calculation of a recursive least squares (RLS) fit [2] of a signal model to an observation. Neural spikes are modelled with damped 4th order polynomials, and the shared baseline is modelled with a 3th order polynomial. The models are at the minimum of the L2-norm

$$J_k(x) = \|y - s_{i-k}(x)\|_{w_k}^2 \in \mathbb{R}$$

$$\hat{x} = \underset{x}{\operatorname{argmin}} J_k(x) \in \mathbb{R}^N,$$

where  $y \in \mathbb{R}^K$ ,  $K \in \mathbb{N}$  is an observation and  $s_i(x) \in \mathbb{R}$  is the model output of an ALSSM of size  $N$ .

### Spike Detection on Recorded Data

Assumption: spike templates are known (learned). Detection with likelihood-ratio between two hypotheses:

$$\text{LLR}_k = -\frac{1}{2} \log \left( \frac{J_k(\text{"spike"} + \text{"baseline"})}{J_k(\text{"baseline"})} \right) \in \mathbb{R}$$

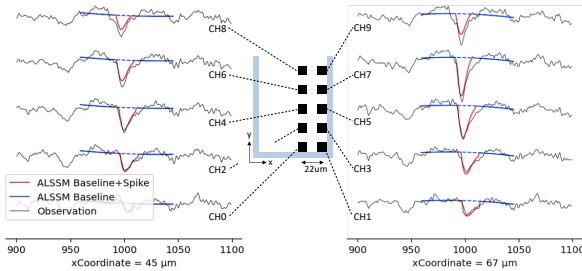


Figure 1: Multi channel observation of a neural spike and ALSSM model outputs with shared baseline and channel-wise neural spike fit.

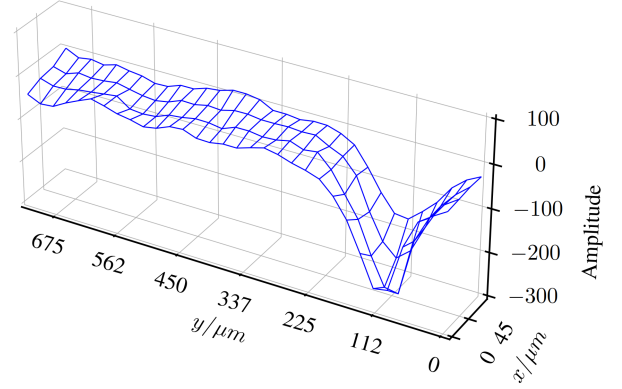


Figure 2: Spatial plot of a single neuron spike from a micro-electrode array probe on a mouse cortex. The probe spans an area of 70 x 720 µm. Data: [1]

## Results

Table 1: Filter and threshold-based spike sorting performance in terms of sensitivity (recall) and precision. 15 known neurons were cut and pasted into different channels and locations with SHYBRID [3] to generate a (partial) ground truth. Threshold on LLR is used as a binary classifier. In total, 5 minutes of recordings at 30kHz were processed. Neurons are grouped according to their performance.

Neurons N°	Sensitivity	Precision	F1 score
1-5	0.95	0.94	0.94
6-10	0.81	0.86	0.83
11-15	0.73	0.68	0.69

## Discussion

Spike sorting with ALSSMs offers similar performance as Finite Impulse Response (FIR) matched filters, while recursive least squares computation and sharing of intermediate results make the ALSSM method computationally more efficient. As an outlook, impulse responses of Signal-to-Peak-Interference optimal filters may be approximated by ALSSMs, solving the problem of overlapping spikes [2].

## References

1. Steinmetz et al., Dataset, 2019, <https://doi.org/10.6084/m9.figshare.7666892.v2>.
2. Baeriswyl et al., 30th European Signal Processing Conference (EUSIPCO), pp. 1208-1212, 2022.
3. Wouters et al., Neuroinformatics 19: 141-158, 2021.



# DETECTION OF NOCTURNAL HYPOGLYCAEMIA USING NON-INVASIVE SENSORS IN PEOPLE WITH DIABETES

C. Mendez Schneider (1,2,3), M. Rothenbühler (2), D. Hadorn (4), M. Laimer (1),  
L. Witthauer\* (1,2)

1 Department of Diabetes, Endocrinology, Nutritional Medicine and Metabolism, Inselspital, Bern University Hospital, University of Bern, Bern, Switzerland; 2 Diabetes Center Berne, Bern, Switzerland;

3 Graduate School for Cellular and Biomedical Sciences, University of Bern, Bern, Switzerland;

4 QUMEA AG, Solothurn, Switzerland

\*Corresponding author: [lilian.witthauer@unibe.ch](mailto:lilian.witthauer@unibe.ch)

## Introduction

Managing diabetes includes a tight glycemic control which was shown to be associated with a higher risk for hypoglycaemia. Acute clinical consequences of hypoglycaemia include reduced motor control, arrhythmias and even death. Almost half of all hypoglycemic episodes occur at night [1]. Advances in sensor technologies allow for non-invasive monitoring of changes in physiological parameters in people at risk of nocturnal hypoglycaemia. It has been shown that physiological changes can be attributed to hypoglycaemic episodes using machine learning models [2]. Thus, we examined a novel nocturnal hypoglycaemia warning system consisting of a ceiling mounted radar sensor, non-invasive wearables, and advanced algorithms.

## Material and Methods

In a pilot study, data on movement during sleep were collected using a radar-based patient monitoring system (Qumea, Solothurn). Additionally, participants wore two smartwatches (Garmin Venu 2 and Fitbit Sense 2) that collected data on heart rate, heart rate variability, breathing rate, temperature, and sleep phases. All participants were equipped with a CGM system (Dexcom G6) and performed capillary blood glucose measurements to calibrate the CGM system. Data was collected for 10 consecutive nights at the patient's homes. The study includes adults with diabetes mellitus on an insulin therapy. Patients with cardiac arrhythmias, antiarrhythmic drugs, beta-blockers, or any illness or use of medications that could affect sleep patterns, including sleep apnea, were excluded. In a preliminary analysis with data from one participant, data was partitioned into samples of five minutes and labelled with "euglycemia" and "hypoglycemia". For each sample, cardiac and respiratory features were employed as predictor variables for a logistic regression model.

## Results

The study is expected to be completed by June 2024. Currently, data from 100 nights for N=10 participants was collected. 19 episodes of level 1 hypoglycaemia ( $\leq 3.9$  mmol/L) and 5 episodes of level 2 hypoglycaemia ( $< 3.0$  mmol/L) were identified during sleep. Each hypoglycaemic episode lasted for at least 20 minutes.

Table 1: Preliminary results: Logistic regression analysis employing data from smartwatches was performed on a training set (N=102) and tested on a test set (N=26). The model's performance is summarized in the confusion matrix.

	Predicted Euglycemia	Predicted Hypoglycemia
Actual Euglycemia	9	5
Actual Hypoglycemia	4	8

## Discussion

Preliminary results suggest correlations between low nocturnal glucose levels and physiological changes. The combination of smart algorithms and both radar-based patient monitoring system and wearable sensors holds great promise to simplify diabetes management, reducing the risk of nocturnal hypoglycaemia, with the potential to reduce healthcare costs.

Table 2: Baseline characteristics of study participants. MDI, multiple daily injection; CSII, continuous subcutaneous insulin infusion; HCL, hybrid closed loop; HbA<sub>1c</sub> glycated hemoglobin.

Variable	Value
Participants, N	10
Age, mean $\pm$ SD [years]	33.9 $\pm$ 19
Sex [male/female]	4/6
Diabetes type	
[Type 1/ Pancreatogenic]	9/1
Insulin treatment	
[MDI/CSII/HCL]	4/4/2
BMI, mean $\pm$ SD [kg/m <sup>2</sup> ]	24.9 $\pm$ 3.9
HbA <sub>1c</sub> , mean $\pm$ SD [mmol/mol]	7.3 $\pm$ 0.8

## References

1. Unger et al, Postgrad Med, 123(4):81-91, 2011.
2. Lehmann et al, Diabetes Care, 46(5):993-997, 2023.

## Acknowledgements

This work was supported by the Diabetes Center Berne Foundation, Vontobel Foundation under application No. 0847/2022, and Innosuisse under funding application No. 62023.1 INNO-LS.



Annual Meeting of the Swiss Society of Biomedical Engineering  
Department of Biomedical Engineering, University of Basel, Allschwil (Switzerland)  
September 13, 2023



# NAVIGATING FLEXIBLE MEDICAL INSTRUMENTS USING FIBER SENSORS AND DEEP LEARNING

Samaneh Manavi Roodsari\* (1), Martin Angelmahr (2), Wolfgang Schade (2), and Philippe C Cattin (1)

1. University of Basel, Department of Biomedical Engineering, Center for medical Image Analysis and Navigation (CIAN), Hegenheimermattweg 167C, Allschwil 4123, Switzerland
2. Fraunhofer Institute for Telecommunications, Heinrich Hertz Institute, HHI, Goslar 38640, Germany

\*Corresponding author: samaneh.manavi@unibas.ch

## Introduction

Optical fiber shape sensing is a revolutionary technology with a wide range of medical and industrial applications. It enables the tracking of endoscopes, catheters, and flexible robots, among other uses. Optical fibers, which are glass wires twice as thick as human hair, have the unique ability to guide light over long distances with low energy loss. By incorporating specific structures along their length to deliberately perturb the light and capture reflected portions, optical fibers can be utilized for shape sensing. Despite the potential of optical fiber shape sensors, the currently available commercial solutions offer only millimeter-level accuracy and come with a high price tag of over 100,000 CHF. This significantly hinders their practicality and limits their widespread adoption.

Over the past few years, we have developed a cost-effective fiber shape sensing solution based on eccentric fiber Bragg gratings (eFBG). eFBGs (depicted in Figure 1) are highly localized FBGs inscribed off-axis in the core of an optical fiber, designed by our collaborators at Fraunhofer HHI in Germany. These specific types of fiber sensors show great potential for shape-sensing applications thanks to their unique sensing mechanism. Despite their many advantages, accurate shape estimation in such sensors is still an open question, which we have addressed in this study.

## Material and Methods

We developed a deep learning algorithm, fine-tuned using the Hyperband optimization algorithm [1], to predict multi-bend shapes of the eFBG sensor directly from its spectrum (Figure 2). The dataset used for training and testing the deep learning model was acquired by randomly deforming the sensor for 30 minutes while recording its spectra and true shape. The reader is referred to [2, 3, 4] for further details.

## Results

With this approach, we achieved a shape prediction accuracy that is competitive with the state-of-the-art distributed fiber shape sensors and can estimate complex multi-bend shapes of a 30 cm long sensor with only a 2 mm tip error [2].

## Discussion

Our research presents a promising approach to fiber shape sensing by combining an easy-to-fabricate eFBG

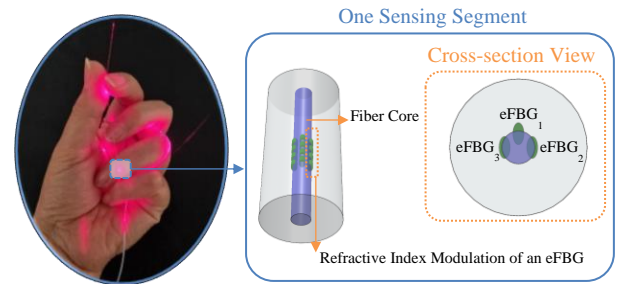


Figure 1. The eFBG shape sensor wrapped around fingers. Each sensing segment contains three eFBGs.

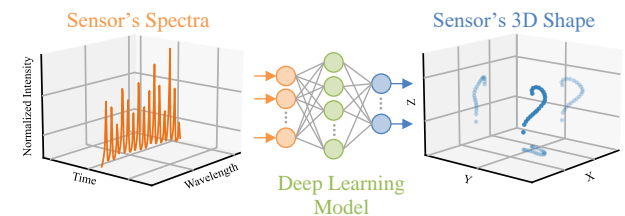


Figure 2. The deep learning model extracts essential features from the sensor's spectra and accurately predicts its corresponding shape. The input spectrum captures the Bragg signal of 15 embedded eFBGs, while the output comprises 20 discrete points along the sensor's shape. More details available in [2, 3].

sensor and a data-driven deep learning model. This approach eliminates the need for conventional computation steps for elaborating the sensor's signal and results in more precise shape estimations, overcoming the limitations of traditional methods. We believe that this work has the potential to drive advancements in efficient and cost-effective shape sensing across various applications, especially in the medical field.

## References

1. K. Li, et al., The J. Mach. Learn. Res. 18: 6765-6816, 2017.
2. S. Manavi Roodsari, et al., arXiv:2210.16316 [cs.LG].
3. S. Manavi Roodsari, et al., Mach. Learn.: Sci. Technol., 2023.
4. S. Manavi Roodsari, et al., Optical Sensors. 11772: 79-88, SPIE, 2021.

## Acknowledgments

We gratefully acknowledge the funding of this work by the Werner Siemens Foundation through the MIRACLE project.



# FORCES APPLIED DURING ULTRASONIC SCALING

Diego Stutzer\* (1), Martin Hofmann (2), Dominik Wenger (1), Khaled Harmouch (3), Sigrun Eick (4),  
Jürgen Burger (2), Thomas Niederhauser (1)

1. Institute for Human Centered Engineering, Bern University of Applied Sciences, Biel, Switzerland,

2. School of Biomedical and Precision Engineering, University of Bern, Bern, Switzerland,

3. Electro Medical Systems S.A., Nyon, Switzerland,

4. Laboratory of Oral Microbiology, Department of Periodontology, University of Bern, Bern, Switzerland.

\*Corresponding author: diego.stutzer@bfh.ch

## Introduction

Dental biofilm and calculus are the leading causes of caries and periodontal diseases and affect most adults during their lifetime. Ultrasonic scalers are widely used to remove dental biofilm and calculus to prevent and treat periodontal diseases. Several studies [1-3] indicate that applying higher force can increase dentin loss and cause tooth damage. Furthermore, the applied force influences ultrasonic scalers' characteristics and is an essential parameter for developing new instruments. However, information about the magnitude, direction, and variation of the force applied during ultrasonic debridement is very limited [4].

The present study investigates the magnitude, direction, and temporal aspects of the force applied during ultrasonic scaling.

## Material and Methods

The study included six dentists. Each dentist cleaned a predefined area covered with comparatively soft ( $4.6 \pm 0.8$  HV) and comparatively hard ( $24 \pm 4.9$  HV) artificial calculus [5] using a commercially available ultrasonic piezoelectric scaler (PIEZON, E.M.S. SA, Nyon, Switzerland). The force applied by the professionals during the debridement was recorded using a custom-built measurement system comprising a three-axis force sensor (ZM3DW-AL 10N, Anhui Zhimin El. Tech., Bengbu, China), a data acquisition module (USB-6366, National Instr. Corp., Austin, USA), and a computer. Additionally, the position of the scaler relative to the calculus surface was recorded by a video camera. Scripts for MATLAB (MathWorks Inc., Natick, USA) were used for filtering, calculations, and to illustrate the results.

## Results

As indicated by the numerical values in Table 1, the median total force applied during scaling on hard artificial calculus was more than twice as big as the force applied to remove comparatively soft artificial calculus. Furthermore, the total force exceeded the manufacturer's recommendation to apply  $<0.1$  Newton. Strong and fast variations of the total force were also considerably more frequent when hard artificial calculus was removed. In contrast, the calculus hardness only marginally influenced the maximum total

force. Furthermore, the measurements revealed that the median value of the force perpendicular to the surface of the calculus or tooth is more than twice as high as parallel to it. Finally, the measurements document that the applied force varies considerably among different individuals and that the usage of the scaler deviated from recommended practices occasionally.

## Conclusion

This study documented the influence of calculus hardness on the magnitude and direction of the force applied by professionals during ultrasonic debridement and contributing factors. The results may raise awareness about the risk of unintentionally applying excessive and potentially detrimental force. Furthermore, the results can support the development of new ultrasonic scalers to optimize their performance in clinical use.

Table 1: Statistical values of the force applied by six dentists scaling soft and hard artificial calculus. Numerical values indicate: median (IQR) / max.

	Soft artificial calculus	Hard artificial calculus
Total force [N]	0.18 (0.15) / 1.95	0.50 (0.36) / 2.22
Force parallel to surface [N]	0.08 (0.06) / 0.58	0.17 (0.20) / 1.58
Force perpendicular to surface [N]	0.16 (0.16) / 1.90	0.45 (0.34) / 1.78
Absolute of time derivative of total force [N/s]	0.66 (1.00) / 18.73	1.34 (1.90) / 58.56

## References

1. Flemming et al, J Periodont, 69 5:547-53, 1998.
2. Schmidlin et al, J Clin Periodont, 28 11:1058-66, 2001.
3. Yousefimanesh et al, J Perio & Impl Sc, 42:243-47, 2012.
4. Ruppert et al, J Periodont, 73 4:419-22, 2002.
5. Stutzer et al, Sensors and Act A: Phys, 351:114131, 2023.

## Acknowledgments

This work has been supported by the Swiss Innovation Agency Innosuisse (Project Grant Nr. 34901.1 IP-LS).



Annual Meeting of the Swiss Society of Biomedical Engineering  
Department of Biomedical Engineering, University of Basel, Allschwil (Switzerland)  
September 13, 2023

# LOAD-INDUCED SCAPULA ROTATION DURING A 30° LOADED ARM ABDUCTION TEST IN ROTATOR CUFF TEARS AND CONTROLS

Eleonora Croci\* (1,2), Hanspeter Hess (3), Jeremy Genter (1,2,4), Cornelia Baum (2), Balazs Kovacs (5), Corina Nüesch (1,2,6,7), Daniel Baumgartner (4), Kate Gerber (3), Andres March Müller (2), Annegret Mündermann (1,2,6,7)

1.Department of Biomedical Engineering, University of Basel; 2.Department of Orthopaedics and Traumatology, University Hospital Basel; 3.School for Biomedical and Precision Engineering, University of Bern; 4.Institute of Mechanical Systems, Zurich University of Applied Sciences; 5.Department of Radiology, University Hospital Basel; 6. Department of Spine Surgery, University Hospital Basel; 7.Department of Clinical Research, University of Basel.

\*Corresponding author: eleonora.croci@unibas.ch

## Introduction

Rotator cuff tears are commonly associated with age and glenohumeral joint instability [1], but this is not yet fully understood. A superior glenohumeral translation is likely to occur, however, scapula rotation might also be affected. The aim of this study was to investigate scapula rotations during a 30° loaded abduction test after rotator cuff tears with single-plane fluoroscopy.

## Material and Methods

Twenty-five patients with unilateral symptomatic rotator cuff tears ( $64.3 \pm 10.2$  years), 25 asymptomatic control subjects ( $55.4 \pm 8.2$  years) and 25 healthy control subjects ( $26.1 \pm 2.3$  years) participated in this study. Shoulders were grouped according to the findings of magnetic resonance images (MRI) in healthy ( $n = 43$ ), rotator cuff tendinopathy ( $n = 24$ ), asymptomatic ( $n = 38$ ) and symptomatic ( $n = 25$ ) rotator cuff tears. Twenty shoulders were discarded due to absence of MRI or other findings not involving the rotator cuff. All subjects executed a 30° arm abduction and adduction movement in the scapular plane with and without additional handheld weights (0, 2 and 4 kg). Single-plane fluoroscopy images were acquired for all shoulders and were labelled with a deep learning based automatic landmark detection algorithm (accuracy: 1.5 mm, 1°) [2]. Downward-upward scapula rotations were measured throughout the entire motion, considering the scapular landmarks. The range of rotation during abduction and adduction was analysed with a linear mixed model (loads, shoulder types) with shoulder IDs as random effects to assess differences from healthy shoulders.

## Results

Upward scapula rotations during abduction are shown in Figure 1, during adduction similar values were found but in the opposite direction (downward scapula rotations). There was a significant effect for load ( $p < 0.001$ ) and rotator cuff tendinopathy ( $p = 0.047$ ) and a significant interaction effect of these two ( $p = 0.006$ ) during abduction. During adduction, we detected a significant effect for load ( $p < 0.001$ ) and asymptomatic rotator cuff tears ( $p = 0.043$ ) and a significant interaction

effect of load and RC tendinopathy ( $p = 0.013$ ). Post-hoc tests showed significant differences between 0 and 4 kg in healthy and in symptomatic RC tears ( $p \leq 0.006$ ).

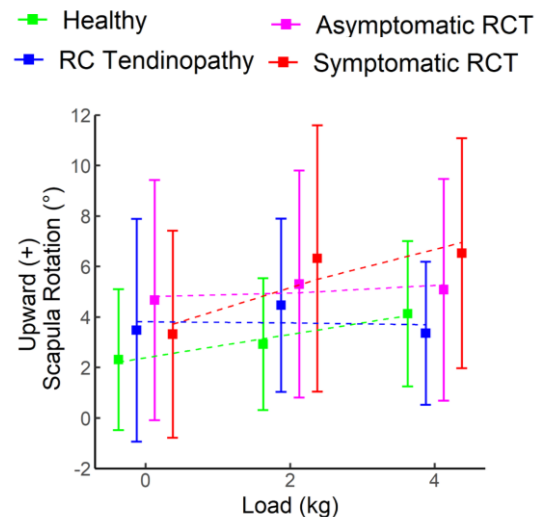


Figure 1: Mean and standard deviation of the upward scapula rotations during 30° arm abduction for the different shoulder types and additional handheld weights. Dashed lines are the results from the linear mixed model. RC: rotator cuff; RCT: rotator cuff tears.

## Discussion

These results indicate that shoulder kinematics are load-dependent. Greater upward scapula rotations are present in rotator cuff tears and increase with increasing weight, suggesting that scapular rotation is involved in the compensatory mechanisms after rotator cuff tears. Further analyses of load-dependent joint stability are needed to obtain a better understanding of shoulder kinematics in more demanding tasks.

## References

1. Yamaguchi et al, J. Shoulder Elb Surg, 9:6-11, 2000.
2. Croci et al, Eur Radiol 2023. *In press*.

## Acknowledgements

This work was funded by the Swiss National Science Foundation (SNSF #189082).



# CRITICAL SHOULDER ANGLE AND GLENOHUMERAL BIOMECHANICS IN SHOULDERS WITH ROTATOR CUFF TEARS – AN IN SITU STUDY

Jeremy Genter\* (1,2,3), Eleonora Croci (2,3), Andreas M. Müller (3), Annegret Mündermann (2,3,4), Daniel Baumgartner (1)

1. IMES, ZHAW, Winterthur 2. DBE, University of Basel, Basel 3. Department of Orthopaedics and Traumatology, University Hospital of Basel, Basel 4. Department of Clinical Research, University Hospital of Basel, Basel

\*Corresponding author: jeremy.genter@zhaw.ch

## Introduction

Glenohumeral biomechanics after rotator cuff tears are not fully understood. Clinical measurements of anatomical morphologies such as the critical shoulder angle (CSA) is often used as a predictor of rotator cuff tears. Nyffeler et al [1] showed that a lateralized acromion, which affects the CSA, directs the deltoid line of action more superiorly. However, the effect of the CSA on joint biomechanics (e.g., glenohumeral translation, center of pressure (CoP), joint reaction force (JRF), and shoulder muscle forces) in shoulders with rotator cuff tears under different weight-bearing conditions is not fully understood. The purpose of this study is to determine the effect of CSA on joint biomechanics using a glenohumeral simulator.

## Material and Methods

A glenohumeral simulator [2] with muscle-mimicking cable systems was used to simulate 30° abduction in the scapular plane. An artificial humerus (Sawbones, USA) and five specimen-specific scapular anthropometries were used to test six types of rotator cuff tears, two weight-bearing loads, and the native and adjusted (to different critical shoulder angles (CSAs)) deltoid origin sites. Linear mixed-effects models (CSA, RC tear type, and weight-bearing) with random effects (specimen and sex) were used to assess differences in GH biomechanics.

## Results

Glenohumeral translation increased from -1.1 mm to 3.2 mm as CSA increased from 28° to 45°, while JRF decreased by 1% per 1° increase in CSA and CoP position was slightly inferior with increasing CSA (Fig. 1). Rotator cuff tears did not significantly alter glenohumeral translations but shifted the CoP up to 5.3 mm more superiorly throughout motion. Weight-bearing significantly increased glenohumeral translation by 0.9 mm and JRF by 74% per 1 kg of additional weight. Rotator cuff and deltoid forces increased by a maximum of 196% and 50%, respectively, in the presence of rotator cuff tears, and weight-bearing increased rotator cuff and deltoid forces by a maximum of 23% and 78% per 1 kg of additional weight, respectively.

## Discussion

Increasing CSA increased glenohumeral translation and decreased JRF, which may make shoulders

with rotator cuff tears more prone to subluxation. However, rotator cuff tears were not associated with increased glenohumeral translation, as the teres minor and the inferior part of the subscapularis muscle compensated for the infraspinatus tear and superior subscapularis tear, respectively, and thus glenohumeral translation remained comparable to the intact rotator cuff. However, the CoP position shifted superiorly, close to where glenoid erosion occurs in patients with RC tears with secondary osteoarthritis [3]. These findings underscore the importance of early detection, precise management, and targeted rehabilitation strategies for RC tears.

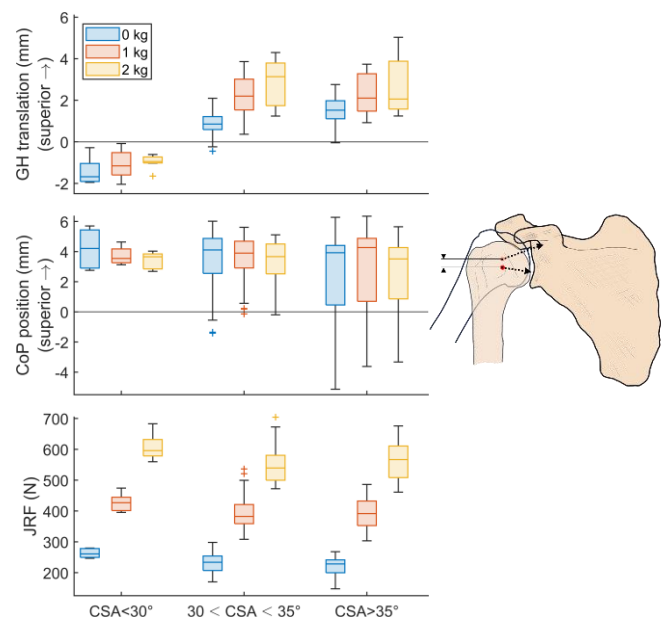


Figure 1: Boxplots of glenohumeral (GH) superior translation from 0° to 30° abduction, center of pressure (CoP) superior translation, and joint reaction forces (JRF) grouped by small, healthy, and large critical shoulder angle (CSA) only for visualization purposes, and weight-bearing loads (0 kg, 1 kg and 2 kg).

## References

1. Nyffeler et al., J Bone Joint Surg Am, 88(4):800–5, 2006
2. Genter et al., at-automatisierungstechnik, in press, 2023
3. Ozel et al., BMC Musculoskelet. Disord. 21, 668, 2020

## Acknowledgements

We thank Dr Brigitta Gahl for her help in the statistical analysis. This project is funded by the Swiss National Science Foundation (SNF 189082).





# KNEE BIOMECHANICS AND MUSCLE ACTIVITY AFTER ANTERIOR CRUCIATE LIGAMENT REPAIR AND RECONSTRUCTION

Linda Bühl\* (1,2), Sebastian Müller(1,2), Corina Nüesch(1,2), Annegret Mündermann(1,2), Christian Egloff (1,2)

1. Department of Orthopaedics and Traumatology, University Hospital Basel, Switzerland; 2. Department of Biomedical Engineering, University of Basel, Switzerland

\*Corresponding author: linda.buehl@unibas.ch

## Introduction

While clinical and patient outcomes after anterior cruciate ligament repair with InternalBrace™ augmentation (ACL-IB) and after ACL reconstruction (ACL-R) are comparable [1], no results on biomechanical function of the knee joint after ACL-IB and no comparison between the groups are available so far. We investigated whether differences during walking exist in knee biomechanics and muscle activity within ACL-IB, and compared to ACL-R and healthy subjects.

## Material and Methods

29 adult patients 2 years after unilateral ACL-IB (sex 13m; age  $36.8 \pm 10.6$  years; body mass index  $24.7 \pm 3.5 \text{ kg/m}^2$ ;  $25 \pm 3$  months postoperatively), 27 age- and sex-matched patients 2 years after ACL-R with autologous hamstring tendon (13m;  $37.0 \pm 10.7$  years;  $25.0 \pm 4.0 \text{ kg/m}^2$ ;  $24 \pm 2$  months postoperatively) and 29 healthy individuals (13m;  $37.0 \pm 10.7$  years;  $23.4 \pm 4.0 \text{ kg/m}^2$ ) completed an instrumented gait analysis. Kinematics, kinetics and muscle activity of Mm. semitendinosus, vastus medialis and lateralis, gastrocnemius, gluteus medius and tibialis anterior were collected using the Point Cluster Technique [2], Conventional Gait Model [3] and electromyography. Knee angle, moments, power, position of the tibia, and muscle activity (amplitude normalized to isokinetic maximum voluntary contraction (%MVC)) were temporally normalized to the gait cycle (%GC) and compared via statistical parametric mapping within ACL-IB (t-test) and between the operated of patients and non-dominant leg of controls (one-way ANOVA, posthoc t-test) ( $P=0.05$ ). Significant intervals  $>2\%$ GC were interpreted and mean of maximum difference (mDiff) in these intervals calculated.

## Results

No leg asymmetries in biomechanics or muscle activity were present in ACL-IB, and no differences between the operated legs in ACL-IB and ACL-R were observed. Compared to controls, ACL-IB had a less anterior tibia position around foot strike (mDiff  $-8.9 \text{ mm}$   $98\text{--}100\%$ ,  $P=0.016$  and  $0\text{--}3\%$ GC,  $P=0.015$ ), and ACL-R had a lower internal rotation moment during terminal stance (mDiff  $-0.04 \text{ Nm/kg}$ ,  $34\text{--}41\%$ GC,  $P<0.001$ ). However, the respective other ACL group presented similar deviation in these parameters (Figure 1). In muscle activity a higher variability and magnitude of in

semitendinosus activation could be observed in ACL-R compared to controls (Figure 1).

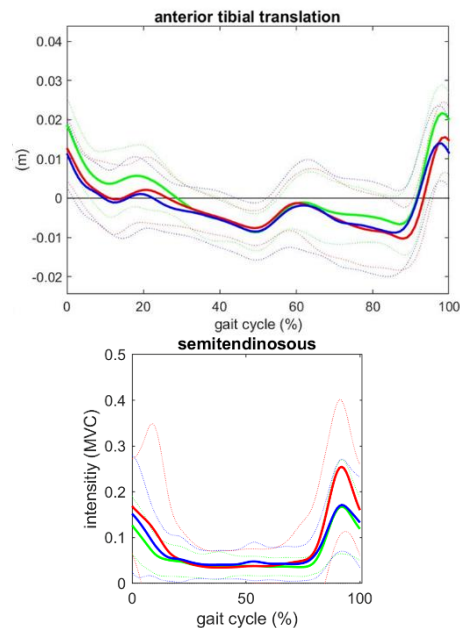


Figure 1: Mean (solid) and standard deviation (dashed) of anterior tibia translation (top) and semitendinosus muscle activity (bottom) of ACL-IB (blue), ACL-R (red) and controls (green) over gait cycle (%GC).

## Discussion

ACL-IB demonstrated no asymmetry 2 years after surgery. However, regardless of ACL surgery type, patients demonstrated altered knee gait mechanics in the operated knee, which might be due to initial ACL rupture. The absence of differences in muscle activity after ACL-IB compared with healthy subjects and the presence of differences after ACL-R underscores the importance of preserving the muscle-tendon complexes and the semitendinosus as an agonist of the injured ACL. Hence, our results strengthen the potential of augmented ACL repair as an alternative to ACL-R in proximal tears.

## References

1. Vermeijden et al. Knee, 38:19–29, 2022.
2. Andriacchi et al. J biomech Eng, 120:743–749, 1998.
3. Leboeuf et al. Gait Posture, 69:235–41, 2019.

## Acknowledgements

This study was funded from Deutsche Arthrose-Hilfe e.V., Swissorthopaedics and Freiwillige Akademische Gesellschaft Basel.



# INCLUDING TURBULENT STRESSES IN BLOOD DAMAGE MODELS: REYNOLDS-STRESS-BASED VS. DISSIPATION-BASED APPROACHES

Jonas Abeken (1), Diane de Zélicourt\* (1), Vartan Kurtcuoglu (1)

1. The Interface Group, Institute of Physiology, University of Zurich, Switzerland

\*Corresponding author: diane.dezelicourt@physiol.uzh.ch

## Introduction

To keep computational cost at bay, computational fluid dynamic simulations of hemodynamics in medical devices generally rely on unsteady Reynolds averaged Navier Stokes (uRANS) models. For the subsequent prediction of blood damage, which is influenced by turbulence stresses that are not resolved in uRANS, a suitable stress formulation that represents the modeled scales is required. However, a consensus on the best approach is still lacking.

Here, we compare two commonly employed stress formulations: a scalar stress representation [1] that employs Reynolds stresses as a proxy for unresolved fluid stresses, and an effective stress formulation based on energy dissipation that includes the modeled stress through the turbulent dissipation rate [2,3]. Comparing three different uRANS closure models and a large eddy simulation (LES) used as reference, we further investigate how the underlying turbulence model influences the results.

## Material and Methods

We conducted uRANS simulations of the CentriMag blood pump (Thoratec Switzerland GmbH [part of Abbott], Zurich, Switzerland) with three different closure models: the  $k-\omega$  shear-stress-transport ( $k-\omega$  SST) model, the elliptic blending  $k-\epsilon$  model ( $k-\epsilon$  EB) and the Reynolds Stress Transport model (RST) model. We further performed an LES to serve as reference.

We implemented both Reynolds-stress-based (RB) and dissipation-based (DB) stress representations in all models and compared the resulting total stress distributions in Eulerian and Lagrangian frameworks.

## Results

The hemodynamic fields of all uRANS models agreed well with the LES data, with time-averaged pressure head, flow rate and rotor moment within 3% of the LES for all models.

In the LES, both Reynolds-stress- and dissipation-based stress formulations led to similar stress distributions, albeit with slightly higher RB stress magnitudes (Figure 1). In the uRANS, however, the Reynolds-stress-based approach overestimated the contribution of unresolved stresses, leading to a general overestimation of the stresses and differences with the reference LES and between closure models up to several orders of magnitude.

In contrast, the DB stress distribution in uRANS showed a closer agreement to the reference LES for all closure models. Predicted DB stress magnitudes deviated by about 50% from the LES, which was more accurate than only considering resolved stresses.

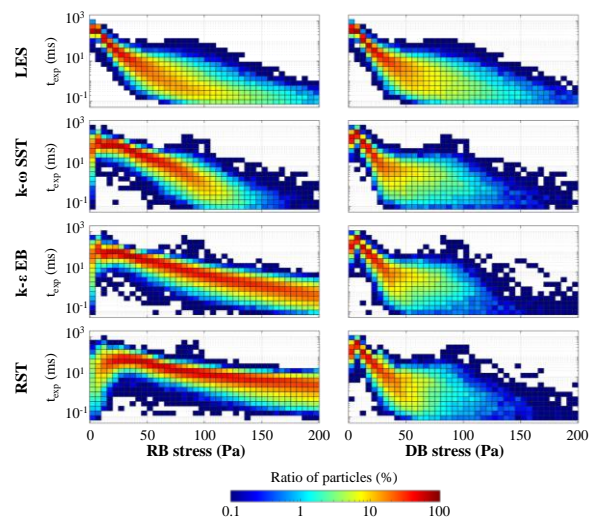


Figure 1: Heatmaps showing the ratio of particles experiencing a given stress magnitude for an exposure time  $t_{exp}$  during one passage through the pump, using either RB or DB stress formulations.

## Discussion

The Reynolds-stress-based formulation proved unreliable for estimating scalar stresses in our RANS simulations, while the dissipation-based approach provided an accuracy improvement over simply neglecting unresolved stresses. Our results suggest that dissipation-based inclusion of unresolved stresses should be the preferred choice for blood damage modeling in RANS.

## References

1. Faghih et al, Biomech Model Mechanobiol, 18(4):845-881, 2019.
2. Morshed et al, PLoS One, 9(8), 2014
3. Konnigk et al, Cardiovasc Eng Technol, 12(3):251-272, 2021.

## Acknowledgements

This work is part of the Zurich Heart project under the umbrella of "Hochschulmedizin Zürich" and is supported by the Stavros Niarchos Foundation (SNF). It was also supported by the Hartmann Müller Foundation under project number 2508



# COMPARATIVE ANALYSIS OF PRK, SMILE, AND LASIK FOR PERSONALIZED REFRACTIVE INTERVENTIONS

Malavika H. Nambiar (1), Sebastian Senti (1), Matteo Frigelli (1), Miguel Angel Ariza Gracia (1), Harald Studer (2), Abhijit Sinha Roy (3), and Philippe Büchler (1)

1. ARTORG Center for Biomedical Engineering Research, University of Bern, Switzerland;

2. Optimo Medical AG, Switzerland. 3. Narayana Nethralaya Eye Clinic, India

\*Corresponding author: philippe.buechler@unibe.ch

## Introduction

The global prevalence of myopia has experienced a significant increase over the past decades, with projections indicating that nearly half of the world's population will be affected by 2050. This alarming rise in myopia, including a substantial proportion of highly myopic cases, poses a significant risk of severe vision impairment and blindness. Consequently, there is a growing interest in refractive interventions such as PRK, LASIK and SMILE/CLEAR. Surgical planning for these interventions often aim for an under-correction due to anticipated myopic regression. It is generally accepted to have a residual refractive error of  $\pm 0.5$  D to accommodate these factors. However, recent long-term studies have shown that a significant percentage of cases fall outside this intended range. To enhance the personalization and predictability of refractive surgeries, *in silico* modeling such as finite element modeling, offer a valuable platform. In this study, we present a numerical model that incorporates the patient-specific geometry of the cornea, a depth-varying material model capturing the ultrastructural morphology of the cornea. Additionally, we analyze the model using post-operative data and compare the effects of PRK, LASIK, and SMILE surgeries.

## Material and Methods

Patient-specific geometric models were developed based on Pentacam elevation maps of patients who underwent PRK, LASIK, or SMILE at the Nethralaya Eye Clinic, India. Individual corneal morphology and surgical parameters such as the ablation profile, LASIK flap, or SMILE depth have been automatically reconstructed using GMSH 4.6 library in conjunction with Python 3.0. Since the surgical incisions are performed on the cornea under physiological stress due to the intraocular pressure, the corneal stress-free shape was determined by performing an iterative prestressing under IOP. A Holzapfel-Gasser-Ogden hyperelastic mechanical model was implemented using an ABAQUS UMAT subroutine [1]. The collagen fibers of the cornea were modelled according to x-ray scattering data. In addition to the fiber orientation, in-plane and out-of-plane fiber dispersions have been considered based on the ultrastructure of the cornea. The mechanical strength of the cornea was modelled to be linearly decreasing with corneal depth based on uniaxial tensile data obtained on strips from human donor. The model was validated by measuring the corneal curvature from the

clinical data and ensuring that it was accurately reproduced at each step of the modelling procedure.

## Results

As expected, the interventions significantly alter the corneal curvature (Fig. 1). The SMILE and PRK surgeries result in similar curvature maps. However, the curvature map predicted for LASIK is different because the flap retracts after removal of the underlying stroma, resulting in an underestimation of the correction by the model.

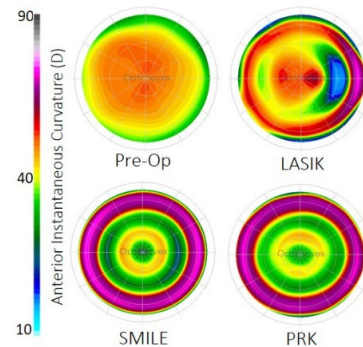


Figure 1: Curvature maps for the presurgical and post-surgical intervention of a typical patient.

## Discussion

The pre-surgical models are in good agreement with the patient's corneal geometry and topography (Fig. 2). Improvements are needed to accurately analyze LASIK interventions. Further analysis of the corneal stresses and strains will be performed for biomechanical analysis of the three refractive interventions in a cohort of 30 patients.

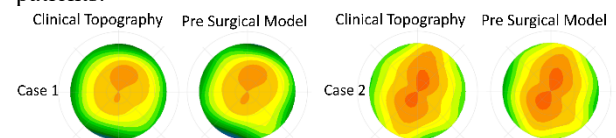


Figure 2: Curvature maps for the clinical data and presurgical model represented for two patients.

## References

1. Holzapfel G.A. et al, J Elasticity, vol. 61, pp.1–48, 2000.

## Acknowledgements

This work was supported by grant IZLIZ3\_182975 from the SNSF.





# DESIGNING 3D-PRINTED IMPLANTS USING TOPOLOGY OPTIMIZATION

Michaela Maintz (1,2,3,\*), Daniel Seiler (1), Florian M. Thieringer (2,3,†), Michael de Wild (1,†)

1. University of Applied Sciences and Arts Northwestern Switzerland FHNW, School of Life Sciences HLS, Institute for Medical Engineering and Medical Informatics IM<sup>2</sup>, Muttenz, Switzerland;

2. Department of Oral and Cranio-Maxillofacial Surgery, University Hospital Basel, Basel, Switzerland;

3. Medical Additive Manufacturing Research Group (Swiss MAM), Department of Biomedical Engineering, University of Basel, Allschwil, Switzerland

\*Corresponding author: [michaela.maintz@fhnw.ch](mailto:michaela.maintz@fhnw.ch)

†These authors have contributed equally to this work and share the last authorship.

## Introduction

Among facial bones, the lower jaw is often affected by fractures [1], which in many cases requires the fixation with an implant. Through developments in 3D-printing and virtual surgical planning technologies, the field of bone regeneration and repair is undergoing a revolutionary transition. For example, implants can be 3D-printed to suit the specific biomechanical and aesthetical needs of the patient which is especially beneficial in complex cases that require a high degree of customization. However, the manual design process of patient-specific implants remains arduous and often neglects crucial patient-specific biomechanical requirements, compromising strength and durability. To address this problem, Finite Element (FE) analysis, a computational modeling tool, can be used to simulate implant-bone models subjected to biomechanical forces, essentially, creating a “digital twin” of both the patient’s anatomy and implant to test the primary implant stability [2]. We are developing a method to design, verify and manufacture patient-specific topology-optimized (TO) osteosynthesis plates, which can be used to stabilize fractures of the mandibular angle [3]. Particularly, the stability of the implant subjected to biomechanical masticatory loads is investigated.

## Material and Methods

The mandible model was obtained from computed tomography data of a 19-year-old female patient. Multiple load conditions were static-mechanically simulated using Ansys Mechanical 2021 R1 (Ansys Inc, Canonsburg, United States) by FE analysis, which involved incisal, full, right molar, and left molar jaw clenching. The optimization objective was set to minimize the mass of the titanium implant while retaining the required mechanical stability. Various different screw configurations and implant thicknesses were tested. To evaluate the static-mechanical stability of the osteosynthesis plate, the FE simulation was conducted by applying four individual static masticatory load-cases used in the optimization process.

## Results and Discussion

Examples of generated implants are depicted in Fig. 1. The design space was reduced to approximately 12-15% of the total initial mass. The FE study revealed that the

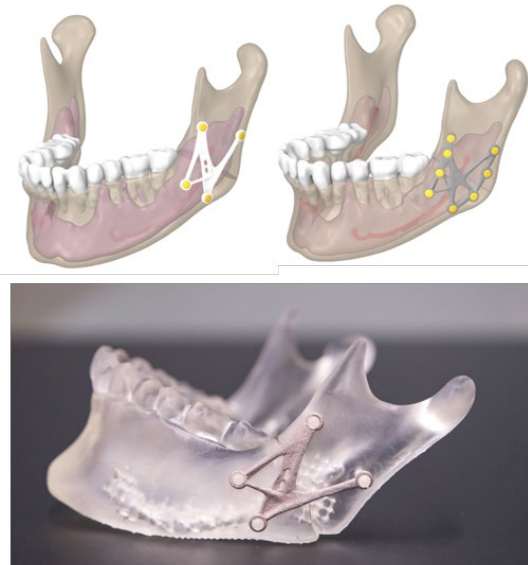


Figure 1: Topology-optimized patient-specific titanium plates for mandibular fracture osteosynthesis

von Mises Stresses of the implant and screws remained within the yield stress of the additive manufactured titanium, indicating mechanical resistance against the major masticatory forces present in the jaw. Biomechanical testing of the implants will be performed to verify these results.

## Discussion

In the virtual surgical planning at the point-of care, the surgeons can be directly involved in the design process. Additionally, the financial and inventory burden of the hospital will be relieved by the in-house additive implant manufacturing since thousands of unused stock implants must not be bought and stored. The digital FE validation of topology optimized implants could significantly speed up the process to bring effective osteosynthesis solutions to patients with time-critical traumatic injuries.

## References

1. Motamedi, M.H.K., Journal of Oral and Maxillofacial Surgery, 61(1): p. 61-64, 2003.
2. Maintz, M., et al., Journal of the Mechanical Behavior of Biomedical Materials, 144: p. 105948, 2023.
3. Maintz, M., et al., Current Directions in Biomedical Engineering, 8(2): p. 177-180, 2022.





# DEVELOPMENT OF A NOVEL BIOREACTOR FOR THE MECHANOBIOLOGICAL STUDY OF THE TENDON-BONE INTERFACE

Slavko Corluka\* (1, 2), Andreas S. Croft (1), Manuel Garnier (1), Sebastian Wangler (2), Helen Moser (2), Michael Künzler (2), Benjamin Gantenbein (1, 2), Michael Schär (2)

1. Department of Biomedical Research, University of Bern, Switzerland, 2. Inselspital Bern, University of Bern, Switzerland

\*Corresponding author: slavko.corluka@insel.ch

## Introduction

Tendons are crucial in transmitting mechanical force from muscles to bones. However, this task is challenging due to the significant difference in tissue resistance between the elastic tendon and the stiff bone. Consequently, stress concentrations occur at the interface between the tendon and bone, known as the enthesis.

The enthesis possesses a specialized structure comprising four zones with increasing calcification of the extracellular matrix from the tendon to the bone. [1] Excessive loading of the enthesis can lead to degeneration, resulting in the loss of the four-zone structure, tendon rupture, and the need for surgical refixation. Unfortunately, the current surgical refixation techniques have a high re-rupture rate, primarily due to the formation of scar tissue instead of the original four-zone structure during healing. [2]

To address this issue and reduce re-rupture rates, it is essential to understand the healing process of the enthesis after tendon refixation, particularly the role of mechanical loading.

Therefore, we aimed to develop an innovative bioreactor capable of precise mechanical loading in ex-vivo models, surpassing existing devices. In this study, we present the development of our new bioreactor and report our initial tests on entheses obtained from freshly slaughtered sheep using this state-of-the-art device.

## Material and Methods

The bioreactor consisted of a linear stage (Igus, Köln, Germany), a step motor (NEMA 24, Igus, Köln, Germany), a load cell (Pushon, Zhengzhou, China), and an Arduino microcontroller (Mega 2560, Arduino). The linear stage provided precise positioning control, driven by the step motor. The Arduino microcontroller programmed the bioreactor's functions, controlling motion, speed, direction, and force application using the load cell. It included a safety mechanism to prevent motor damage in case of resistance or sample rupture.

Sheep enthesis samples from a local abattoir were harvested and securely fastened inside a stainless-steel chamber using custom-made clamps. The chamber was sealed with a plastic beaker containing 5% fetal calf serum in high-glucose Dulbecco's Modified Eagle Medium (HG-DMEM). The fully assembled bioreactor was placed in a normoxic incubator at 37°C with 5% CO<sub>2</sub>.

Cultivation and mechanical loading of the sheep enthesis in the bioreactor were conducted for four days. On the fourth day, the cell viability of the mechanically loaded enthesis was assessed using the LIVE/DEAD Viability kit (ThermoFisher, MA, USA) and compared to a free-floating enthesis without mechanical loading.

## Results

We successfully developed a bioreactor capable of controlling ex vivo enthesis loading based on predefined strain or force values. The bioreactor's output includes force measurement within the range of 15 to 200 N, with an accuracy of  $\pm 10\%$  of the measured value and a repeatability of  $\pm 0.2$  N. The absolute position of the linear displacement demonstrates a precision of  $\pm 0.1$  mm, with a repeatability of  $\pm 0.05$  mm. All position, force, and time data are recorded for subsequent evaluation.

In our preliminary tests using cultivated entheses obtained from freshly slaughtered sheep, we observed a high initial cell viability of  $97.6\% \pm 0.044\%$  immediately after harvesting. However, by day 4 in the free-floating condition, the cell viability decreased to  $63.9\% \pm 0.073\%$ . In contrast, the mechanically stimulated sample exhibited a higher cell viability of  $74.4\% \pm 0.029\%$  on day 4, indicating a positive effect of mechanical loading on cell viability compared to the free-floating condition.

## Discussion

The newly developed bioreactor combines user-friendly operation, adaptability, and flexible sample loading, greatly expanding its range of applications. Initial test outcomes indicate a favorable effect of mechanical loading on cell viability in ex vivo bioreactor cultures of entheses extracted from freshly slaughtered sheep. To establish the validity of these observations, further assessment using larger sample sizes is imperative. Moreover, a comprehensive understanding of the exact implications of mechanical loading on enthesis requires diligent exploration of culture conditions and mechanical loading patterns.

## References

1. Loukopoulou et al, Eur Cell Mater. 2022 May 5;43:162-178.
2. Vinestock et al, Am J Pathol. 2022 Aug;192(8):1122-1135



# CONDITIONED MEDIUM FROM INTERVERTEBRAL DISC INHIBITS AUTOLOGOUS MESENCHYMAL STROMAL CELLS AND OSTEOBLASTS

Shuimu Chen\* (1), Andreas S. Croft (1), Sebastian Bigdon (2), Zhen Li (3), Andrea E. Oberli (1), Katherine B. Crump (1), Benjamin Gantenbein (1)

1. Tissue Engineering for Orthopaedics & Mechanobiology (TOM), Bone & Joint Program, Department for BioMedical Research (DBMR), Faculty of Medicine, University of Bern, Bern, Switzerland

2. Department of Orthopedic Surgery & Traumatology, Inselspital, University of Bern, Bern, Switzerland

3. AO Research Institute Davos, Davos, Switzerland

\*Corresponding author: shuimu.chen@unibe.ch

## Introduction

Low back pain (LBP) is a significant global burden and is associated with the degeneration of the spine and human intervertebral discs (hIVD) [1]. Current “gold standard” treatment for hIVD degeneration is the removal of the affected hIVD tissue and to promote spinal fusion. However, in some cases this process fail because of non-fusions after operation [2,3]. One possible reason is that bone morphogenetic protein (BMP) antagonists i.e., are secreted by the IVD at higher doses, which has a inhibitory effect of osteogenesis in the presence of IVD cells [4].

The purpose of this study is to explore the effect of conditioned medium (CM) from hIVD on autologous osteoblasts (hOBs) and bone marrow mesenchymal stem cells (hMSCs).

## Material and Methods

Collect the bone fragments, bone marrow and intervertebral disc from the same patients after spinal operation. Isolation of hOB, hMSC from bone and bone marrow, as well as three main cell types from hIVD, nucleus pulposus (hNP), annulus fibrosus (hAF) and cartilage endplate (hCEP). Make alginate beads with hIVDs and collect the conditioned medium. Conditioned medium is used to culture hOBs and hMSCs. Evaluate the osteogenesis of hOBs and hMSC, as well as potential cause.

## Results

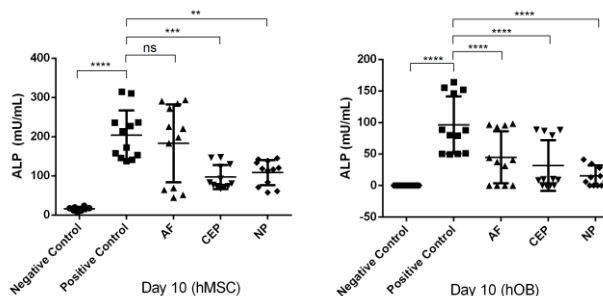


Figure 1. ALP expression significantly decreases on Day 10 when adding CM into hMSC and hOB. (*p*-value, \* < 0.05; \*\* < 0.01; \*\*\* < 0.001; \*\*\*\* < 0.0001; N=3-5)

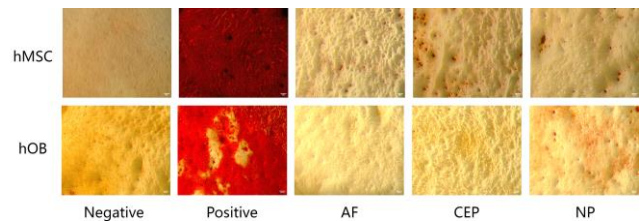


Figure 2. A trend of lower calcium deposition could be observed on Day 21 using alizarin red staining after hOB and hMSC cultured with CM from different hIVD cells. (Calcium deposits: Bright orange red; hMSC& hOB, N=3-5)

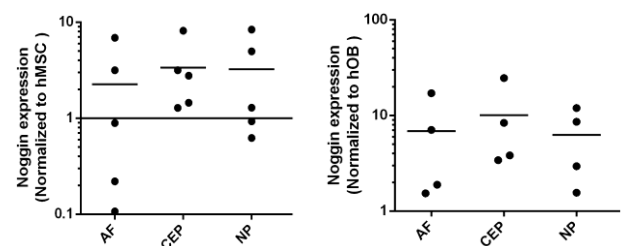


Figure 3. The expression of Noggin is mainly higher in all cell types of hIVD compared with hOB, as well as hMSC. (hMSC& hOB, shown are the means, N=3-5)

## Conclusions and Discussion

- Noggin is higher expressed in hIVD cells compared to hOB and hMSC (Fig 3).
- The osteogenesis of hOBs and hMSCs is generally inhibited in the presence of CM from hIVD cells.
- The high expression level of Noggin in hIVD cells may be a potential inhibitor of autologous OBs and MSCs.
- Knockdown of Noggin in hIVD cells could improve the osteogenesis of hOBs.

## References

1. James et al, The Lancet, 392(10159): 1789-1858, 2018.
2. Serra et al, Biofabrication, 8(3): 035001, 2016.
3. Watkins et al, Medicine, 93(29): e275, 2014.
4. Chan et al, Arthritis Research & Therapy, 18:29, 2016.



# IN-VITRO INVESTIGATION OF COMPRESSION AND CATABOLIC CYTOKINES ON HUMAN CARTILAGE ENDPLATE CELLS IN AGAROSE

Katherine B. Crump\* (1,2), Paola Bermudez-Lekerika (1,2), Ahmad Alminnawi (3,4), (1,2), Liesbet Geris (3,4), Jérôme Noailly (5), Benjamin Gantenbein (1,2)

1. Tissue Engineering for Orthopaedics and Mechanobiology, Bone & Joint Program, Department for BioMedical Research (DBMR), Medical Faculty, University of Bern, CH; 2. Department of Orthopedic Surgery & Traumatology, Inselspital, University of Bern, Bern, CH; 3. GIGA In Silico Medicine, University of Liège, BE; 4. Skeletal Biology and Engineering Research Center, KU Leuven, BE; 5. BCN MedTech, Universitat Pompeu Fabra, ES

\*Corresponding author: katherine.crump@unibe.ch

## Introduction

Intervertebral disc (IVD) degeneration is the main cause of low back cases in young adults [1]. However, the initiating and risk factors are poorly understood as it is a highly multifactorial disease. The cartilage endplate (CEP) covers the top and bottom of the IVD and acts to transmit compressive loads and transport water, nutrients, and waste in and out of the disc. [2] Early CEP degeneration is likely to play a key role in IVD degeneration, but little is known about CEP mechanobiology and its changes in degeneration. [3,4]. Investigating these changes is essential to elucidate how the CEP contributes to IVD pathology. It was hypothesized that CEP cells would behave similarly to articular chondrocytes. Thus, it was predicted that dynamic compression would be sufficient to induce anabolism, while stimulation with pro-inflammatory cytokines would induce catabolism.

## Material and Methods

Human CEP cells were expanded until passage 3 or 4, then seeded at a density of  $7.5 \times 10^6$  cells/ml into 2% agarose carriers (dimensions: 6 mm  $\varnothing$  and 3 mm height) and cultured for 5 days for phenotype recovery. Cell-agarose carriers were placed in custom-made chambers, stimulated with 10 ng/ml TNF throughout the entirety of the experiment and dynamically compressed under ~7% strain for one hour at 1.5 Hz daily for up to 14 days. Carriers were collected on Days 0, 7, and 14 for downstream analysis of cell viability, metabolism, gene expression, and glycosaminoglycan (GAG) content.

## Results

After 7 and 14 days of culture, cell-agarose carriers of the TNF-stimulated conditions showed decreased expression of anabolic gene aggrecan (*ACAN*) (Fig. 1), with no change in amount of collagen II (*COL2*). TNF-stimulated carriers showed a trend towards higher expression of catabolic genes matrix metalloproteinase 3 (*MMP3*) and *IL-6* compared to controls (Fig. 1). In contrast, there was a trend towards lower GAG/DNA content in TNF-stimulated carriers in comparison to controls. However, the GAG released in the media stayed consistent throughout the entirety of the experiment for all conditions. The TNF-stimulated

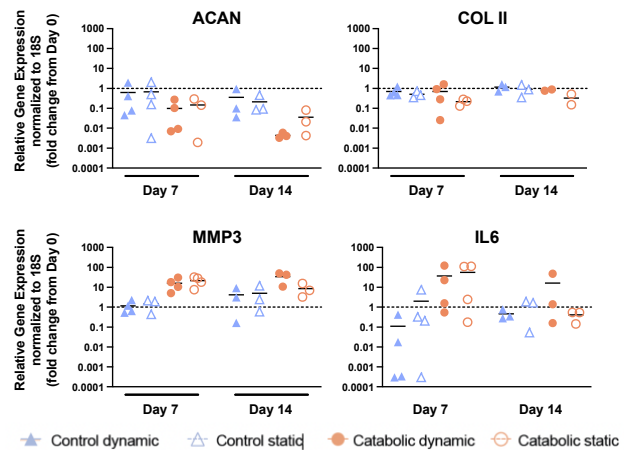


Figure 1: Relative gene expression of *ACAN*, *COL II*, *MMP3*, and *IL6* in CEP cells. Shown are the means,  $N=2-4$

carriers also showed a trend towards higher cell metabolic activity.

## Discussion

This study demonstrated that TNF could induce a catabolic response in human CEP cells through the downregulation of *ACAN* and the upregulation of *MMP3* and *IL6*. Interestingly, these results suggest TNF has a greater effect on *ACAN* than *COL2* within the CEP. Compression did not appear to effect gene expression or GAG content.

## References

1. P. Bermudez-Lekerika et al, Front Cell Dev Biol, 10:924692, 2022
2. Z. Sun et al, Int J Med Sci, 17(5):685-692, 2020
3. S. Roberts et al, Spine, 14(2):166-174, 1989
4. C. Ruiz Wills et al, Front Phys, 9:1210, 2018

## Acknowledgements

This project was supported by the Marie Skłodowska Curie International Training Network “disc4all” under the grant agreement #955735.



# EXPLORING A NOVEL SPHEROID 3D CELL CULTURE SYSTEM FOR TIE2+ NUCLEUS PULPOSUS CELLS OF THE INTERVERTEBRAL DISC

Silvan Rüttimann\*(1), Leon Schlagenhof (1), Andreas S. Croft (1), Andrea Oberli (1), Benjamin Gantenbein(1,2)

1. Tissue Engineering for Orthopaedics and Mechanobiology, Bone & Joint Program, Department for BioMedical Research (DBMR), University of Bern, CH

2. Department of Orthopaedic Surgery and Traumatology, Inselspital, Bern University Hospital, Medical Faculty, University of Bern, Bern, Switzerland

\*Corresponding author: silvan.ruettimann@unibe.ch

## Introduction

Low back pain (LBP) is a big problem in our aging society. LBP impacts the patients quality of life and places an immense burden on the healthcare system worldwide [1]. Degeneration of the intervertebral disc (IVD) is one of the common causes of LBP. Recently, nucleus pulposus (NP) progenitor cells (NPPC) were discovered, which are positive for Angiopoietin-1 receptor (aka. Tie2+/CD202b) [2-5]. These NPPCs are a promising cell source for IVD regeneration and may spark the development of novel cell therapies. It is known, that these NPPCs are pretty rare (2-10% of all IVD cells) in human IVDs and diminish in number with increasing age [6]. The low numbers of sorted primary NPPCs necessitates an expansion of the NPPCs. It has been demonstrated, that 3D culture is superior to classic 2D culture to maintain the pluripotent phenotype of the NPPCs [3]. The goal of this research is to test the expansion and culture of bovine NPPCs cells in a novel spheroid plate.

## Material and Methods

NP tissue was isolated from 5-6 discs from 4 bovine bovine tails (aged 10-13 months). NP cells were isolated by using a mild two step digestion protocol. Then, the primary NP cells were stained with Tie2 Antibody conjugated with Alexa 488 and DAPI for FACS. Sorted NP cells were expanded for 2 weeks under hypoxia (5% O<sub>2</sub>) and were supplemented with 2.5ng/ml FGF2 until 80% confluency. Tie2+ and Tie2- cells were then seeded in the functionalized and in the 2D control wells of the spheroid plate SP5D of Kugelmeier Ltd (see fig. 1). The cells were cultured for 2 weeks under hypoxia and FGF-2. Colony forming unit-assay was performed at day 0. Cell activity, DNA/GAG content and gene expression of selected genes was measured on day 1, 8, 15.

## Results

The DNA content of the Tie2+ and - spheroids (see fig. 2) increased by a factor of 1.7 and 3. The cells in the 2D plastic control wells grew faster and increased by factor of 11 and respectively 18.

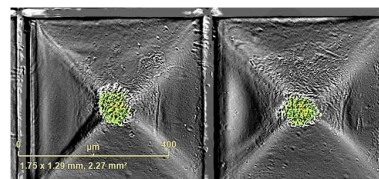


Figure 1: Spheroids of bovine NP Tie2+ cells stained with Calcein AM and Ethidium homodimer in the SP5D spheroid plate by Kugelmeier, 400 cells/microwell, 1d 6h after seeding

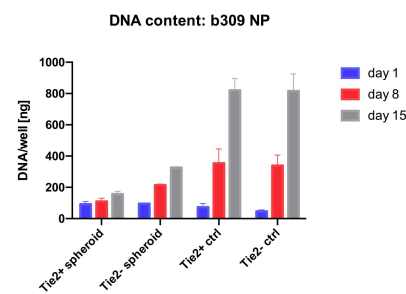


Figure 2: Absolut DNA content/well, either 750 spheroids or 2D control in 24well plate, Tie2 + and Tie2-, cultivated under hypoxia (2% O<sub>2</sub>) and supplemented with FGF2 (N=1, n=3), means ± SD

## Conclusion

The obtained results of the pilot show that sorted bovine NP cells proliferated in all culture conditions. There seems to be a big difference in the cell proliferation rate depending on the chosen culture system (3D vs 2D). However, more biological replicates are needed for further evaluation of the results.

## References

1. Spencer et al., Lancet 392:1789-858, 2018
2. Bischof et al., Applied Sciences 11: 7144, 2021
3. Guerrero et al., JOR SPINE 4:e1131, 2020.
4. Sako et al., Applied Sciences 11, 2021
5. Zhang, et al., Int. J. Mol. Sci 21: 9423, 2020
6. Sakai, et al., Nat Commun 3:1264, 2012

## Acknowledgements

This study is supported by an SNF Bridge – Discovery Grant (<https://data.snf.ch/grants/grant/211510>). FACSLab and Life cell imaging (LCI) of the DBMR, University of Bern are gratefully acknowledged.



Annual Meeting of the Swiss Society of Biomedical Engineering  
Department of Biomedical Engineering, University of Basel, Allschwil (Switzerland)  
September 13, 2023



# FROM NASAL CHONDROCYTES TO A 3D BIOPRINTED OSTEOCHONDRAL TISSUE

Esma B. Tankus<sup>\*</sup> (1), Gregor Miklosic (2), Valentina Basoli (1), Neha Sharma (1,4), Matteo D'Este (2), Andrea Barbero<sup>†</sup> (3), Florian M. Thieringer<sup>†</sup> (1,4)

1. Swiss Medical Additive Manufacturing, Department of Biomedical Engineering, University of Basel, Switzerland. 2. AO Research Institute Davos, Switzerland. 3. Cartilage Engineering Group, Department of Biomedicine, University Hospital of Basel, University of Basel, Switzerland. 4. Clinic of Oral and Cranio-Maxillofacial Surgery, University Hospital Basel, Switzerland.

<sup>†</sup>These authors have contributed equally to this work and share the last authorship.

\*Corresponding author: esma.tankus@unibas.ch

## Introduction

Osteochondral defects due to trauma or osteoarthritis affect the cartilage layer and the underlying subchondral bone. Cartilage tissue is divided into the articular and hypertrophic zones. Recent work has shown that the phenotype of chondrocytes within the different zones can be controlled by regulating oxygen concentration.<sup>1</sup> This study investigates the role of hypoxia in cartilage formation, using human nasal chondrocytes hNC embedded in a collagen/tyramine hyaluronic-acid-based (Col/THA) hydrogel<sup>2</sup>, by controlling oxygen gradient using a 3D bioprinting approach.

## Material and Methods

Primary hNCs were isolated from the nasal septum cartilage of patients (n=3) and were cultured in 2D under normoxic conditions (21%-O<sub>2</sub>), hypoxic conditions (2%-O<sub>2</sub>), or supplemented with hypoxia-inducing compound (21%-O<sub>2</sub>+1mM-DMOG). hNCs were embedded into the Col/THA (2.5%/15%) hydrogel with ruthenium/sodium persulfate (0.2 mM/2 mM) as a photoinitiator. Col/THA based constructs were generated using circular molds (Ø 5mm, height 1.5mm) and crosslinked using visible light for 10 min. Gene expression of chondrogenic and hypertrophic markers was performed by RT-PCR. New extracellular matrix deposition was assessed by using Alcian Blue (AB), safranin-O and immunofluorescence (IF) staining.

## Results

2D cultured hNCs in hypoxia and with DMOG maintained the native spheroidal morphology, showing positive AB staining. Conversely, the normoxic conditions showed an elongated fibroblastic morphology and a limited amount of AB-positivity (data not shown). Hypoxia-conditioned hNCs exhibited statistically significant upregulation of the chondrogenic markers and a lower expression of the hypertrophic cartilage markers (Fig. 1). Histologically, Col/THA-based constructs demonstrated new extracellular matrix formation, as evidenced by positive Safranin-O staining, which was further confirmed through positive immunofluorescence (IF) staining (Fig. 2).

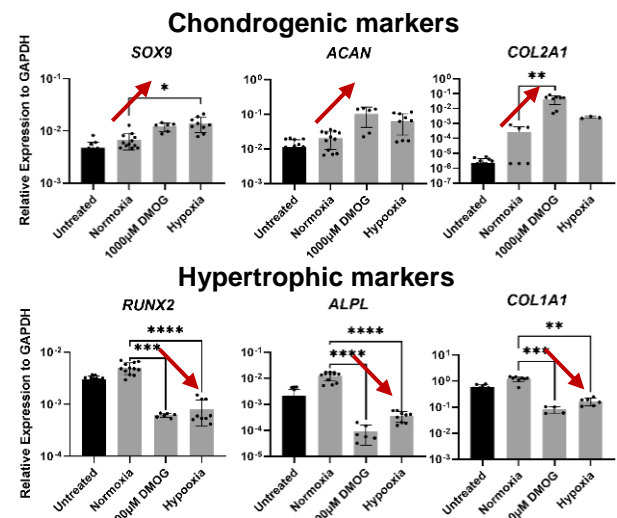


Figure 1: RT-PCR analysis of hNCs at day 14. Gene expression normalized to untreated samples. \* $p < 0.05$ , \*\* $p < 0.005$ , \*\*\* $p < 0.0005$ , \*\*\*\* $p < 0.0001$ .

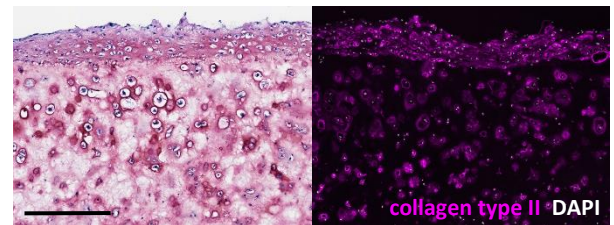


Figure 2: Safranin-O and IF staining of hydrogel construct cross-section (28 days). Scale bar: 200µm.

## Discussion

This project showcases the positive impact of hypoxic culture and the possible usage of a Col/THA-based hydrogel for cartilage formation, having implications for osteochondral repair. Moving forward, our next goal is to refine the strategy for generating a heterogeneous cartilage layer integrated with a subchondral bone scaffold, ultimately establishing a functional cartilage-bone interface.

## References

1. C-W. Twu et al, Allergy Rhinol, 5:125-131, 2014.
2. F. Staubli et al, Acta Biomater, 43:253-265, 2022.



# 3D-BIOPRINTING OF CARDIAC TISSUE MODELS WITH A NOVEL COST-EFFECTIVE AND VERSATILE BIOINK

Fabian Züger\* (1,2), Anna Marsano (3), Martino Poggio (4) and Maurizio R. Gullo (1)

1. University of Applied Sciences and Arts Northwestern Switzerland, Muttens, CH 4312, Switzerland

2 Swiss Nanoscience Institute University of Basel, Klingelbergstrasse 82, Basel, CH 4056, Switzerland

3 Cardiac Surgery and Engineering Department of Biomedicine University Hospital Basel, Switzerland

4 Nanomechanics and Nanomagnetism Department of Physics University of Basel, Switzerland

\*Corresponding author: fabian.zueger@fhnw.ch

## Introduction

In cardiac tissue engineering, the urge for novel biofabrication methods is high since myocardial infarction is one of the most common causes of hospitalization and death in the world. 3D-bioprinting for tissue regeneration relies on, among other things, hydrogels with favorable rheological properties. These include shear thinning for cell friendly extrusion, post-printing structural stability as well as physiologically relevant elastic moduli needed for optimal cell attachment, proliferation, differentiation, and tissue maturation [1]. This work introduces a novel cost-effective gelatin-methylcellulose based hydrogel whose rheological properties were optimized for ideal printability and cardiac tissue engineering [2] by means of neonatal rat cardiomyocytes and fibroblasts (NRCM, NRFB). The cells were mixed into the bioink and 3D-bioprinted into a distinct pattern. Long-term cell culture experiments (21d) were conducted, assessing cell viability, and beating behaviour at several timepoints.

## Material and Methods

The bioink, consisting of a blend of gelatine and methylcellulose (GMC) was freshly prepared, loaded with the cardiac cells (4mio/mL) and subsequently 3D-bioprinted (RegenHU Switzerland) into a predefined two-layered construct, with the following dimensions: a 18x18mm square, with 1mm spacing and a strand size of 300-400µm. A crosslinking solution composed of transglutaminase (TG, 120mg/mL) was poured over the construct and incubated for 5min. After this shape stabilization process the constructs were washed, submerged in full NRCM medium, and incubated for up to 21d (Fig. 1A). Every 48-72h the medium was changed and at several timepoints a life/dead assay using a Propidium Iodide (PI)/Hoechst staining was carried out. Staining was followed by fluorescence microscopy and ImageJ analysis of the cell viability at those different timepoints (Fig. 1 B&C). Beating construct areas were recorded and the beating deflection of cardiomyocytes was analyzed using Tracker software.

## Results

Cardiac cells were printed within the GMC bioink into a predefined two layered structure and could be kept for long time cell experiments in the incubator for up to 21d. During the whole timespan, the constructs kept their

original shape and a mean viability of 85.24% ( $\pm 1.62$ ) was measured. Along with this high viability, beating behaviour of the cells within the construct could be observed as well, over the period of the culture. These results indicate that a cell friendly 3D-printing process was established and that the GMC bioink is not cytotoxic. Furthermore, the porous structure helped for better nutritional exchange resulting in lower cell death, compared to areas with less porosity. Areas with beating NRCMs could be identified. Further details on methods and results will be presented at the meeting.

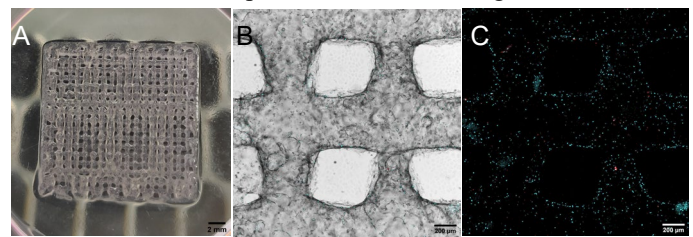


Figure 1: (A) Photograph of a 3D-bioprinted construct 21 days post printing and incubation at 37°C, bioink contains cardiac cells (4mio/mL), scale bar = 2 mm; (B&C) Fluorescence microscopy image of 21d post print construct stained with Hoechst 33342 (blue) and PI (red), stacking of brightfield (BF, only in B), Hoechst and PI channel, scale bar = 200 µm

## Discussion

These promising findings of cardiac cells being successfully mixed with bioink and 3D-bioprinted into a defined structure with a high viability and beating behaviour will support further experiments combining the structure with electrospun nanofibers (eNF) to create a cardiac tissue mimicking model. This combination can strengthen the electrical coupling and thus, enable proper cell maturation leading towards electrophysiological and structural relevant cardiac tissue models.

## References

1. Gopinathan, J. et al., Biomaterials Research 22, 11, 2018
2. Züger, F. et al., Biomimetics 8, 27, 2023

## Acknowledgements

The authors acknowledge financial support from the Swiss Nanoscience Institute (SNI) at the University of Basel.



Annual Meeting of the Swiss Society of Biomedical Engineering  
Department of Biomedical Engineering, University of Basel, Allschwil (Switzerland)  
September 13, 2023

# TEMPORAL INTERFERENCE STIMULATION OF THE PHRENIC NERVES

Elisa M. Kaufmann\* (1,3), Olivier Scheidegger (2), Andreas Häberlin (3), Thomas Niederhauser (1)

1. Institute of Human Centered Engineering HuCE, Bern University of Applied Sciences, Biel, Switzerland.;  
2. Department Neurology, Bern University Hospital, University of Bern, Bern, Switzerland 3. sitem Center for Translational Medicine and Biomedical Entrepreneurship, University of Bern, Bern, Switzerland;

\*Corresponding author: elisa.kaufmann@bfh.ch

## Introduction

Mechanical ventilation in the intensive care unit (ICU) can lead to complications such as ventilator-induced diaphragmatic dysfunction (VIDD), resulting in prolonged and cost expensive stays [1]. This study proposes a novel method using multiple esophageal electrodes for phrenic nerve stimulation (PNS) to address these limitations. Esophageal electrodes offer advantages such as selective stimulation and monitoring diaphragmatic electromyography [2]. Additionally, temporal interference stimulation (TIS) was introduced as a promising technique to overcome limitations of conventional stimulation [3], [4]. TIS utilized the low-pass filtering property of nerves and the low-frequency envelope of two interfering signals for stimulation. We hypothesize that selective phrenic nerve stimulation can efficiently activate the diaphragm with reduced co-stimulations.

## Material and Methods

**Multimodal Catheter Design:** A novel modular catheter design enables simultaneous measurements of diaphragm EMG, ECG, esophageal, and gastric pressure. Made of a flexible printed circuit board, the catheter comprises two main modules. The first segment integrates the stimulation electrodes for TIS, while the second combines different sensing modalities. This concept allows customization of the catheter length based on the weight and height of the pig or patient.

**TIS:** The finite element analysis study explores three electrode placement approaches: internal (esophageal), external (transcutaneous cervical), and mixed (esophageal and transcutaneous dipole). The aim is to assess their effects on stimulation outcomes. Control over interference location was achieved through current amplitude ratios and electrode placement. A sophisticated setup was used to analyze the impact of stimulation frequency, waveform, and electrode design on efficiency.

## Results

By manipulating electrode position, the maximum envelope locus could be rotated and displaced (Figure 1). Optimal centering was achieved by distributing electrodes in a trapezoidal shape along a circular circumference. When dipoles were close together, like in catheter arrangements, deep tissue stimulation range was limited, but maximum locus area remained centered. Changing electrode sizes (5mm<sup>2</sup> to 25mm<sup>2</sup>) had no significant effects. Precise locus

control within the body was achieved by varying dipole amplitudes without electrode movement.

## Discussion

Different electrode positions significantly impact external envelope steering, highlighting the importance of precise electrode placement and the challenge of internal application. However, variations in electrode size minimally affect external control. The study demonstrates the potential for non-invasive locus control without physical electrode movement, as supported by existing literature [3]. These findings will be validated in vitro using a multimodal esophageal catheter configuration and further confirmed in vivo.

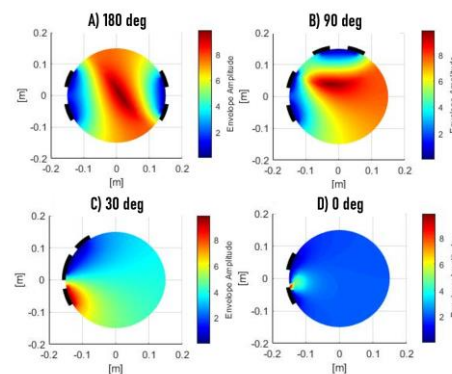


Figure 1: The circle depicts the cross-section of the neck region, black markers illustrating the positions of the electrodes. Electrode position impacts the envelope locus: A and B are external, while C and D represent possible esophageal dipole arrangements.

## References

1. Jaber, S. et al: Am J Respir Crit Care Med, 183(3):364-371, 2011.
2. Luo Y.M. et al, Am J Respir Crit Care Med., 160(5 Pt 1):1629-34, 1999.
3. Grossman N. et al, Cell, 169(6):1029-1041.e16, 2017.
4. Kaufmann E. et al, Biomed Eng Online., 30;22(1):5, 2023.





# ADAPTIVE ARTIFICIAL MUSCLES FOR TREATING INCONTINENCE

Beate Lyko\* (1), Hans Deyhle (1), Mirko Meboldt (2), Stephan Fox (2), Robert Katzschmann (3), Bert Müller (1)

1. Biomaterials Science Center, Dep. of Biomedical Eng., University of Basel, Switzerland,  
2. Product Development Group Zurich, Dep. of Mechanical and Process Eng., ETH Zürich, Switzerland,  
3. Soft Robotics Lab, Dep. of Mechanical and Process Eng., ETH Zürich, Switzerland

\*Corresponding author: beate.lyko@unibas.ch

## Introduction

Incontinence, the involuntary loss of urine, faeces, or gas, is a prevalent medical condition among the general population. Affected people can suffer from shame and social isolation [1], depression [2, 3], as well as physical pain [4]. Treatment often only includes the use of single use pads and transurethral catheters. Options for severe cases are limited. The current gold standard in implant-based therapy is the artificial sphincter AMS800™. It consists of three components including a fluid filled cuff with a fixed opening and closing pressure that must be set manually. However, with revision rates of up to 20% in the first five years due to material failure, tissue erosion and atrophy, this solution is unsatisfactory [5, 6]. An alternative device, as shown in Figure 1, based on hydraulically amplified self-healing electrostatic (HASEL) actuators that can automatically adapt the pressure on the urethra is needed. With a lowered average pressure and less implant components, atrophy and implant-associated infections will be reduced.

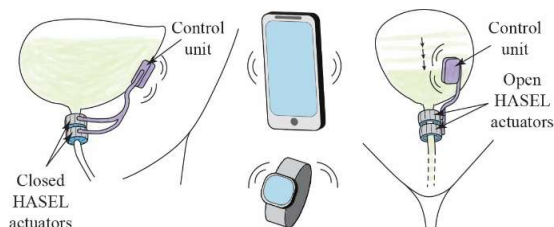


Figure 1: The alternative artificial urinary sphincter may consist of a single- or double-cuff placed around the urethra. Wireless communication permits additional functionality by medical experts and patients.

## Material and Methods

HASEL actuators, see Figure 2, are promising components for artificial sphincters.

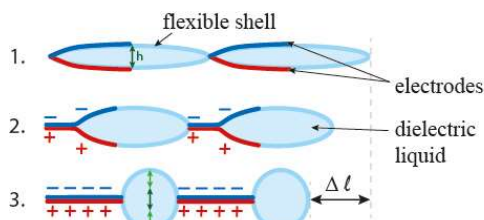


Figure 2: Scheme of cross section of a Peano-HASEL actuator with two units. Increase in voltage leads to closing of electrodes (1. → 3.) and thus to the deformation of the liquid-filled pouch [7].



Annual Meeting of the Swiss Society of Biomedical Engineering  
Department of Biomedical Engineering, University of Basel, Allschwil (Switzerland)  
September 13, 2023

The working principle is based on fluid-filled pouches with electrodes on two opposite sides. The pouches change their shape in length and width when a voltage is applied. They can be circularly arranged to mimic the human sphincter.

## Results

Figure 3 shows a possible HASEL sphincter design.

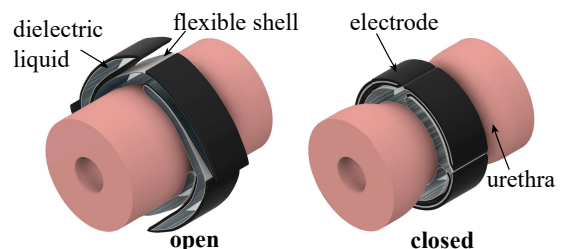


Figure 3: Schematic of a HASEL sphincter design: The flexible artificial muscle around the hollow organ is shown in the open state, where the urethra allows passing of water and closed state where a voltage is applied and the electrodes (black) attract, displacing the dielectric liquid inside the HASEL pouches. The actuator both increases in thickness and shortens.

## Discussion

Integrated self-sensing of actuators is envisaged for pressure adaptation within milliseconds. The control unit could be implemented either externally or directly onto the sphincter, which reduces the number of components in the system to just two or even one. The use of a double-cuff configuration, where the cuffs open and close alternately, could further reduce local tissue load while providing the required pressure of up to 100 cmH<sub>2</sub>O and a stroke of about 10 %. Through appropriate material selection and *in vitro* testing of the sphincter designs applying porcine urethras, a biocompatible and energy-efficient implant should be developed.

## References

1. Park et al, J Gerontol B Psychol Sci Soc Sci, 77 (7):1250-1258, 2022.
2. Cheng et al, J Int Med Res, 48(6):1-12, 2020.
3. Vrijens et al, Neurourol Urodyn, 36(7):1816-1823, 2017.
4. Beeckman, J Tissue Viability 26(1):47-56, 2017.
5. Srivastava et al, Eur Urol Focus 5(5):887-893, 2019.
6. Montague et al, Adv Urol 2012: 835290, 2012.
7. Kellaris et al, Sci Robot, 3:eaar3276, 2018.



# DYNAMIC COMPRESSION TESTS WITH SIMULTANEOUS ELECTROCHEMICAL ANALYSIS OF POUROUS GRADED TITANIUM

L. Graf\* (1), R. Meinke (2), P. Malgaroli (1), M. Maintz (1,3), C. Fleck (2), M. de Wild (1)

1. University of Applied Sciences Northwestern Switzerland, CH;

2. Technical University of Berlin, DE

3. Medical Additive Manufacturing Research Group, DBE, University of Basel, CH;

\*Corresponding author: lukas.graf@fhnw.ch

## Introduction

In this study a method to estimate the fatigue strength on porous graded titanium structures was established. The dynamic mechanical properties of implants with porosity gradients are important to determine the fatigue strength. However, dynamic compression tests of porous graded lattices have so far been largely undocumented. In this study, lattice structures featuring different porosity gradients have been developed, designed, and additively manufactured (AM) using selective laser melting (SLM). Subsequently, dynamic compression tests in a simulated biological environment with simultaneous electrochemical analysis have been performed to estimate the fatigue strength and corrosion resistance.

## Material and Methods

A sample used to verify the method is shown in Figure 1. It has been manufactured out of commercially pure titanium Grade 2 on a Realizer SLM-250<sup>HT</sup> system.

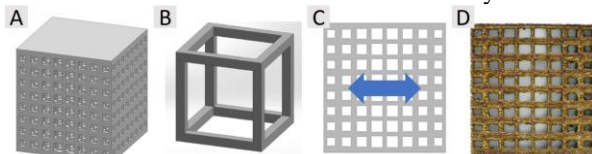


Figure 1: (A) Cubic sample with an overall side length of 11 mm covered on the top and bottom with a 0.3 mm thick plate. (B) Cubic unit cells. (C) A one-dimensional, mirrored porosity gradient ranging from 50% porosity in the 1<sup>st</sup> to 60% (2<sup>nd</sup>), 70% (3<sup>rd</sup>) and 80% (4<sup>th</sup>) column (f.l.t.r). (D) Frontal view of the sample.

The setup for the dynamic compression test with simultaneous electrochemical analysis is displayed in Figure 2. Hanks' BSS is used as the electrolyte and is kept at 37°C. The free corrosion potential is measured between the sample (working electrode) and the reference electrode (Argenthal Ag/AgCl, +207 mV to NHE). The free corrosion current is measured between the sample (working electrode) and the counter electrode, consisting of AM commercially pure Grade 2 titanium. The setup is comparable to Leinenbach, et al [1]. The specimens are mechanically loaded with a sinusoidal compression of 5 Hz. While the lower stress level is kept constant at -10 MPa, the initial upper stress of -60 MPa is constantly increased at a rate of 5 MPa/10'000 load cycles N (black lines in Figure 3). Throughout the entire experiment, the plastic strain amplitude is determined as the percentage of irreversible deformation (green line).

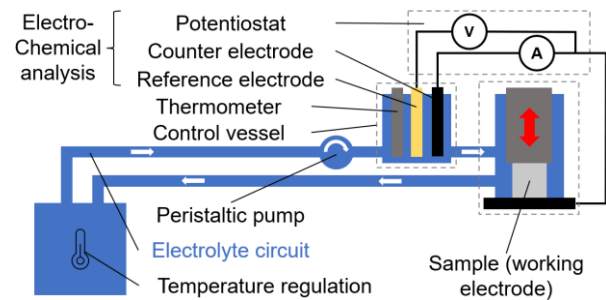


Figure 2: Setup for the dynamic compression tests with simultaneous electrochemical analysis.

## Results

The result of a typical dynamic compression test is displayed in Figure 3. The increasing compressive stress is shown in black. The test stopped at 106'890 load cycles with a maximum compression stress of -113 MPa. First structural failures are detected at 60k to 80k load cycles, indicated by peaks in the current flow (red), simultaneous abrupt drops of the potential (blue) under continuous exponential increase of the plastic deformation (green).

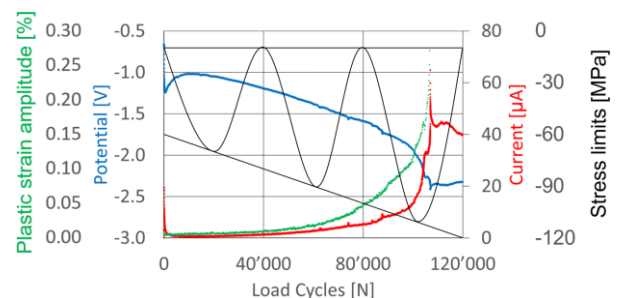


Figure 3: Results of potential (blue), current (red), and plastic deformation (green) during dynamic mechanical compression (black).

## Discussion

The study showed that initial mechanical failures are correlated to electrochemical degradation, presumably by fractures of the TiO<sub>2</sub> layer and their sudden reoxidation. The static mechanic failure load of the graded titanium scaffolds of -133 MPa is reduced to an estimated fatigue limit between -90 and -100 MPa.

## References

1. Leinenbach et al, Materials Science & Engineering Technology, 33:442-447, 2002.



# OPTIMIZATION OF HYDROTHERMAL TREATMENTS ON ORTHOPEDIC AZ31B ALLOY TO IMPROVE CORROSION RESISTANCE

Nadia Milanesi (1,2) \*, Matteo Pavarini (1), Monica Moscatelli (1), Roberto Chiesa (1)

1. Department of Chemistry, Materials and Chemical Engineering "G. Natta", Politecnico di Milano, Milan, IT

2. Department of Biomedical Engineering, Biomaterials Science Center, University of Basel, Basel, CH

\*nadia.milanesi@unibas.ch

## Introduction

Magnesium and its alloys have been recently recognized as promising absorbable materials for application in the biomedical field. The biocompatibility, nontoxicity and biodegradability of magnesium make it attractive for use in orthopedics, as it could help overcoming the need for secondary surgeries to remove temporary implants after bone healing. However, the main challenge for its application lies in balancing the degradation time of the implant and the healing time of the bone. In fact, the rapid corrosion of magnesium in physiological environments strongly limits its use and makes alloying and coating treatments essential. Among various surface modification solutions, the hydrothermal method represents a simple and inexpensive option to form thick hydroxide films on the surface of magnesium, which can protect the substrate by retarding the initial stages of corrosion [1]. Here, different one-step hydrothermal treatments are investigated to produce uniform, compact and protective films on AZ31B magnesium alloy.

## Material and Methods

The samples were first pretreated by acid etching and ultrasound cleaning. The hydrothermal treatment then was performed by immersing the samples in either water (ACQ) or different aqueous solutions, containing tricalcium phosphate (TCP), sodium bicarbonate and calcium nitrate (BDS-CNT), ammonium dihydrogen phosphate (DAP) or sodium nitrate (NAN), into Teflon-lined stainless steel reaction vessels with the samples, and heating them in a thermostatic oven for 4:30h at 160°C. The thickness of the formed coatings was then assessed by eddy current testing, while the coatings' morphology and structure were assessed by SEM imaging and microtomography.

Corrosion resistance was tested by potentiodynamic polarization (PDP) tests in simulated body fluid, and by *in vitro* degradation in phosphate-buffered saline (PBS) solution: the samples will be evaluated after 1-7-14 days of immersion by SEM and micro-CT. Further corrosion tests will also be performed with the EC-pen method [2]. Moreover, wettability measurements of the coatings will be performed by static water contact angle.

## Results

The PDP corrosion tests showed that the addition of elements in solution appears to inhibit the formation process of the protective layer on the surface of the

specimens, increasing the corrosion rate as compared to pure  $\text{Mg}(\text{OH})_2$  coatings. The corrosion rate is reported in Table 1, as well as the thickness of the coatings.

Table 1: Corrosion behavior and coating thickness of the hydrothermal coatings

Solution	Corrosion rate (mm/year)	Coating thickness ( $\mu\text{m}$ )
ACQ	$0.10 \cdot 10^{-2}$	$18.97 \pm 0.85$
TCP	$0.57 \cdot 10^{-2}$	$24.35 \pm 2.87$
BDS-CNT	$2.66 \cdot 10^{-2}$	$50.49 \pm 1.42$
DAP	$102 \cdot 10^{-2}$	$54.78 \pm 13.98$
NAN	$3.10 \cdot 10^{-2}$	$28.24 \pm 1.27$

By observing the SEM images, the differences in coating morphology and accumulations can be appreciated (Figure 1).

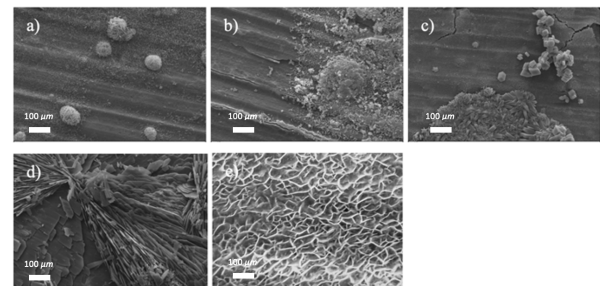


Figure 1: SEM micrographs of the different coatings: a) ACQ, b) TCP, c) BDS-CNT, d) DAP, e) NAN.

## Discussion

Although the ACQ specimens appear to have the best corrosion resistance, by integrating elements within the coating it could be possible to promote bone healing thanks to a modulation of the corrosion layer's composition. Further analyses will allow to investigate how the different solutions affect coating formation and  $\text{Mg}(\text{OH})_2$  nucleation and to better describe the corrosion behavior of each family of coatings.

## References

1. Y. Chen et al, Acta Biomater, 10:4561-4573, 2014.
2. F.M. Weiss. et al, Eur Cells Mater, 30, 2015.



# THERMAL ANALYSIS OF NEW TRANSDERMAL DEVICES FOR POWER TRANSFER TO VENTRICULAR ASSIST DEVICES

Christian Grossmann Aybar (1), Daniel Fehr\* (1), Fabrizio Spano (1), Andreas P. Kourouklis (2), Edoardo Mazza (2), Mathias Bonmarin (1)

1. ZHAW Zurich University of Applied Sciences, School of Engineering, Institute of Computational Physics, Technikumstrasse 9, 8400 Winterthur, Switzerland

2. Department of Mechanical and Process Engineering, Institute for Mechanical Systems, ETH Zurich, Leonhardstrasse 21, 8092, Zurich, Switzerland

\*Corresponding author: fehd@zhaw.ch

## Introduction

Different engineered approaches have led the design of implants with controlled physical features to minimize adverse effects in biological tissues. Aiming to prevent infection, similar efforts have focused on optimizing the design features of drivelines used to transfer power to percutaneous ventricular assist devices (VAD), omitting however a thorough look on the implant-skin interactions that govern local tissue reactions. Here, we utilized an integrated approach for the biophysical modification of transdermal implants and their evaluation by chronic sheep implantation in comparison to the standard of care VAD drivelines.

## Material and Methods

We developed a novel method for the transfer of breath topographical features on thin wires with modular size. Moreover, we examined the impact of implant's diameter, surface topography, and chemistry on macroscopic, histological, and physical markers of inflammation, fibrosis, and mechanical adhesion on 16 implants. Furthermore, we performed COMSOL simulations to investigate the electrothermal implications of conductive wires with different sizes for the power transfer to VADs. In our model, we simulate the electrical properties of the prototype's wires, to confirm that it does not produce a significant body temperature rise. The skin model (Fig. 1a) mimics the multilayered skin properties of the abdominal wall of epidermis, dermis, fat and muscle (3 cm thickness) [1]. Also, we include a PDMS layer (5 mm thickness) that represents the silicon-based material of the conductive skin.

## Results

All implants demonstrated infection-free performance. The fibrotic response was enhanced by the increasing diameter of implants but not influenced by their surface properties. The implants of 0.2 mm diameter promoted mild inflammatory responses with improved mechanical adhesion and restricted epidermal downgrowth, in both silicone and polyurethane coated transdermal wires. On the contrary, the VAD drivelines with larger diameter triggered severe inflammatory reactions with frequent epidermal downgrowth [2]. During the study, different thicknesses of the polyurethane (PU) insulating coating were tested for the

wire of 0.2 mm diameter. However, no significant improvement was observed when increasing the insulation layer, since the temperature difference in the model was due to the temperature skin gradient and not the electric current. In this model, the dimensions of both the inner copper diameter and the PU coating thickness were obtained from the manufacturer's specifications (0.2030 mm and 0.0105 mm, respectively).

Our results show that when the wires are subject to the peak voltage for VADs (~14.5 V) and a steady-state current of 1.2 A, the temperature temporarily increases by up to 0.65°C in the core of the copper wires (Fig. 1b), due to the inrush current. Nonetheless, the temperature of the patch in the steady state remains increased by around 0.02°C, indicating that there is no significant risk for skin injury from heat dissipation.

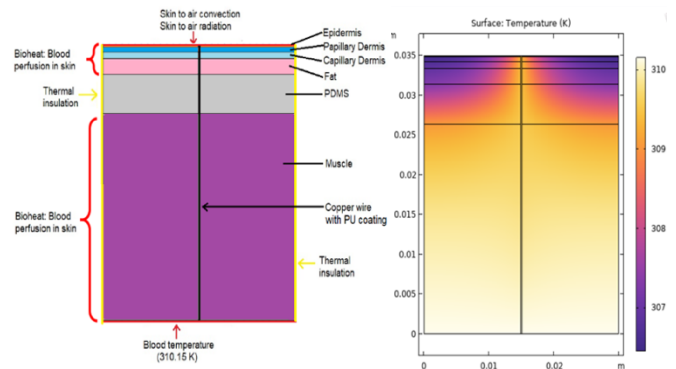


Figure 1: a) Schematic representation of the model and boundary conditions in COMSOL Multiphysics. b) Temperature distribution for a 1.2 A current.

## Discussion

This combination of experimental and computational findings will enable the design of new percutaneous medical devices to support therapies that require safe exchange of power, signal, and mass through the human body, without affecting the patient's electrothermal conditions.

## References

1. Bonmarin et al, Comput Biol Med, 47:36–43, 2014.
2. Kourouklis et al, Eur Biophys J, 51: 171–184, 2022.



# FEASIBILITY AND ACCURACY OF ROBOT GUIDED COLD ABLATION OSTEOTOMY FOR EXTRADURAL ANTERIOR CLINOIDECTOMY

Thanh Tu Ha\* (1), Martina Schicker (1), Yann Luder (1), Marta Morawska (2), Michel Roethlisberger(1)

1. University Hospital Basel, Switzerland; 2. Advanced Osteotomy Tools AG, Switzerland

\*Corresponding author: thanhthu.ha@stud.unibas.ch

## Introduction

Anterior clinoidectomy is a surgical procedure used to access the central skull base, providing access to sellar and parasellar pathologies and vascular lesions in and around the cavernous sinus.[1] However, the procedure is challenging and risky due to limited working space, restricted surgical view, and proximity to critical anatomical structures such as the carotid artery, sinus cavernous sinus, oculomotor nerve, and optic nerve. [2]

Different instruments for removal are mentioned in the literature. Mechanical removal with a diamond drill is the most common method. However, mechanical removal carries risks. Mechanical and thermal damage may occur due to the drill. Furthermore, the outcome is strongly dependent on the experience of the surgeon. [3]

Advancements in medical robotics technology offer potential improvements in various areas of neurosurgery. [4] The aim of our study was to test the feasibility and accuracy of the robotic Er:YAG laser for removal of the anterior clinoid. Potential improvements could be the absence of mechanical as well as reduced thermal damage to the surrounding tissue. [5] Furthermore, high precision can be achieved by robotic guidance.

## Material and Methods

The experiment utilized five fresh frozen skulls, fixed in a Mayfield clamp to ensure a stable setup. Preoperative planning was performed using NeuroPlan®, which segmented critical anatomical structures and planned trajectories with a safety distance of 2 mm from danger zones. A navigation system and additional referencing screws were employed for precise bone ablation.

The target structure was reached by performing a pterional craniotomy and extradural preparation of the anterior clinoid. Finally, precise bone ablation was performed with the Er:YAG laser attached to a robotic arm moving in 7 axes. A navigation system and an OCT laser ensured the required accuracy.

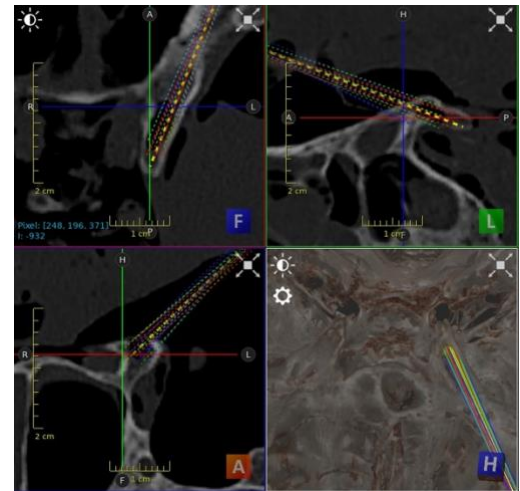


Figure 1: Trajectory planning on the preoperative CT scan. Overview in the axial, sagittal and coronary sectional planes. 3D reconstruction of the anterior clinoid with the trajectories.

## Preliminary Results

Table 1: The evaluation of the data is not yet complete. On average, 63% of the cancellous volume was removed from the anterior clinoid with the laser. The total volume of the anterior clinoid averaged 290 mm<sup>3</sup>.

Head (No.)	1	2	3	4	Mean
Width in the base (mm)	8.7	8.92	9.29	9.23	9.06
Length (mm)	9.8	10.1	11.8	12.0	10.9
Volume whole anterior clinoid (mm <sup>3</sup> )	194	180	391	396	290
Volume cancellous bone anterior clinoid (mm <sup>3</sup> )	134	86	204	192	152
Ablation volume (mm <sup>3</sup> )	92	78	108	103	96
Axially preserved corticall	No	Yes	Yes	Yes	-
Percent volume of ablation to volume of cancellous bone	69%	90%	53%	54%	63%
Number of laser pulses per laser trajectory	22	20	10	19	18

## References

1. Rhoton A. et al, Neurosurgery, 51:273-302, 2002.
2. Kulwin C. et al, Surg Neurol Int, 2:140, 2011.
3. Dongwoo J. et al, Neurosurgery, 64:96-105, 2009.
4. Singh R. et al, Surg Neurol Int, 19:13:373, 2022
5. Beak K.W. et al, Lasers Surg Med, 53(3):291-9, 2020





# FEASIBILITY AND ACCURACY OF ROBOT-GUIDED COLD ABLATION OSTEOTOMY FOR EXTRADURAL OPTIC CANAL UNROOFING

Martina Schicker\* (1), Thanh Tu Ha (1), Yann Luder (1), Dominik Cordier, (1) Marta Morawska (2) and Michel Röthlisberger (1)

1. Universitätsspital Basel, Petersgraben 4, Basel, Switzerland;

2. Advanced Osteotomy Tools AG, Basel, Switzerland;

\*Martina Schicker: e-mail: [martina.schicker@stud.unibas.ch](mailto:martina.schicker@stud.unibas.ch)

\*Thanh Tu Ha: e-mail: [thanhtu.ha@stud.unibas.ch](mailto:thanhtu.ha@stud.unibas.ch)

## Introduction

Optic canal unroofing is a surgical technique employed to reach the central skull base, allowing entry to sellar and parasellar pathologies as well as vascular lesions located within and around the cavernous sinus. [1]

In modern practice, a Diamond Drill is used to take out the roof's volume. Despite the procedure's relative safety in the hands of skilled surgeons, there is general agreement that conducting drilling in the anterior skull base is linked to considerable risks. [2,3]

Modern studies using YAG lasers have demonstrated that this technique can be very promising compared to mechanical tools. [4]

The objective of this study was to evaluate the feasibility and precision of utilizing a cold ablation roboter-guided laser osteotome for delineating the boundaries of the optical canal. Additionally, the investigation involved the insertion of a thermal probe into the optical canal to assess the occurrence of significant heat damage resulting from the removal of the optic roof. Success was defined as the accurate excavation of the optical canal, which was confirmed through post-experimental CT scans and photographic documentation.

## Material and Methods

The experiment utilized five fresh frozen skulls. Preoperatively, critical structures were segmented in the Neuroplan © software and given a safety margin of 2mm. Based on this, four trajectories were planned, which were connected to two lines. Accurate bone removal was accomplished using the Er:YAG laser, which was connected to a robotic arm capable of movement along seven axes. A navigation system and an OCT laser were employed to guarantee the necessary precision. The skulls were opened using a pterional craniotomy technique, and the procedure was conducted extradurally.

## Preliminary Results

The data evaluation is not yet fully concluded. However, immediately postoperatively, clearly visible markings can be observed macroscopically, which appear to be highly accurate in comparison with the preoperative planning. In the postoperative CT scans, the markings are not visible.

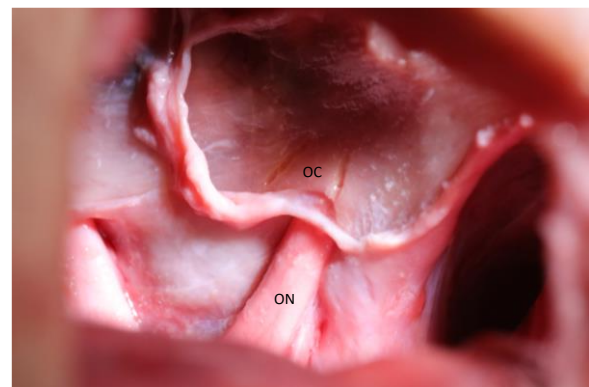


Figure 1: Markings of the optic canal with intact optic nerve, OC: Optic Canal, ON: Optic Nerve

## Discussion

These initial findings have the potential to stimulate further investigation into the applications of robotic and laser technologies in the realm of neurosurgery.

However, we have identified some limitations: Depth precision isn't as advanced as expected yet. Also, cadavers lack active bleeding, and temperature measurement limitations require more experimentation.

Overall, the study emphasizes the feasibility and exceptional precision of robotic technology, which can be utilized to advance the development of additional procedures to improve patient outcomes and reduce perioperative risks in neurosurgical interventions.

## References

1. Rhoton A. et al, Neurosurgery, 51:273-302, 2002.
2. Spektor, S. et al, Neurochir 155, 1017–1024 (2013).
3. Akabane, A. et al, Journal of Neurosurgery, 82(2), 284-287.
4. Baek KW. et al Lasers Surg Med. 2015 Jul;47(5):426-32.



# MODEL TO SIMULATE BRAIN BIOPSIES USING A NAVIGATED ROBOTIC GUIDING SYSTEM AND A BONE CUTTING LASER

Thanh Tu Ha (1), Yann Luder\* (1), Michel Röthlisberger (1), Martina Schicker (1), Marta Morawska (2), Dominik Cordier (1)

1. University Hospital Basel, Switzerland; 2. Advanced Osteotomy Tools AG, Switzerland

\*Corresponding author: yann.luder@stud.unibas.ch

## Introduction

Brain biopsies are necessary in cases of unclear lesions on imaging studies to establish a treatment plan based on the histologic diagnosis [1]. Conventional methods frequently include skin incisions of up to 4 centimeters in length and drilling a hole up to 14 millimeters in diameter and the angle of the biopsies are relatively limited to 90 degrees. Hence, there is interest in alternative methods that potentially improve the procedure. A previous study investigated the potential of an Er:YAG laser to make brain biopsies less invasive, faster, and safer. The study demonstrated that the Er:YAG laser can create highly precise bone channels for biopsies. Furthermore, it can create tangential bone channels which allows for biopsy of brain regions that are usually impossible or hazardous to access. [2]

Building upon the results of the previous study, further research and technological advancements were pursued. Consequently, the Er:YAG laser osteotome used in this study allows bone ablation and biopsy needle guidance without the need for attachment to the operating table or head immobilization device, as is the case with conventional methods for guiding the drill and biopsy needle.

## Material and Methods

In this study, five freshly frozen heads were used, which were immobilized using a Mayfield clamp. Before conducting the biopsies, the NeuroPlan© software was used to plan the trajectory and angle of the biopsies. To align the pre-experimental CT with the skull, referencing points on the skull and its surface are registered using a pointer. A small skin incision was made at the biopsy entry point marked by a targeting laser to access the bone area where the Er:YAG laser ablated the bone for the biopsy.



Figure 1: Head of the laser osteotome robot with attached biopsy needle guidance system and inserted biopsy needle.

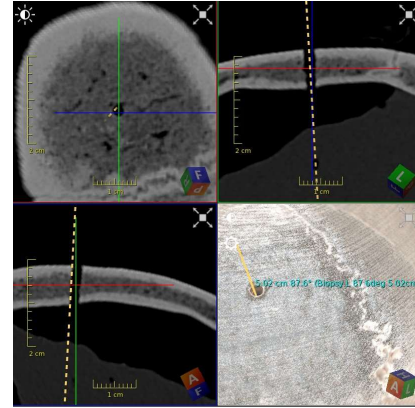


Figure 2: Biopsy accuracy is assessed using Neuroplan©, which overlays pre-biopsy CT scans with planned trajectories and post-biopsy CT scans.

## Results

Table 1: Preliminary results show that the laser osteotome can accurately remove bone along planned trajectories from pre-biopsy CT scans, with precision near the lower limit of the 1-3 mm accuracy range of conventional biopsy methods.

Variable	Biopsy angle (degrees)	Count	Mean (mm)	Min (mm)	Max (mm)
Bone channel diameter	45	5	2.80	2.51	3.20
	90	5	2.47	2.36	2.54
	total	10	2.64	2.36	3.20
Deviation from centre of bone channel	45	5	0.94	0.35	1.64
	90	5	1.18	0.66	2.08
	total	10	1.06	0.66	2.08

## Discussion

The laser osteotome enables precise bone ablation along previously planned trajectories, while the robotic arm ensures sufficient stability for guiding the biopsy needle. Furthermore, it allows biopsies at angles not possible with conventional methods, providing access to previously inaccessible brain regions. However, during the transition from bone ablation to biopsy, the sterile cover for the biopsy needle guidance system must be removed and reattached. Since the laser osteotome is currently slower than drilling, future optimization of the setup to avoid this transition could significantly speed up the procedure.

## References

1. Burger PC. et al, Arch. Path. Lab. ,121(5):477-480, 1997
2. Ha TT. et al, Front. Oncol., 11:690374, 2022.



# A ROBUST ELECTROMAGNETIC TRACKING SYSTEM FOR DEEP BRAIN STIMULATION SURGERY

Céline Vergne<sup>\*(1,2,3)</sup>, Morgan Madec (2), Raphael Guzman (4), Joris Pascal (1), and Simone Hemm (1)

1. *Institute for Medical Engineering and Medical Informatics, School of Life Sciences, University of Applied Sciences and Arts Northwestern Switzerland, Muttenz, Switzerland.*
2. *ICube laboratory, University of Strasbourg – CNRS, Strasbourg, France.*
3. *Department of Biomedical Engineering, Faculty of Medicine, University Basel, Allschwil, Switzerland.*
4. *Department of Neurosurgery, University Hospital Basel, Basel, Switzerland.*

\*Corresponding author: celine.vergne@fhnw.ch

## Introduction

The electromagnetic tracking (EMT) technique is an effective method for neuronavigation as it allows for real-time wireless guidance of tools without requiring a line of sight. However, EMT systems available on the market are not compatible with the standard procedure to guide the placement of deep brain stimulation (DBS) electrodes based on a stereotactic system [1]. This incompatibility is caused by the distortions induced by the stereotactic system in the tracking volume [2], which can lead to significant degradation of tracking performance [3]. Most distortions are the result of the alternating magnetic field of the EMT system itself. This alternating field is required to localize the sensing units, which are inductive sensors. To address this issue, we developed a new EMT system, ManaDBS, based on on-chip magnetometers capable of measuring the quasi-static magnetic fields applied for our tracking. In this work, we compare the tracking performance degradation of our system to the market device, NDI Aurora®, in the presence of a stereotactic system.

## Methods and materials

The two navigation systems, NDI Aurora® and ManaDBS, consist both of a magnetic field generator of 20 cm x 20 cm x 7 cm and a flexible tube of 1.4 mm diameter, functionalized with a sensor at the tip. The sensor was placed at 25 cm from the generator. The frame and arc of the Leksell® Vantage™ Stereotactic System and Leksell® Stereotactic G system were investigated. Each object was inserted between the generator and the sensor. The sensor's localization was carried out twice; initially without the object, and subsequently with the object placed at a distance ranging from 60 mm to 5 mm from the sensor. The position error was calculated as the Euclidean distance between the positions obtained without the object and with the object at varying distances. For the orientation, the Sum of Squared Errors (SSE) was also calculated as both systems have 6 degrees of freedom.

## Results

The NDI Aurora® exhibits errors (Euclidian distance) up to 0.4 mm, 2.5 mm, 5.8 mm, 5.9 mm for the Vantage frame, G-frame, Vantage arc, and G-arc respectively

(Fig. 1) with a mean error of 0.4 mm, 1.9 mm, 3.8 mm, 4.8 mm. The ManaDBS exhibits a maximal error of 0.4 mm and a mean error of 0.1 mm over all the different objects. The mean SSE for the orientation is 0.9° and 1.4° for the NDI Aurora® and the ManaDBS respectively over all the different objects.

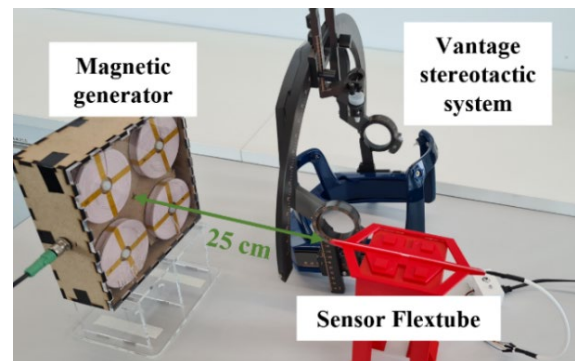


Figure 1. Picture of the experimental setup, the two navigation systems can be switched without changing the configuration, the flexible tube is placed at 25 cm from the magnetic field generator.

## Discussion

Metallic parts from the stereotactic system such as both arcs and the G-frame respectively induced a degradation in the performance of the NDI Aurora®. As the Vantage frame is made from resin that doesn't distort the magnetic field, both navigation systems exhibit unchanged performances. The ManaDBS shows robustness to the presence of the stereotactic system in the tracking volume in comparison to the market device. Further work is required to validate its robustness in a surgical environment.

## References

1. Burchiel et al, Stereotactic and Functional Neurosurgery, 98:37–42, 2020.
2. Franz et al, IEEE Transactions on Medical Imaging, 33:1702–1725, 2014.
3. Nafis et al, Jr. Proceedings of the SPIE, 6141:152-167, 2006.



# POLARIMETRIC GLUCOSE MEASUREMENT VIA DIGITAL POLARIZATION MODULATION

Ehsan Hassanpour Yesaghi (1,2), Mahsa Nasehi (1,2), Lilian Witthauer\* (1,2)

1. Department of Diabetes, Endocrinology, Nutritional Medicine and Metabolism, Inselspital, Bern University Hospital and University of Bern, Bern, Switzerland; 2. Diabetes Center Berne, Bern, Switzerland

\*Corresponding author: lilian.witthauer@unibe.ch

## Introduction

Continuous Glucose Monitoring (CGM) is a technology that enables people with diabetes to monitor their glucose levels 24 hours a day. Current CGM devices suffer from a delay of 5 to 40 minutes between the actual glucose level and the reading on the device [1,2]. This delay is one of the major causes that hinders the development of a fully automated insulin delivery system and the artificial pancreas. Also, poor accuracy at low and high glucose value, short wearing time, interference with substances, and temperature dependence hinder the optimal performance of current CGMs. Thus, there is a need for new glucose sensing technologies. In this paper, we present our current glucose sensing setup based on polarimetric spectroscopy alongside first preliminary results.

## Material and Methods

Glucose molecules are known to be chiral, meaning they cannot be superimposed with their mirror image. This affects the light transmitted through a sample containing chiral molecules by rotating the light polarization. The amount of rotation is linearly dependent on the glucose concentration as well as the optical path length for any specific wavelength and temperature [3].

$$\theta = \alpha(\lambda, T) \cdot l \cdot c \quad (1)$$

Fig. 2 shows a schematic of the current optical setup for measuring glucose concentrations in aqueous solutions.

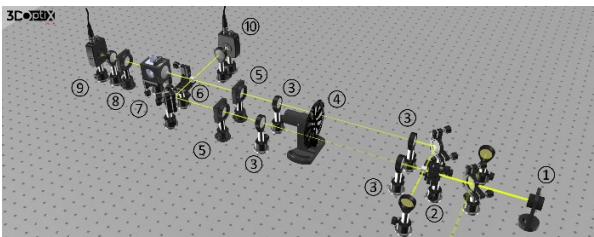


Figure 1: ① Light source, ② Beam splitter, ③ Telescope system, ④ Chopper, ⑤ Polarizer, ⑥ Beam combiner, ⑦ Sample, ⑧ Analyzer, ⑨ Signal detector, ⑩ Reference detector.

## Results

The light polarization rotation was measured for five different glucose concentrations in the physiological range using aqueous glucose solutions. The results are shown in Fig. 3 where a linear behavior between our

measured signal and glucose concentration is observed, which agrees with Eq. 1.

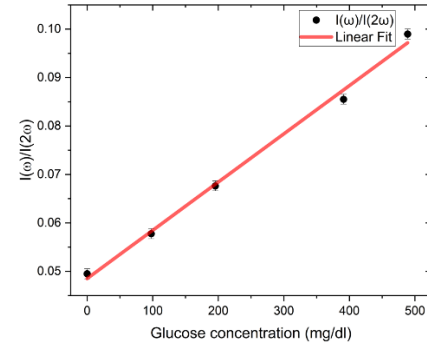


Figure 2: Optical signal equivalent to amount of polarization rotation as a function of glucose concentration.

## Discussion

The preliminary results show that using a simple optical setup, one can measure glucose concentration in the physiological range with sensitivities in the order of 40 micro degrees of polarization rotation. As a next step, we intend to add spectroscopy [4,5] to our setup to enhance both sensitivity and specificity of our setup. We will also investigate effects such as flow, temperature, and pulsation using our custom-built flow simulator. Our final goal is miniaturization of our technology for a real-time accurate CGM.

## References

1. Basu, A. et al. Diabetes **62**, 4083–4087 (2013).
2. Schmelzeisen-Redeker, G. et al. J Diabetes Sci Technol. **9**, 1006 (2015).
3. Stark, C. et al. Biomed. Opt. Express, BOE **10**, 308-321 (2019).
4. Stark, C. et al. Biomed. Opt. Express, BOE **10**, 6340–6350 (2019).
5. Ghosh, S. et al. ACS Photonics **8**, 2234–2242 (2021).

## Acknowledgements

This work was supported by the Diabetes Center Berne Foundation, Berne University Research Foundation (Nr. 33/2022) and by BFH.





# A NOVEL APPROACH TOWARDS SMART MULTI-FUNCTIONAL CATHETERS

Nishant Gupta\* (1,2), Gerhard Kuert (1), Andreas Haeberlin (3), and Thomas Niederhauser (1,2)

1. Institute for Human Centred Engineering, Bern University of Applied Sciences, Switzerland; 2. the sitem Center for Translational Medicine and Biomedical Entrepreneurship, Switzerland; 3. the Department of Cardiology, Inselspital, Bern University Hospital, Switzerland

\*Corresponding author: nishant.gupta@bfh.ch

## Introduction

Catheter-based diagnosis and treatments have gained much attention towards adding intra-corporeal sensing and actuating capabilities that benefit from improved tissue interaction compared to extra-corporeal transducers. However, the extreme size and flexibility requirements limit the feasible number of connections and the multiplexing complexity, thus restricting the sensing capabilities [1]. Here, we describe a simplified networking circuit which not only considerably increases the number of sensing regions (nodes) but also enables ‘surface-integration’, i.e., embedding the entire circuit in the catheter wall [2]. We compare the effective sampling rate (ESR) achievable for the commonly acquired bio-signals and the required wire count.

## Material and Methods

Figure 1(a) illustrates the node circuit, in which the sequentially connected D-type flip-flops (DFF) of  $N$

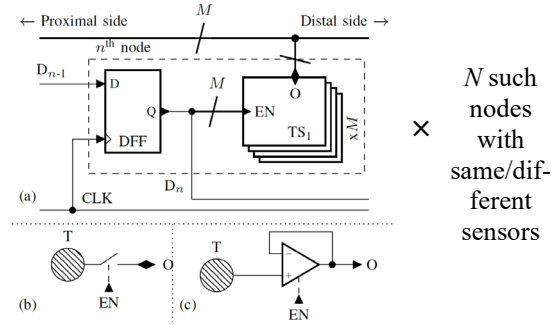


Figure 1: (a) Principal circuit of a node. (b) Bi-directional transducer-switch (TS) interface. (c) Buffered TS interface

nodes provide access to the individual node. The output of the target DFF ( $D_n$ ) enables (via EN input) all the  $M$  transducer-switch (TS) interfaces in the node and connects to the next node in the chain. The state of all DFFs is controlled by 2 external signals:  $D_0$  and clock (CLK), thus allowing interface to all  $M \times N$  transducers using only  $O(M)$  connections + 2 for power. The interface itself could be either a bi-directional switch (Figure 1(b)) or a voltage buffer (Figure 1(c)). The effective sampling rate (ESR) achievable by each node is given by:

$$ESR = 1/(t_c + t_s + t_a) \quad (1)$$

where,  $t_c$ ,  $t_s$ , and  $t_a$  are communication, settling and acquisition times respectively.

## Results

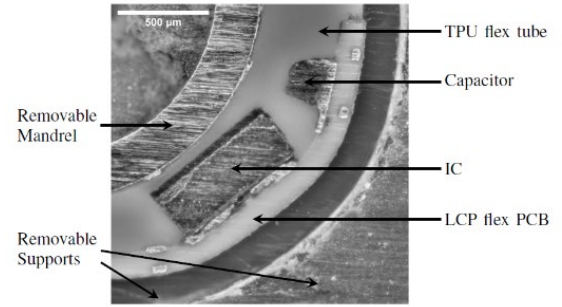


Figure 2: Catheter cross-section. Diameters, outer: 3.3 mm, inner: 2.2 mm. TPU: Thermoplastic Poly-Urethane, IC: Integrated Circuit, LCP: Liquid Crystal Polymer, PCB: Printed Circuit Board

Table 1: ESR (for  $N=10$ ) achieved with the proposed circuit and comparison with grid-based[1] multiplexing

ESR Modality	$(t_s+t_a)$ [μs]	This work $t_c = 125$ ns	Grid-based $t_c < 10$ ns
Impedance	3	32 kHz	33 kHz
ECG/EMG	50	1.99 kHz	2 kHz
Oximetry	150	0.66 kHz	0.66 kHz
Wire count	$M=6$	10	18

## Discussion

The proposed topology provides a daisy-chainable network of sensing nodes capable of high sampling rates. Flexibility towards the number, order, and type of modalities, promotes modularized diagnostic catheters. Together with surface integration and further miniaturization of electronics/sensors, low-cost manufacturing of advanced customizable multi-functional catheters may become possible.

## References

1. S. P. Lee et al., Proc. IEEE, 103:4: 682–689, 2015
2. G. Kuert et al., IEEE EMBC, 6163–6166, 2019

## Acknowledgements

This work was funded by the SNSF (20B1-1 186321/1) and by the Swiss Innovation Agency - Innosuisse (56257.1 IP-LS).



# Index

- Abeken Jonas, 42  
Aebischer Philipp, 18  
Akouissi Outman, 16  
Albers Christoph E., 21  
Alexopoulos Leonidas G., 19, 20  
Alminnawi Ahmad, 47  
Amos Giulia, 13  
Angelmahr Martin, 37  
Anschütz Lukas, 18  
Ariza Gracia Miguel Angel, 43  
Awchi Mo, 33
- Baeriswyl Christof, 35  
Barbero Andrea, 49  
Basoli Valentina, 49  
Baum Cornelia, 39  
Baumgartner Daniel, 39, 40  
Becce Fabio, 9, 29  
Beckmann Felix, 10  
Beltraminelli Anna, 13  
Bermudez-Lekerika Paola, 19, 21, 47  
Bertrand Alexander, 35  
Bigdon Sebastian F., 21, 46  
Bikis Christos, 24  
Boey Hannelore, 14  
Bonmarin Mathias, 55  
Bourgeois Frédéric, 31  
Breakwell Lee, 20  
Bufflé Eric, 12  
Burger Jürgen, 38  
Büchler Philippe, 9, 25, 26, 29, 43  
Bühl Linda, 41  
Bürgler Sarah, 32
- Canbaz Ferda, 27  
Candinas Daniel, 11  
Carrel Thierry, 12  
Cattin Philippe C., 17, 37  
Caversaccio Marco, 18  
Celania Chris, 23  
Ceylan Eylul, 13  
Chan C. H. Michael, 15  
Chansoria Parth , 13  
Chen Shuimu, 46  
Chiesa Roberto, 54  
Civet Yoan, 12  
Clavica Francesco, 12  
Clément Blandine, 13  
Conolly Sinead, 13  
Cordier Dominik, 57, 58  
Corluka Slavko, 45  
Coste Jérôme, 28  
Crocì Eleonora, 39, 40  
Croft Andreas S., 21, 45, 46, 48  
Crump Katherine B., 19, 46, 47
- D'Este Matteo, 49  
Dalbert Adrian, 34
- Datta Alexandre N., 33  
de Wild Michael, 44, 53  
de Zélicourt Diane, 42  
Demory Brice-Olivier, 11  
Deyhle Hans, 10, 22, 52  
Drusova Sandra, 27  
Duru Jens, 13
- Eghbali Pezhman, 9, 29  
Egloff Christian, 41  
Eick Sigrun, 38  
Erbach Georg F., 21
- Fehr Daniel, 55  
Fleck C., 53  
Fox Stephan, 52  
Fratzl Alex, 13  
Frey Urs, 33  
Frigelli Matteo, 25, 43
- Gaab Jens, 32  
Gantenbein Benjamin, 19–21, 45–48  
García-Gómez Diego, 33  
Garnier Manuel, 45  
Genter Jeremy, 39, 40  
Gerber Kate, 39  
Geris Liesbet, 47  
Geys Marlies, 34  
Girardin Sophie, 13  
Goetti Patrick, 9, 29  
Graf Lukas, 53  
Granziera Cristina, 17  
Grossmann Aybar Christian, 55  
Gullo Maurizio R., 50  
Gupta Nishant, 61  
Guzman Raphael, 59
- Ha Thanh Tu, 56–58  
Haas Carola A., 24  
Hadorn D., 36  
Haeberlin Andreas, 61  
Hamidi Arsham, 27  
Harmouch Khaled, 38  
Hassanpour Yesaghi Ehsan, 60  
Heinisch Paul Philipp, 12  
Hemm Simone, 28, 30, 31, 59  
Hess Hanspeter, 39  
Hofmann Martin, 38  
Huber Alexander, 34  
Humbel Mattia, 10, 22  
Häberlin Andreas, 51  
Hörer Jürgen, 12
- Iberite Francesco, 16  
Ihle Stephan J., 13  
Imbach Lukas L., 33
- Jahren Silje E., 12  
Janz Philipp, 24

- Jonkers Ilse , 14
- Kanelis Exarchos, 19, 20
- Katzschmann Robert, 52
- Kaufmann Elisa M., 51
- Killen Bryce A, 14
- Kling Sabine, 25, 26
- Kohler Malcolm, 33
- Kourouklis Andreas P., 55
- Kovacs Balazs, 39
- Kuert Gerhard, 61
- Kunut Ahmet, 34
- Kurtcuoglu Vartan, 42
- Künzler Michael, 45
- Lacey Melissa, 20
- Laimer M., 36
- Le Maitre Christine, 19, 20
- Lemaire Jean-Jacques , 28
- Li Xue, 32
- Li Zhen, 46
- Lopez Antuña Maria, 11
- Luder Yann, 56–58
- Luo Xin, 32
- Lyko Beate, 52
- Madduri Srinivas, 13
- Madec Morgan, 59
- Maintz Michaela, 44, 53
- Malgaroli P., 53
- Mantokoudis Georgios, 18
- March Müller Andres, 39
- Marsano Anna, 50
- Martinez Thomas, 12
- Maurer Benedikt, 13
- Mazza Edoardo, 55
- Meboldt Mirko, 52
- Meinke R., 53
- Mendez Schneider Camilo, 36
- Meylan Arnaud, 29
- Micera Silvestro, 16
- Miklosic Gregor, 49
- Milanesi Nadia, 54
- Moosmann Julian, 10
- Morawska Marta, 56–58
- Morgenroth Elenor, 15
- Moscattelli Monica, 54
- Moser Helen, 45
- Muheim Jonathan, 16
- Muheim Sébastien, 27
- Márquez Neila Pablo, 11
- Mönkemöller Leah, 13
- Müller Andreas M., 40
- Müller Bert, 10, 22, 24, 52
- Müller Judith, 8
- Müller Sebastian, 41
- Mündermann Annegret, 39–41
- Nambiar Malavika H., 43
- Nasehi Mahsa, 60
- Niederhauser Thomas, 38, 51, 61
- Noailly Jérôme, 19, 47
- Nüesch Andrea, 20
- Nüesch Corina, 39, 41
- Oberli Andrea E., 46, 48
- Obrist Dominik, 12
- Osswald Martin, 33
- Oswald Katharina A. C., 21
- Palermo Luana, 32
- Pascal Joris, 59
- Pavarini Matteo, 54
- Perren Aurel, 11
- Perriard Yves, 12
- Pfiffner Flurin, 34
- Pioletti Dominique, 9
- Poggio Martino, 50
- Postolka Barbara, 14
- Richard Mélina, 32
- Rodgers Griffin, 10, 24
- Romell Jenny, 23
- Roska Botond, 13
- Rothenbühler Kilian, 29
- Rothenbühler M., 36
- Ruff Tobias, 13
- Röthlisberger Michel, 56–58
- Rüttimann Silvan, 48
- Samaneh Manavi, 37
- Sampaio Paulo, 11
- Sandkühler Robin, 17
- Satir Osman Berk, 9, 29
- Schade Wolfgang, 37
- Scheel Mario, 22
- Scheidegger Olivier, 51
- Schicker Martina, 56–58
- Schlagenhof Leon, 48
- Schneider Philipp, 7
- Schulz Georg, 10, 22, 24
- Schulz Yannick, 32
- Schär Michael, 45
- Seiler Daniel, 44
- Senti Sebastian, 43
- Sezer Dilan, 32
- Sharma Neha, 49
- Shokur Solaiman, 16
- Sifringer Léo, 13
- Sijgers Leanne, 34
- Singh Kapil Dev, 33
- Sinha Roy Abhijit, 43
- Sinues Pablo, 32, 33
- Spano Fabrizio, 55
- Stawiski Marc, 30
- Steffens Simon, 13
- Storni Federico, 11
- Strunz Franziska, 21
- Studer Harald, 43
- Stutzer Diego, 38
- Sznitman Raphael, 11
- Sökeland Greta, 11
- Tahsini Vahoura, 26

Tang Zhifeng, 32  
 Tankus Esma B., 49  
 Tanner Christine, 10, 24  
 Terrier Alexandre, 9, 29  
 Thalmann Peter, 24  
 Thieringer Florian M., 44, 49  
 Tringides Christina M., 13  
 Tripkis Dimitrios, 22  
 Tseranidou Sofia, 19  
 Twengström William, 23

Usemann Jakob, 33

Van De Ville Dimitri, 15  
 van den Anker Johannes, 33  
 Vander Sloten Jos, 14  
 Vergne Céline, 59  
 Vilaclara Laura, 15  
 Vischer Mattheus, 18  
 Vogel Dorian, 28, 30  
 Vuilleumier Patrik, 15  
 Vulić Katarina, 13  
 Vörös János, 13

Walter Armando, 12  
 Wangler Sebastian, 45  
 Wartenberg Martin, 11  
 Weaver Sean, 13  
 Weder Stefan, 18  
 Wenger Dominik, 38  
 Wicht Jonatan, 11  
 Wildhaber Reto A., 35  
 Williams Frances, 20  
 Wimmer Wilhelm, 18  
 Witthauer Lilian, 36, 60  
 Wolleb Julia, 17  
 Wuertz-Kozak Karin, 19  
 Wårdell Karin, 28

Zenobi-Wong Marcy, 13  
 Ziesenitz Victoria C., 33  
 Züger Fabian, 50